^{17}O and ^{63}Cu Nuclear Resonance Study of the Inhomogeneous Electronic State in $La_{2-x}Sr_xCuO_4$

by

Philip Morgan Singer

Submitted to the Department of Physics
in partial fulfillment of the requirements for the degree of

Doctorate in Physics

at the

MASSACHUSETTS INSTITUTE OF TECHNOLOGY
[February 2003]
October 2002

Author ..... Philip Singer .....
Department of Physics
October 21, 2002

Certified by ..... T. Imai .....
Takashi Imai
Associate Professor
Thesis Supervisor

Accepted by ..... Thomas J. Greytak .....
Thomas J. Greytak
Professor, Associate Department Head for Education

^{17}O and ^{63}Cu Nuclear Resonance Study of the Inhomogeneous Electronic State in $La_{2-x}Sr_xCuO_4$

by

Philip Morgan Singer

Submitted to the Department of Physics
on October 21, 2002, in partial fulfillment of the
requirements for the degree of
Doctorate in Physics

Abstract

Detailed systematic measurements of the spatial variation in the electronic state in the high T_c superconductor $La_{2-x}Sr_xCuO_4$ are presented through a unique combination of ^{63}Cu NQR (nuclear quadrupole resonance) in ^{63}Cu isotope enriched polycrystalline samples for $0.04 \leq x \leq 0.16$, and ^{17}O NMR (nuclear magnetic resonance) in high-quality single crystals for $0.035 \leq x \leq 0.15$. It is evidenced that locally, the hole concentration x_{local} ($\neq x$) modulates over short length scales R_{patch} = 3.0-4.0 nm (= 8-10 a, where a is the lattice spacing) within the CuO_2 plane. The characteristic spatial variation in local hole concentration $^{63}x_{local}$ (according to ^{63}Cu NQR) is determined through a systematic study of the extent of the frequency dependence of the spin-lattice relaxation rate $^{63}1/T_1$ across the inhomogeneous ^{63}Cu NQR spectrum for samples with different nominal hole concentration x. The characteristic spatial variation $^{17}x_{local}$ (according to ^{17}O NMR) is determined through a systematic study of the extent of the overlap of the inhomogeneous ^{17}O NMR spectrum for crystals with different nominal x. The characteristic amplitudes of the spatial variation $^{(63,17)}\Delta x_{local}$, given by $^{(63,17)}x_{local} = x \pm ^{(63,17)}\Delta x_{local}$ according to ^{63}Cu NQR and ^{17}O NMR respectively, are both shown to increase with decreasing temperature below 500-600 K and reach values as large as $^{(63,17)}\Delta x_{local}/x$ = 0.4-0.5 in the temperature range $\geq$ 100 K. The ^{17}O NMR result for the spatial variation $^{17}x_{local}$ determined through the spin channel are semi-quantitatively the same as the ^{63}Cu NQR result $^{63}x_{local}$ determined through the charge channel, implying that the spin and charge degrees of freedom are highly correlated through the local hole concentration across the Brillouin zone. By incorporating the random positioning of $^{+2}$Sr donor ions in the lattice in a novel approach, the length scale of the spatial variation $^{63}R_{patch} \gtrsim$ 3.0 nm is calculated by fitting the entire ^{63}Cu NQR spectrum using a patch-by-patch distribution of the spatial variation $^{63}x_{local}$ with the patch radius $^{63}R_{patch} \gtrsim$ 3.0 nm as the only free parameter. A similar calculation for the patch radius $^{17}R_{patch}$ = 3.0 – 4.0 nm is deduced using the inhomogeneous linebroadening and overlap of the ^{17}O NMR spectrum for different x, and consistent values for the length scale $^{17}R_{patch} \sim ^{63} R_{patch}$ are found. The *same* extent of the frequency dependence in $^{63}1/T_1$ across the ^{63}Cu

NQR spectrum of the high-quality single crystals and the poly-crystalline samples is found, implying that the inhomogeneity in the electronic state is a sample independent, intrinsic phenomenon in $La_{2-x}Sr_xCuO_4$. The implications of the inhomogeneous electronic state to ^{63}Cu wipeout and the stripe phenomenon at lower temperatures are discussed, and the generally believed view that hole doping in the $La_{2-x}Sr_xCuO_4$ alloy is homogeneous across the CuO_2 plane is put into serious question.

Thesis Supervisor: Takashi Imai
Title: Associate Professor

Acknowledgments

My academic career at MIT as has been both fruitful and rewarding, and there are many people I would like to thank for making it happen, in both academic and social settings.

First of all, I would like to thank my fellow laboratory mates at MIT. Kent Thurber, for his help on arrival. He always had a good answers to my questions, or where I could find one. Allen Hunt, for all the work we did together, including the countless hours of data acquisition and sample preparation. He always had a good strategy for trouble shooting and resolving experimental issues, which systematically occurred. His work in the wipeout physics paved the way for the inhomogeneity physics in this thesis. Agneta Cederström, for her involvement in the group, her diversity, and among many other things, her companionship. And my advisor, Takashi Imai, for hiring me in the group well into my career at MIT. He has been a great inspiration, and I thank him for his patience over the years.

Outside of the group at MIT, I would like to thank Jared Martin, Jim Yurko, and Jason Richards. Jessica Thomas, for her help and understanding in physics graduate life, and for her friendship and panache. Jamie Portsmouth, for his comradeship and coffee talks in physics and surrealism in general.

Outside of MIT, I wish to thank Danny Kemp and Nicholas Collings for our long-lasting friendships. I also wish to thank L.v. Beethoven for his musical genius and driving force. And I wish to thank my mother, father, and sister for their support and their presence, without whom this would not have been possible.

Contents

List of Figures

Chapter 1

Introduction

The mechanism of high transition temperature, or high T_c, superconductivity remains enigmatic even after 16 years of its discovery by J.G. Bednorz and K.A. Müller [5], where a $T_c \sim 30$ K in the copper-oxide $La_{2-x}Ba_xCuO_4$ was first reported. Since then, the highest superconducting transition temperature has jumped to $T_c \simeq 130$ K for the mercury based copper-oxide $HgBa_2Ca_2Cu_3O_y$. The material properties of the high T_c superconductors are very different from the conventional superconductors, both in the superconducting state and in the normal state. Conventional superconductors are Fermi-liquid like metals in the normal state, and their superconducting state is well described by Bardeen-Cooper-Schrieffer (BCS) theory [4] with phonon mediated pairing of the electrons. The behavior of high T_c superconductors is much more difficult to describe by conventional condensed matter theory. For a start, the electronic phase diagram of high T_c cuprates involves a number of different phases and transitions, including an antiferromagnetic phase (or Néel state), an insulator-metal crossover, a spin-glass phase, and an overdoped metallic regime, in addition to the superconducting phase with some complex pairing mechanism of the electrons.

The complexity of the phase diagram for $La_{2-x}Sr_xCuO_4$ is illustrated Fig. 1-1. The undoped parent compound, La_2CuO_4, is a Mott insulator which forms long range antiferromagnetic order below the Néel temperature $T_N \lesssim 300$ K (gray region). La_2CuO_4 is a close experimental realization of a 2 dimensional $S = 1/2$ Heisenberg antiferromagnet on a square lattice [8] whose spin Hamiltonian can be described as

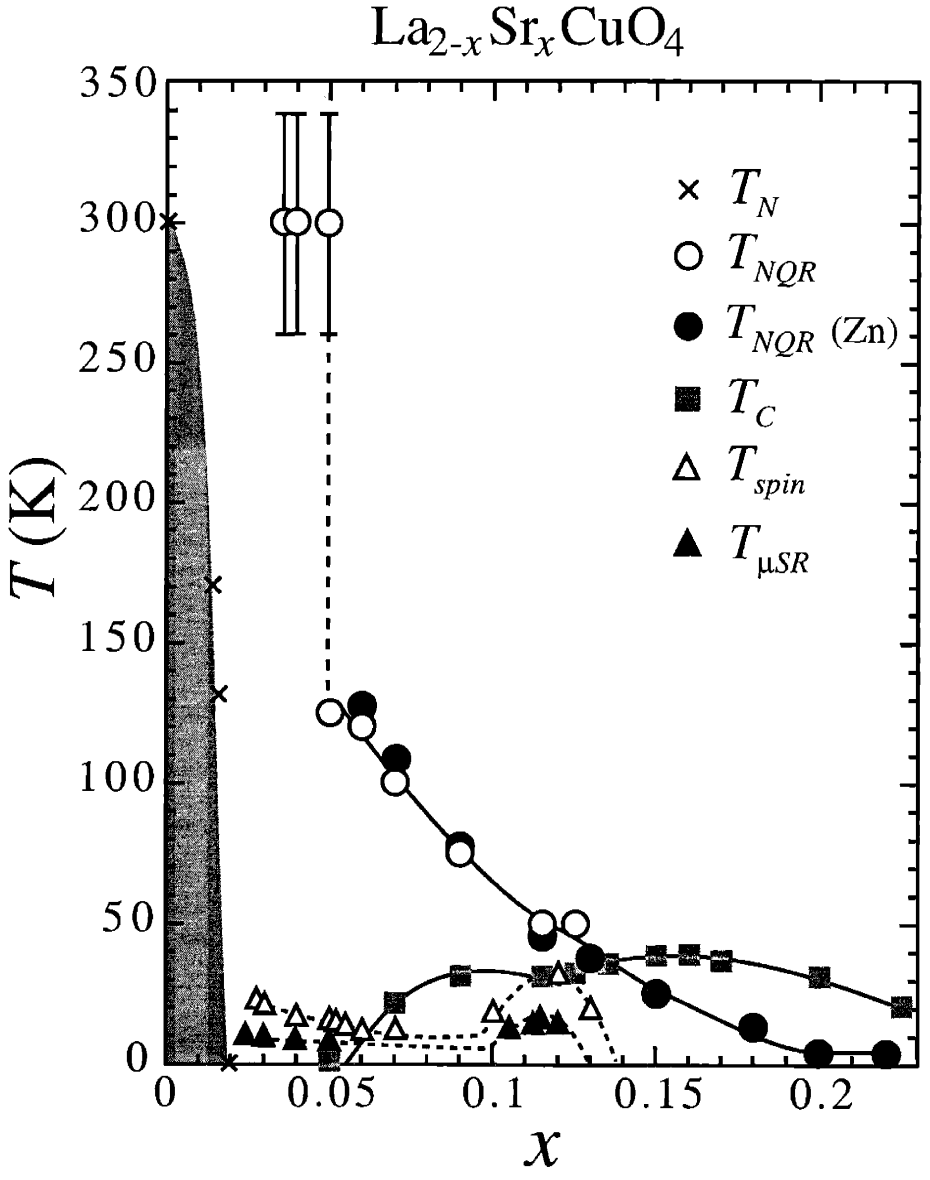

Figure 1-1: Phase diagram of $La_{2-x}Sr_xCuO_4$ showing the onset of ^{63}Cu NQR wipeout T_{NQR} [31] and T_{NQR} (Zn) for $La_{2-x}Sr_xCu_{0.96}Zn_{0.04}O_4$ with dilute amounts of $^{+2}$Zn substitution [78]. Also shown for $La_{2-x}Sr_xCuO_4$ are the onset of superconductivity T_c with a dip at $x \simeq 1/8$ doping, the onset of the Néel state T_N [46], the onset of incommensurate magnetic peaks according to elastic neutron scattering T_{spin} [48, 55, 56, 87, 97] and the onset of μSR asymmetry $T_{\mu SR}$ [49, 65]. Dashed vertical line shows jump in T_{NQR} which coincides with the rotation of the stripe orientation according to neutron scattering and the superconductor-insulator crossover. Other lines are a guide for the eye.

such

$$\mathcal{H} = J \sum_{i,\delta} S_i \cdot S_{i+\delta} \tag{1.1}$$

The localized copper electron spins S_i have (nearly) isotropic antiferromagnetic interactions with their nearest neighbours (δ) in the square CuO_2 plane. The exchange energy $J \sim 130$ meV (or 1500 K equivalently) is rather large in the high T_c cuprates. The parent compound is also very sensitive to the random chemical substitution of $^{+2}$Sr ions in the place of $^{+3}$La ions, which effectively adds holes into the CuO_2 plane by alloying. As shown in Fig. 1-1, long range antiferromagnetic order disappears when only 2 % of holes ($x = 0.02$) are added. Further doping 5% of holes ($x = 0.05$) results in an insulator-superconductor crossover. The occurence of superconductivity for such small amounts of doping suggests that magnetism is important for the pairing mechanism in high T_c materials. The fact that superconductivity is also suppressed if the doping is too high ($x \geq 0.20$) may suggest that overdoping and increased random disorder destroy the spin correlations needed for superconductivity. Even though static antiferromagnetic order disappears above $x = 0.02$, spin fluctuations persist even in the doping region where superconductivity occurs [36, 93]. It therefore seems very likely that the spin correlations are involved in the pairing mechanism for high T_c materials. The original search by J.G. Bednorz and K.A. Müller was for a material with strong electron-phonon interactions, or strong polarons. Whether the strong spin correlations or whether the strong polarons mediate the pairing in high T_c (or both) is still a matter of debate.

A relatively new addition to the already complex electronic phase diagram of high T_c cuprates is the so-called *stripe phase*, which occurs near $x \simeq 1/8$. Soon after the discovery of high T_c, a systematic study of $La_{2-x}Ba_xCuO_4$ revealed an anomalous supression of T_c for $x \simeq 1/8$ [60]. A similar supression of T_c has also been established in Eu and Nd co-doped samples $La_{2-x-y}(Nd,Eu)_ySr_xCuO_4$ [19], and also $La_{2-x}Sr_xCuO_4$ as shown in Fig. 1-1. These studies indicate that there are unusual electronic properties at $x \simeq 1/8$ which seeded the so called "1/8th anomaly". More recently, elastic neutron scattering experiments on $La_{1.6-x}Nd_{0.4}Sr_xCuO_4$ for $x \simeq 1/8$

by J.M. Tranquada *et al.* [93] have demonstrated that the doped holes microscopically phase segregate into hole rivers, forming a charge density wave (CDW). The hole rivers become antiphase boundaries between hole-poor segments in which Cu spins form short range spin density wave (SDW) order. They find that the simplest geometric arrangement of the spin and charge degrees of freedom that provide quantitative agreement with their data consists of spin and charge stripes along the tetragonal lattice symmetry, a pictorial representation of which is shown in Fig. 1-2(a) taken from [93].

In our first two publications on the striped materials, A.W. Hunt *et al.* demonstrated that slowing of stripes in $La_{2-x}Sr_xCuO_4$, $La_{2-x-y}(Nd,Eu)_ySr_xCuO_4$ and in $La_{2-x}Ba_xCuO_4$ can be easily captured by measuring the anomalous reduction, or *wipe-out*, of the ^{63}Cu NQR intensity [31,77]. More specifically, for $La_{2-x-y}(Nd,Eu)_ySr_xCuO_4$ with $0.12 \leq x \leq 0.16$, the onset temperature T_{NQR} of the ^{63}Cu NQR wipeout agrees very well with the onset temperature T_{charge} of short-range charge order detected by neutron [35,93–95] and X-ray [66,102] scattering measurements. Moreover, the wipe-out fraction $F(T)$, defined as the fraction of unobservable ^{63}Cu nuclei in the sample, shows a nearly identical temperature dependence with the charge stripe order parameter observed by scattering techniques, which lead us to argue that the temperature dependence of the wipeout fraction $F(T)$ is *a good measure* [31] of the charge stripe order parameter.

We show the wipeout fraction $F(T)$ in Fig. 1-2(b) in the case of $La_{1.48}Nd_{0.40}Sr_{0.12}CuO_4$ (i.e. $x \simeq 1/8$), and we provide a comparison with the charge stripe order parameter measured by neutron scattering. The charge stripe order parameter is defined as the square root of the neutron scattering intensity which corresponds to our measured quantity $F(T)$. We see a remarkable similarity between the onset of the charge stripe order parameter at $T_{charge} \simeq 70$ K and the onset of NQR wipeout at $T_{NQR} = 70 \pm 5$ K, and furthermore, the temperature dependences are consistent below $T_{charge} \simeq T_{NQR}$. Also shown is the temperature dependence of the spin stripe order parameter. Note that charge stripe order $T_{charge} \simeq 70$ K preceeds the onset of spin stripe order at $T_{spin} \simeq 50$ K. The discovery of charge and spin stripe order and the close similarity

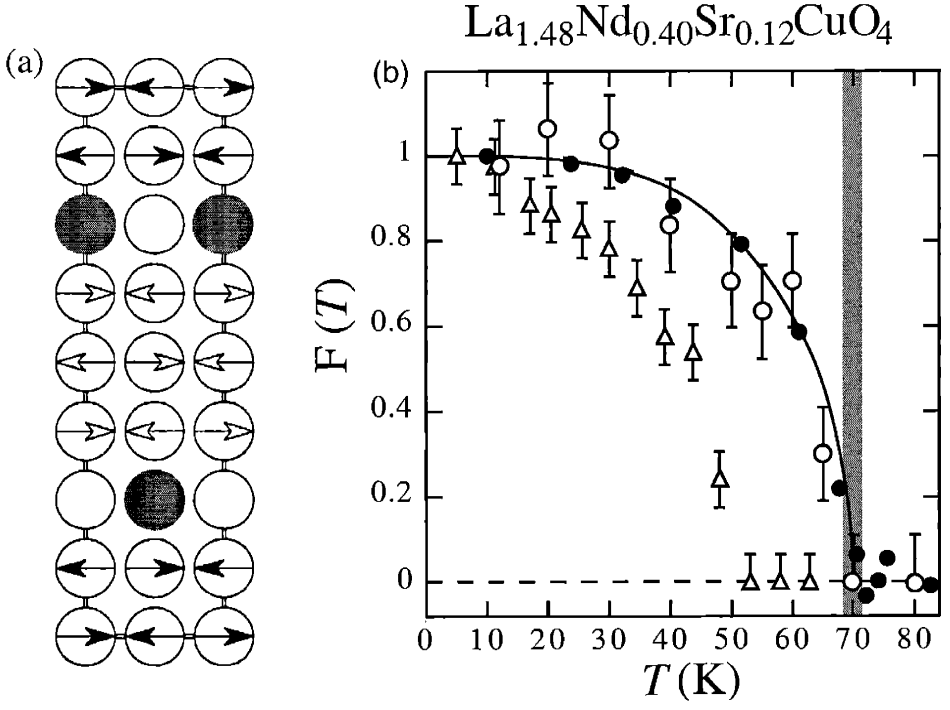

Figure 1-2: (a) The original picture of stripes, from J.M Tranquada *et al.* [93], where the arrows represent the Cu spins, and are colored white or black to indicate opposite phases. The doped holes are shown as grey circles. (b) The temperature dependence of the square root of the intensity of the incommensurate charge (○) and spin (△) peaks according to elastic neutron scattering in $La_{1.48}Nd_{0.40}Sr_{0.12}CuO_4$ [93]. Also shown is the ^{63}Cu NQR wipeout fraction $F(T)$ (•) (defined as the fraction of unobservable ^{63}Cu signal) for the same material. Gray region shows the onset temperature for charge stripe order $T_{charge} \simeq 70$ K. Lines are a guide for the eye.

with temperature dependence of our NQR data (Fig. 1-2) prompted us to carry out a systematic study of $F(T)$ for $La_{1.6-x}Nd_{0.40}Sr_xCuO_4$ over a wide range of x. The results of our systematic study (taken from [77]) are shown in Fig. 1-4. One very important feature we discovered was the qualitative difference above and below $x \simeq 1/8$: for $x \gtrsim 1/8$, we found a sharp collective onset of $F(T)$ below T_{NQR}, where T_{NQR} decreases with increasing x. For $x < 1/8$, we found a tailed onset of $F(T)$ below T_{NQR} followed by an inflection point T_{NQR}^{inflec} where $F(T)$ accelerates below $T_{NQR}^{inflec}(< T_{NQR})$. T_{NQR} for $x \gtrsim 1/8$ and T_{NQR}^{inflec} for $x < 1/8$ are found to create a dome-like feature in the wipeout phase-diagram centered at the magic hole concentration of $x \simeq 1/8$ [32].

Further studies into the stripe phenomenon [32] clarified our view-point that T_{NQR} represents the onset of glassy slowing of stripe fluctuations for $x \gtrsim 1/8$, triggered by the slowing of charge dynamics. This is certainly the case at $x \simeq 1/8$ where charge stripe order below $T_{charge} \simeq T_{NQR} \simeq 70$ K leads to the onset of spin stripe order at $T_{spin} \simeq 50$ K (shown in Fig. 1-2) and μSR precession at even lower temperatures $T_{\mu SR} \simeq 30$ K [62]. The difference in onset temperatures reflects the *glassy* slowing of the stripes fluctuations. As shown and explained in detail in Ref. [32], in the case of $x \simeq 1/8$ the characteristic frequency scale Γ of the spin stripe fluctuations slow down from a well defined value $\Gamma = 10^{12}$ Hz at $T_{charge} \simeq 70$ K, to $\Gamma \sim 10^7 - 10^{10}$ Hz at $T_{\mu SR} \simeq 30$ K. The fact that the spin fluctuations do not immediately become static at a particular temperature implies a glassy transition.

The glassy nature of the slowing is observed experimentally due to the fact that each experimental probe has its own characteristic frequency-scale of measurement. The lower the characteristic frequency-scale of the probe, the lower the onset temperature of the stripe anomaly. For neutron scattering, the experimental frequency-scale is given by the resolution width, typically $\sim 10^{11} - 10^{12}$ Hz. The μSR frequency-scale is given by the inverse of the natural decay time of the muons $\sim 10^7$ Hz. For NQR, the frequency-scale is given by the inverse of the r.f. pulse separation time $\sim 10^5$ Hz which is equivalent to the shutter speed of the NQR experiment. Using the experimental data from various probes and their corresponding frequency-scales, we self-consistently reproduced the observed temperature dependence of $F(T)$ [32] for

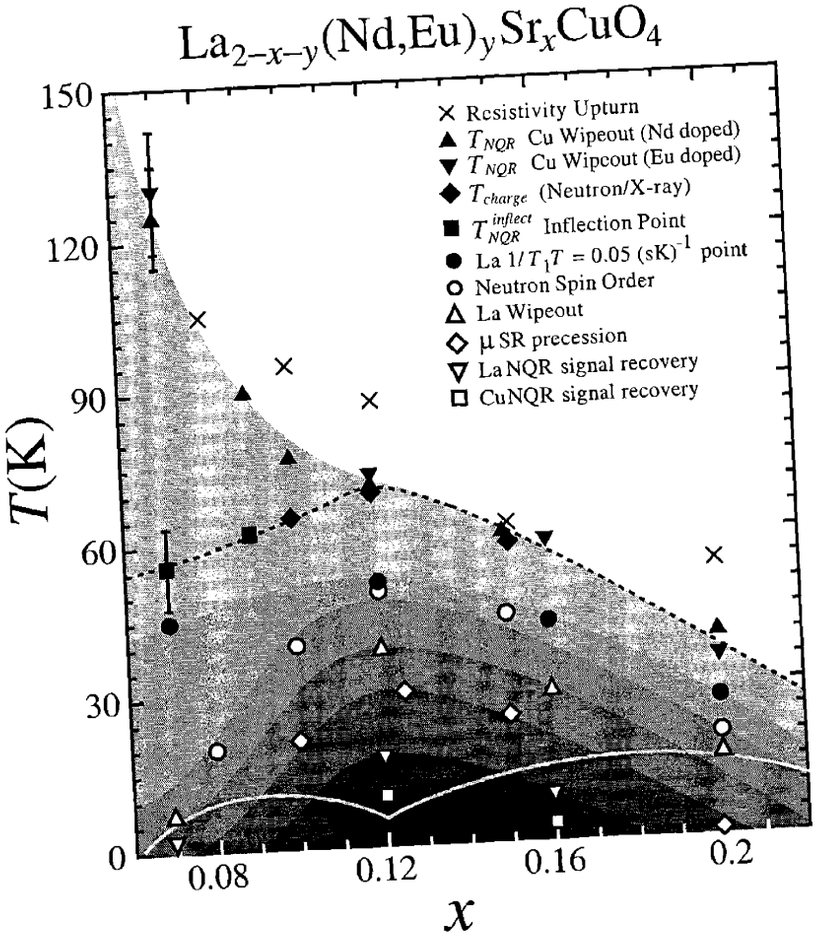

Figure 1-3: Phase diagram for $La_{1.6-x}Nd_{0.4}Sr_xCuO_4$ and $La_{1.8-x}Eu_{0.2}Sr_xCuO_4$, showing the upturn in ab-plane resistivity temperature T_u found in $La_{1.6-x}Nd_{0.4}Sr_xCuO_4$ [35] (×), ^{63}Cu wipeout onset T_{NQR} in $La_{1.6-x}Nd_{0.4}Sr_xCuO_4$ (▲) and $La_{1.8-x}Eu_{0.2}Sr_xCuO_4$ (▼), onset temperature T_{charge} for short range charge order according to neutron [35, 94] and X-ray [66, 102] in $La_{1.6-x}Nd_{0.4}Sr_xCuO_4$ (◆), the copper wipeout inflection point (■) in $La_{1.6-x}Nd_{0.4}Sr_xCuO_4$, the temperature where $^{139}1/T_1T = 0.05\,(\mathrm{sK})^{-1}$ in $La_{1.8-x}Eu_{0.2}Sr_xCuO_4$ (●), long range spin order T_{spin} [35,95] in $La_{1.6-x}Nd_{0.4}Sr_xCuO_4$ (○), onset of La wipeout for $La_{1.8-x}Eu_{0.2}Sr_xCuO_4$ (△), onset of μSR coherent precession $T_{\mu SR}$ [62] for $La_{1.6-x}Nd_{0.4}Sr_xCuO_4$ (◇), the onset of ^{139}La recovery of signal in $La_{1.8-x}Eu_{0.2}Sr_xCuO_4$ (▽), and the onset of ^{63,65}Cu recovery of signal in $La_{1.8-x}Eu_{0.2}Sr_xCuO_4$ (□). The darker grey tones indicate increasingly slow fluctuation timescales. We also show the superconducting boundary as a white line and a dotted line that connects T_{charge} and the Cu wipeout inflection points as a guide for the eye.

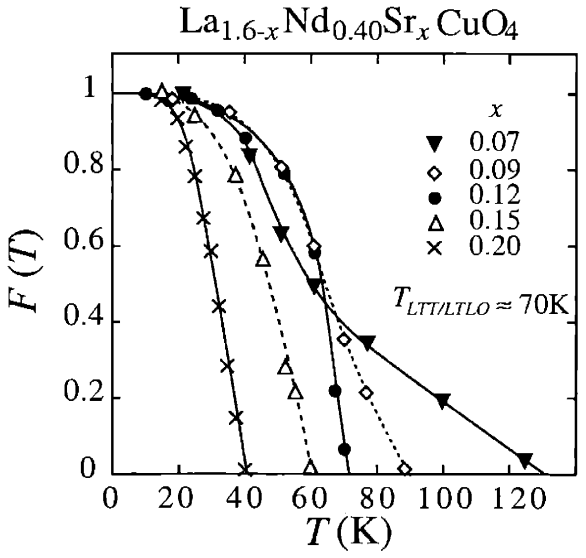

Figure 1-4: The fraction of wiped out signal, $F(T)$, in $La_{1.6-x}Nd_{0.4}Sr_xCuO_4$ where the symbols used for each hole concentration x are listed in the figure. The low temperature structural phase transition temperature T_{LTT} for $x \simeq 1/8$ is $T_{LTT} \sim 70$ K [35]. The lines are guides for the eye and only data points below T_{NQR} are plotted.

$x \gtrsim 1/8$.

The physical picture we proposed in [32] was that certain regions of the CuO_2 plane begin to charge order below T_{NQR} and exhibit the glassy slowing of the spin stripe fluctuations. Other regions, however, remain in the "normal" ω/T scaling regime. The observed wipeout fraction $F(T)$ then corresponds to the total area in the CuO_2 planes within which the glassy slowing has begun. As explained in [32], the glassy slowing in the wipeout regions results in enhanced spin-lattice relaxation rates in excess of the cutoff $^{63}1/T_1^{cutoff} \sim 6000$ s^{-1}. The reason ^{63}Cu nuclei with $^{63}1/T_1 >^{63} 1/T_1^{cutoff}$ are no longer observable is because their spin-spin relaxation rate $^{63}1/T_2(>^{63} 1/T_1)$ is so large that the signal decays before we can measure the re-focusing of the spin-echo. Another way of putting it is that the shutter speed of the NQR experiment is too slow. In our physical picture, the fraction $(1 - F(T))$ then corresponds to the "normal" ω/T scaling regions where the ^{63}Cu nuclei have mild relaxation rates $^{63}1/T_1 \sim 2000$ s^{-1}, i.e. below $^{63}1/T_1^{cutoff}$.

As evidenced in Fig. 1-4, for $x > 1/8$ a sharp onset temperature for $F(T)$ is

also found, implying that a similar collective effect is taking place to $x \simeq 1/8$. We also found an overall decrease in the onset temperature T_{NQR}. In fact, independent X-ray scattering measurements [66] for $x = 0.15$ found a lower onset temperature for charge order $T_{charge} \simeq 55$ K, consistent to our wipeout onset $T_{NQR} \simeq 60 \pm 5$ K. This gave strong supportive evidence that $T_{NQR} \simeq T_{charge}$, at least in the region $x \gtrsim 1/8$. Analysis of the glassy slowing for $x > 1/8$ also revealed a lower energy scale for the glassy slowing away from $x \simeq 1/8$ where the stripe fluctuations are most robust [32,77].

The region $x < 1/8$ is a different story all together. As shown in Fig. 1-4 in the case of $x = 0.07$ and $x = 0.09$, we found that the temperature dependence of $F(T)$ is tailed for $x < 1/8$ [31,77]. This implies that a collective phenomenon is not taking place immediately below T_{NQR}. However below T_{NQR}, we also found that an inflection point $T_{NQR}^{inflect}$ existed below which the temperature dependence of $F(T)$ is accelerated. In the case of $x = 0.09$, $T_{NQR}^{inflect} = 60 - 65$ K while T_{NQR}= 88-92 K, and for $x = 0.07$, $T_{NQR}^{inflect} = 50 - 55$ K while $T_{NQR} = 120 - 130$ K. Note that while $T_{NQR}^{inflect}$ *decreases* with decreasing x, the onset of the tailed wipeout below $T_{NQR}(> T_{NQR}^{inflect})$ *increases* with decreasing x. Clearly a different kind of mechanism is kicking below T_{NQR} which is distinct to the collective effect below $T_{NQR}^{inflect}$. More recent neutron and X-ray scattering for $x = 0.10$ and $x = 0.08$ [35] found that the onset of charge stripe order T_{charge} and the structural transition temperature T_{LTLO} into the LTLO (low temperature less orthorhombic) phase coincided, i.e. $T_{charge} \simeq T_{LTLO}(\lesssim 65$ K). This is analogous to the findings at $x \simeq 1/8$ where the LTT (low temperature tetragonal) structural transition $T_{LTT} \simeq$70 K coincides with the onset of charge order $T_{charge} \simeq T_{LTT}$ [93]. The neutron and X-ray results for all x suggest that static charge order cannot develop without the tetragonal symmetry that is compatible with the symmetry of the charge stripes. We immediately gained insight into the wipeout for $x < 1/8$ by noting that the inflection point $T_{NQR}^{inflect}$ (Fig. 1-4) coincides with $T_{charge} \simeq T_{LTLO}$. This implies that the long spatial coherence of the charge stripes below $T_{charge} \simeq T_{LTLO} \simeq T_{NQR}^{inflect}(< T_{NQR})$ for $x < 1/8$ accelerates wipeout at the inflection point in $F(T)$. This explained the collective feature of $F(T)$ below $T_{NQR}^{inflect}$,

however, the tailed wipeout region $T_{NQR}^{inflect} < T < T_{NQR}$ for $x < 1/8$ still remained a mystery.

In earlier publications [31, 38, 77] we suggested that the tailed wipeout for $x < 1/8$ may be accounted for if we assume that individual holes begin to localize with decreasing temperature, thereby creating local moments. This is a situation similar to the one that results in wipeout in conventional dilute Kondo alloys [63] and spin glasses [51]. On the other hand, in this scenario in which the local moments are created by localization effects, the precursive wipeout for $T_{NQR}^{inflect} < T < T_{NQR}$ may be further enhanced if one increases resistivity by introducing disorder. However as shown in Fig. 1-1, our experimental studies on Zn doped $La_{2-x}Sr_xCu_{0.96}Zn_{0.04}O_4$ show that the onset of wipeout T_{NQR} is a fairly well-defined temperature scale that does not vary even when resistivity is enhanced and local moments are introduced by $^{+2}$Zn impurity doping [78]. The observation that the increase in localized spins induced by $^{+2}$Zn impurities does not change the wipeout effects is a significant contradiction to claims made by certain researchers such as the group at Los Alamos [20]. They believe that spin glass-like physics is the only piece of underlying physics needed to account for the observed Cu wipeout. In particular, their oversimplification does not involve any kind of stripe physics in their model, which in our view is highly questionable given the uncanny similarity between the sharp collective onset of $F(T)$ at T_{NQR} or the inflection point, $T_{NQR}^{inflect}$, and the charge stripe ordering temperature T_{charge} shown in Fig. 1-2 and Fig. 1-4. Instead, they attribute the Cu wipeout in the entire doping region x to certain unknown inhomogeneities in the CuO_2 plane which cause local moment-like effects and Cu wipeout for neighbouring Cu sites.

It is certainly true that the NQR/NMR (nuclear magnetic resonance) community has been aware of some mysterious inhomogeneity effect in $La_{2-x}Sr_xCuO_4$ and related compounds [11, 20, 22, 25, 26, 31, 32, 45, 77-80, 83, 92, 101] since the 1980's, such as the Curie-Weiss like temperature dependence of the NMR linewidth which is not consistent a simple localized moment picture. Local moments cause a Curie like temperature dependence $\sim 1/T$ of the NMR linebroadening. Yet no clear picture has emerged that discerns and relates the effects of inhomogeneity, genuine electronic

phase separation, stripe modulation, and random substitution of donor ions. On the other hand, recent STM (scanning tunnelling microscopy) studies on the surface state of $Bi_2Sr_2CaCu_2O_{8+\delta}$ cleaved at low temperature [67] reveal spatial variations of the electronic state on a short length scale ~nm in the surface plane. Whether such ~nm modulations are universally observable in the bulk and other high T_c materials remains to be seen, but the STM results have enhanced the interest in the potential impact of the spatial inhomogeniety of the electronic properties in cuprates.

Motivated by these historic events, we set out to conduct a detailed systematic study of the *local* electronic state in $La_{2-x}Sr_xCuO_4$ by taking advantage of the local nature of the NMR/NQR techniques. The NMR and NQR techiques are inherently sensitive to spatial variation of the electronic states with atom resolution. Furthermore, NMR/NQR techniques are bulk sensitive, which means that our results are guranteed to reflect the entire sample, and we can even probe the temperature dependence in a broad range comparable to J. We recall that many other techniques such as STM and angle-integrated photo emission probe only the surface of the crystal which does not necessarily represent the bulk properties. They are also incapable of probing the local electronic states in the temperature range of interest

The key feature we utilize are the *inhomogeneously* broadened NMR and NQR lineshapes. In undoped La_2CuO_4, the ^{63}Cu NQR linewidth is *homogeneously* broadened. *Homogeneous linebroadening* is NMR jargon which in the present case implies that the linewidth of the spectrum is proportional to the very long electron spin-spin correlation length ξ_{AF}. On the other hand, the ^{63}Cu NQR lineshape in $La_{2-x}Sr_xCuO_4$ is known to be *inhomogeneously broadened* by spatial variations in Electric Field Gradient (EFG) tensors. Likewise the ^{63}Cu NMR lineshape is *inhomogeneously broadened* by spatial variations in Knight shifts. The origin of the large distribution in the EFG has never been investigated extensively since most researchers considered it to be the mere consequence of disorder by alloying effects between $^{+2}$Sr and $^{+3}$La ions (there has also been a persistent false assertion that the ^{63}Cu NQR lineshape reflects electronic phase separation into two regions). The ^{17}O NMR lineshape also exhibits an unusually broad spectrum. with Curie-Weiss like temperature dependence in the

linewidth. This has also been a long mystery in the NMR community (as mentioned above) since the presence of local moments should lead to a Curie like temperature dependence of the linewidth instead.

In this thesis, we present our detailed measurements of the *frequency dependence* of spin and charge properties across the ^{63}Cu NQR and ^{17}O NMR lineshapes. We also present novel lineshape simulations that explicitly take the alloying effects into account. Our results indicate that, contrary to common assumptions, disorder effects or local moments are not the cause of the extreme inhomogeneous linebroadening in $La_{2-x}Sr_xCuO_4$. Instead, we show that the inhomogeneous linebroadening reflects a spatial variation over the short $\sim$6 nm length scales of the local electronic states. By conducting detailed measurments as a function of temperature, we demonstrate that it involves certain thermodynamic effects.

The rest of this thesis is sectioned as follows: in chapter 2 we characterize our poly-crystalline samples, we present the experimental techniques and notation for ^{63}Cu NQR, and we describe the NQR/NMR spectrometer. In chapter 3 we present the experimental results for ^{63}Cu NQR including the frequency dependence of $^{63}1/T_1$ to determine $^{63}x_{local}$, and the temperature dependence of the ^{63}Cu NQR spectrum. In chapter 4 we present the analysis of the ^{63}Cu NQR data using the patch-by-patch model of the inhomogeneous electronic state. We formulate of the point charge calculation of the EFG (electric field gradient) incorporating randomness effects and deduce the lower bound $^{63}R_{patch}$ and $^{63}x_{patch}$ above T_Q. We also fit the NQR data below T_Q to deduce the local orthorhombic distortions of the lattice. In chapter 5 we summarize the ^{17}O NMR data of the spatial variation and compare with ^{63}Cu NQR data. In chapter 6 we present our conclusions.

Chapter 2

Experimental Techniques and Procedures

2.1 Sample Characterisation

All of the single phase, poly-crystalline samples of $La_{2-x}Sr_xCuO_4$ used in this study were prepared using conventional solid state reactions [72,89]. We mix predried La_2O_3 (99.995%), $SrCO_3$ (99.995%), and ^{63}CuO (99.995%) with correct nominal compositions using an agate mortar and pestle until an intimate mixture is obtained. A prereaction is carried out for 20 h in a box furnace at 850°C followed by repeated regrindings and sinterings (also 20 h) at temperatures between 950°C and 1000°C. During these initial firings the materials are usually made into low density pellets with a hand press. Finally the samples are pelletized with the pneumatic press and high temperature annealed in flowing O_2 gas at 1100°C to 1150°C for 24 h to 48 h before a slow and controlled cooling cycle that includes low temperature annealing at 800°C (24 h) and 500°C (24 h). The long annealing in O_2 insures that the oxygen content is uniform and stoichiometric and high annealing temperatures insure fast reaction kinetics. By using a large number of grindings (typically 5-8), we acheive homogeneous, high quality poly-crystalline samples.

The most important test on the quality of our poly-crystalline samples is shown in Fig. 2-1. In Fig. 2-1 we compare the extent of the inhomogeneity in high-quality

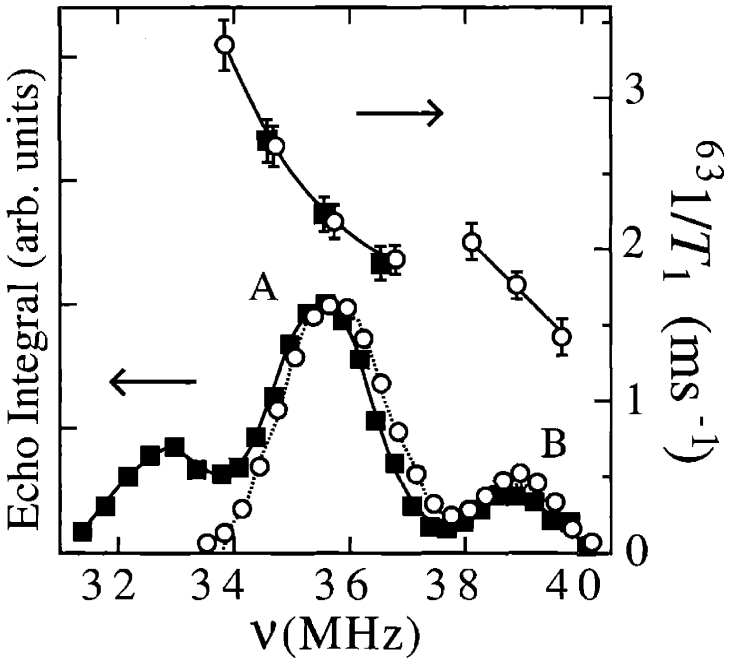

Figure 2-1: Cu NQR spectrum (left axis) and frequency dependence of $^{63}1/T_1$ (right axis) at 100 K for single crystal $x = 0.15$ (■) [80] and ^{63}Cu isotope enriched polycrystalline sample $x = 0.16$ (○) [79]. Extra feature in Cu NQR spectrum at lower frequency side for (■) is from ^{65}Cu isotope. Dashed line is fit using patch-by-patch model with a lower bound for the patch radius of $^{63}R_{patch} = 2.6$ nm, while solid lines are a guide for the eye.

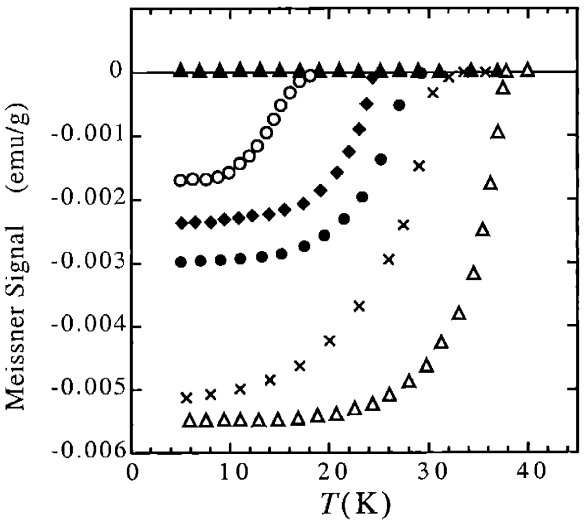

Figure 2-2: Temperature dependence of field cooled Meissner signal in 15 Oe for poly-crystalline $La_{2-x}Sr_xCuO_4$ with $x = 0.20$ (×), $x = 0.16$ (△), $x = 0.115$ (•), $x = 0.09$ (♦), $x = 0.07$ (○), and $x = 0.04$ (▲).

single crystals [80] and our poly-crystalline samples (reported here and in Ref. [79]) by measuring the frequency dependence of $^{63}1/T_1$ across the ^{63}Cu NQR spectrum. We find entirely consistent results between samples. This immediatelty establishes that the inhomogeneity in the electronic state in $La_{2-x}Sr_xCuO_4$ is an *intrinsic* phenomenon common to many samples, and also rules out certain claims that our poly-crystalline samples are somehow more inhomogeneous than those reported elsewhere. Such claims on the quality of our poly-crystalline samples originated as an excuse to negate the fact that hole doping is inhomogeneous in $La_{2-x}Sr_xCuO_4$ [79].

Apart from ^{63}Cu NQR itself, we characterise our poly-crystalline samples by measuring the superconducting transition T_c and the room temperature lattice parameters. We deduce T_c by measuring the Meissner signal using a SQUID magnetometer in the field cooled mode with a constant applied magnetic field of 15 Oe, the results of which are shown in Fig. 2-2. We find that the onset temperature of the diamagnetic susceptibility, T_c, and the volume fraction agree with previous measurments in poly-crystalline samples prepared in a similar fashion [72, 89].

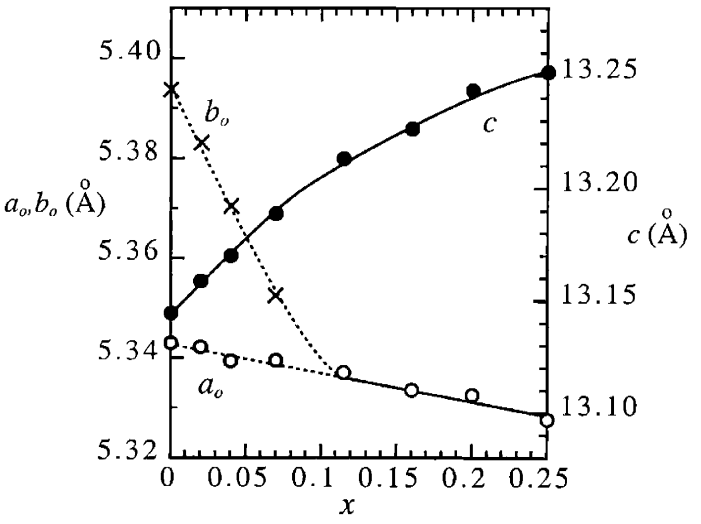

Figure 2-3: x dependence of lattice constants at 295 K deduced by X-ray diffraction along the a_o (○), b_o (×), and c (•) axes using orthorhombic notation.

We deduce the lattice parameters with an X-ray diffractometer using the Cu $K\alpha^1$ line. The lattice parameters are shown in Fig. 2-3, which show close agreement with previous results [72]. We shall use the data in Fig. 2-3 for our analysis in chapter 4. In this thesis, we define a_o and b_o to be the lattice parameters in orthorhombic notation and $[a_o, b_o, c]$ as the vector along the orthorhombic directions. Likewise, we define a and $b(=a)$ as the lattice parameters in tetragonal notation and $[a, b, c]$ as the vector along the tetragonal direction. An illustration of the body-centered tetragonal cell is shown in Fig. 2-4.

Our typical X-ray linewidths were comparable to the instrumental resolution with a *HWHM* $\delta_{Instr} \sim 0.025^o$ determined using a high quality Si standard. Previous higher resolution X-ray diffraction experiments [88] (where $\delta_{Instr} \sim 0.01^o$) were able to use the observed X-ray linewidths and overlaps between different samples x to deduce a lower bound to the compositional distribution with a *HWHM* $\delta x_{Sr} \sim 0.01$. Only a lower bound to δx_{Sr} could be inferred because X-ray diffraction takes a spatial average over length scales larger than tens of nm's [88]. They attributed $\delta x_{Sr} \sim 0.01$ to imperfect mixing inherent to the solid state reaction. Similar conclusions were

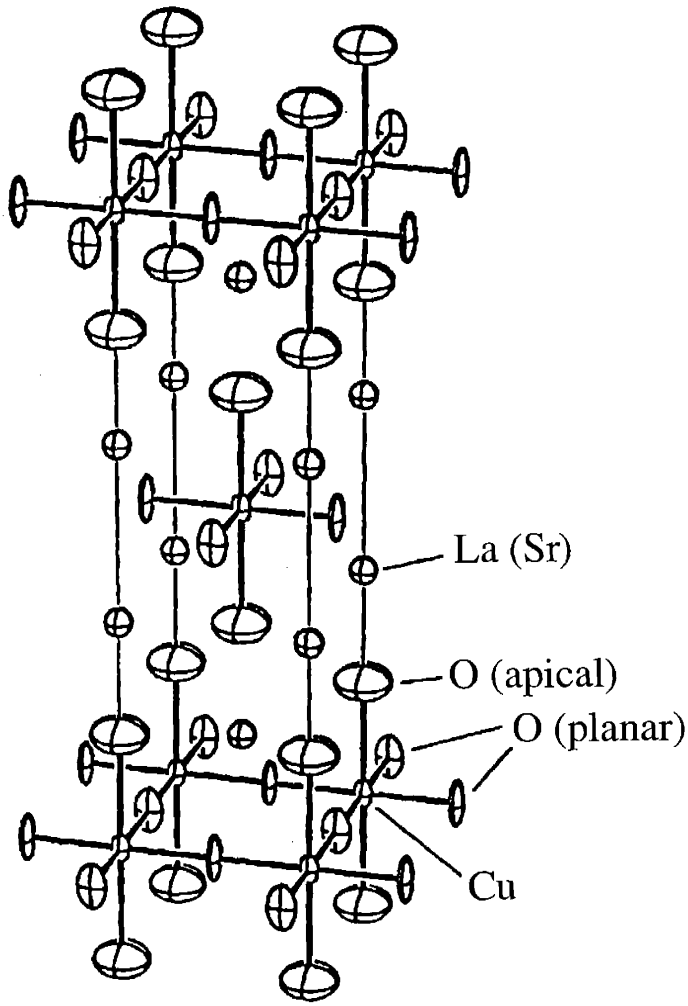

Figure 2-4: Picture of crystal structure for $La_{2-x}Sr_xCuO_4$ with the atomic positions labeled, adapted from [44].

reached [72] using overlaps of X-ray diffraction and neutron Bragg peaks between different x where $\delta x_{Sr} \sim 0.015$ was deduced.

We confirmed the same order lower bound $\delta x_{Sr} \simeq 0.013$ in single crystal $x = 0.15$ [80] using EMPA (electron micro-probe analysis) whose length scale is determined by the focus area of the beam $\sim 1\mu$m. This means that even for high-quality single crystals whose spatial variation of $^{+2}$Sr content is as small as $\delta x_{Sr} \simeq 0.013$ ($\ll {}^{63}\Delta x_{local}$) over $\sim 1\mu$m still exhibits a large modulation in the local electronic states as detected by NQR at much shorter $\sim$nm length scales. Furthermore, we will demonstrate in chapter 3 that ${}^{63}\Delta x_{local}$ is temperature dependent and increases with decreasing temperature. This means that the variation in $^{+2}$Sr content from the solid state reaction alone cannot account for our findings. Instead, a thermodynamic process must be involved.

2.2 NQR Techniques and Procedures

2.2.1 The Quadrupole Interaction

The nucleus interacts with the charge environment through the charge distribution of the nucleus. The simplest way to express the charge interactions is by the multipole expansion of the charge distribution in spherical harmonics of order l. Obviously, the nuclei has a charge monopole moment ($l = 0$), Ze, which interacts with the electric field. However, this interaction is independent of the direction of the spin of the nucleus, so the nuclear spin transitions are not effected by this interaction. The next moment, an electric dipole moment ($l = 1$), is prohibited by the fact that nuclear states have well-defined parity. In fact, this prohibits any charge multipoles with odd l.

The quadrupole moment ($l = 2$), ${}^nQ$ for the nuclear species n, is allowed and is defined as [1,81]

$$e^nQ = \frac{1}{2}\int (3z^2 - r^2)\rho(\mathbf{r})^n d\mathbf{r} \tag{2.1}$$

where $\rho(\mathbf{r})^n$ is the charge distribution of the nucleus in its maximum magnetic eigen-

state $m_I = I$ where I is the total nuclear spin. Taking the z-axis as the magnetic quantization axis and I^z as the nuclear spin operator along the quantization axis, m_I is given by the eigenvalue

$$I^z |I, m_I\rangle = m_I |I, m_I\rangle \tag{2.2}$$

Physically, the quadrupole moment represents the deviation of the charge distribution of the nucleus from spherical symmetry. A "pancake" shaped charge distribution will have a negative quadrupole moment (which is the case for ^{63}Cu), while a "rocket-ship" shaped charge distribution will have a positive quadrupole moment(which is the case for ^{17}O). Note that $^nQ = 0$ for $I = 1/2$ nuclei since flipping between $m_I = \pm 1/2$ states has no effect on the total Coulomb energy between the nucleus and the surrounding EFG. $I \geq 1$ must be satisfied for $^nQ \neq 0$.

Higher order moments of the charge distribution probably do exist, but the interaction effects become smaller very rapidly for higher orders. The interaction strength is expected to decrease roughly as [1]

$$\left(\frac{R_n}{R_e}\right)^l \approx (10^{-5})^l \tag{2.3}$$

where R_n is the radius of the nucleus and R_e is the radius of the electron distribution. This very rapid decrease in the interaction strength is clearly seen in the comparison of the $l = 0$ monopole and $l = 2$ quadrupole interactions. The monopole interaction between the charge of the nucleus and the electrons will be of order 10 eV, while a typical quadrupole interaction is of order 10 MHz $\sim 10^{-8}$ eV.

The quadrupole moment ^nQ interacts with the total EFG (electric field gradient) $V^{(\beta,\gamma)}$ at the position of the nucleus ($r = 0$), and is therefore a charge probe. The traceless symmetric tensor $V^{(\beta,\gamma)}$ is defined as such [1]

$$V^{(\beta,\gamma)} = \left(\frac{\delta^2 \mathcal{V}}{\delta x_\beta \delta x_\gamma}\right)_{r=0} \tag{2.4}$$

where $\mathcal{V}$ is the total Coulomb potental at the origin and (β, γ) are any two orthogonal

spatial directions. The interaction Hamiltonian is then given by [1]

$$\mathcal{H}_Q = \sum_{\beta,\gamma} \frac{e^n Q}{6I(2I-1)} \left\{ \frac{3}{2}(I^\beta I^\gamma + I^\gamma I^\beta) - \delta^{\beta,\gamma} I(I+1) \right\} \cdot V^{(\beta,\gamma)} \tag{2.5}$$

In the case of Cu, there exist two stable isotopes $n = 63(65)$ with natural abundances of 69 (31) % respectively, both with a nuclear spin $I = 3/2$. This is both an advantage and a disadvantage. It is generally a disadvantage in the sense that their quadrupole moments ${}^nQ$ happen to be similar ${}^{63}Q/{}^{65}Q = 1.081$, and therefore their NQR spectrum tend to coincide. This is the case in $La_{2-x}Sr_xCuO_4$ for $x > 0.05$ where the NQR spectrum from each isotope is broad enough that they merge in the temperature range of interest, and therefore ^{63}Cu isotope enrichment is essential to separate the lines.

Using Eq. (2.5), the resonance frequency tensor ${}^{63}\nu_Q^{(\beta,\gamma)}$ is then given by [1,81]

$${}^{63}\nu_Q^{(\beta,\gamma)} = \frac{e^{63}Q}{2h} V^{(\beta,\gamma)} \tag{2.6}$$

$V^{(\beta,\gamma)}$ can be rotated and diagonalised to point towards the principle axes α of the EFG. This leads to the following relation

$${}^{63}\nu_Q^{\alpha} = \frac{e^{63}Q}{2h} V^{\alpha} \tag{2.7}$$

In the tetragonal phase, the principle axes α are along the crystal axes $[a, b, c]$, and satisfy the general traceless condition

$$V^c + V^b + V^a = 0 \tag{2.8}$$

The direction of the largest component $|V^c|$ defines the *main* principle axis which is along the crystal c-axis. The asymmetry parameter η ($0 \leq \eta \leq 1$) is then defined as

$$\eta = \frac{V^a - V^b}{V^c} \tag{2.9}$$

$$|V^c| > |V^b| > |V^a| \tag{2.10}$$

η is typically small $\eta \leq 0.06$ for the planar Cu site in the cuprates [69], and for both A and B-sites in $La_{2-x}Sr_xCuO_4$ [82]. The final expression for the observed NQR frequency $^{63}\nu_Q$ in the tetragonal phase is then given by

$$\begin{aligned} {}^{63}\nu_Q &= \frac{e^{63}Q}{2h}V^c\left(1+\eta^2/3\right)^{1/2} \\ &\simeq \frac{e^{63}Q}{2h}V^c \end{aligned} \tag{2.11}$$

for $\eta \leq 0.06$. The value of ^{63}Q used varies between groups, but is generally taken to be either $^{63}Q = -0.211$ barns [84] which is based on theoretical calculation, or $^{63}Q = -0.16$ barns [2] which is based on ESR measurements in cuprate salts. Since we are dealing with experimental results, we choose to use $^{63}Q = -0.16$ barns [2]. As discussed in appendix A, however, our calculation of the length scale $^{63}R_{patch}$ is insensitive to the absolute value of ^{63}Q used.

2.2.2 The spin-lattice relaxation, $^{63}1/T_1$

The dynamic properties are reflected in the nuclear spin-lattice relaxation rate, $^{63}1/T_1$. $^{63}T_1$ is the time scale for the nuclear spin system to return to thermal equilibrium after excitation by an applied r.f. pulse, as shown in Fig. 2-5. This time scale reflects the density of low energy magnetic fluctuations of the electronic system.

As long as the nuclear spin system may be described by a common spin temperature, $^{63}1/T_1$ may be written in terms of the transition rates W_{mn} between the nuclear states with energy E_m and E_n [81]

$$\frac{1}{T_1} = \frac{1}{2}\frac{\sum_{m,n} W_{mn}(E_m - E_n)^2}{\sum_m E_m^2} \tag{2.12}$$

The transition rate W_{mn} is determined by the external perturbations on the nuclear spin system. In these strongly magnetic copper-oxide materials, the most important contribution to $^{63}1/T_1$ is from the electron spin fluctuations via the electron-nuclear

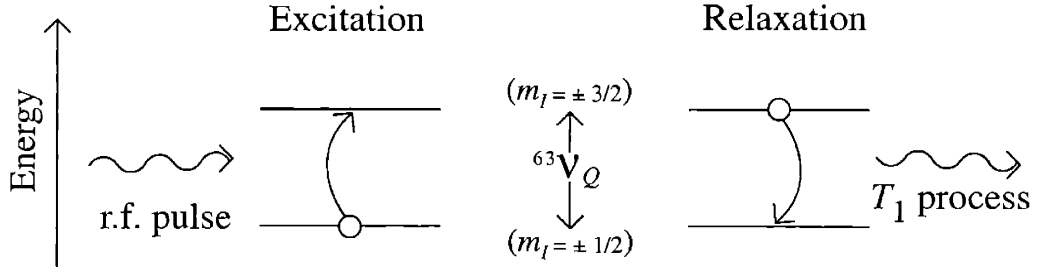

Figure 2-5: In order to measure $^{63}1/T_1$, we first excite the nuclei to the higher energy level state by an r.f. pulse and then monitor the relaxation of the nuclei back to thermal equilibrium. Energy is transferred out of the nuclear spin system by magnetic fluctuations at the resonance frequency $^{63}\nu_Q \simeq 36$ MHz.

hyperfine spin interaction. Note that while the transition rates W_{mn} are dominated by magnetic processes, the separation of the nuclear states $(E_m - E_n)/h = {}^{63}\nu_Q$ is determined by the EFG (Fig. 2-5).

The allowed transitions $(m_I \leftrightarrow m_I')$ in NQR for $I = 3/2$ are $(+1/2 \leftrightarrow +3/2)$ and $(-1/2 \leftrightarrow -3/2)$ [1,81]. $(+1/2 \leftrightarrow -1/2)$ is not allowed in NQR since the EFG cannot split the $\pm$ degeneracy (Fig. (2-5)) since it is of charge origin. Furthermore, $(-1/2 \leftrightarrow +3/2)$ and $(+1/2 \leftrightarrow -3/2)$ where $|\Delta m_I| = 2$ does not occur because $^{63}1/T_1$ is dominated by magnetic relaxation processes where only $|\Delta m_I| = 1$ is allowed.

In NQR, the direction along which the spin-lattice relaxation rate $^{63}1/T_1$ is measured is given by the main principle axis, i.e. the c-axis (Eq. (2.11)), and cannot be changed externally. Using Eq. (2.12), one can derive a general expression for $^{63}1/T_1^c$ with relaxation by a single magnetic process as such [61]

$$^{63}\left(\frac{1}{T_1}\right)^c = \frac{^{63}\gamma_n^2}{2}\sum_{\mathbf{q}}\left[\left|^{63}A(\mathbf{q})_{(\perp,1)}\right|^2 + \left|^{63}A(\mathbf{q})_{(\perp,2)}\right|^2\right]\mathbf{S}_\perp(\mathbf{q},\omega_n). \tag{2.13}$$

where $\omega_n/2\pi = {}^{63}\nu_Q \simeq 36$ MHz is the NQR frequency, and $\mathbf{q}$ is the reciprocal lattice vector. $^{63}A(\mathbf{q})_{(\perp,1)}$ (in units of kOe/μ_B) is the wave vector dependent hyperfine form

factor [75] in the first perpendicular direction to the main principle axis of the EFG (i.e. in the ab plane), and ${}^{63}A(\mathbf{q})_{(\perp,2)}$ to the second perpendicular direction (also in the ab plane). The hyperfine form factors are discussed below. $\mathbf{S}_{\perp}(\mathbf{q},\omega_n)$ is the F.T. of the ensemble average of the electron spin-spin correlator $\langle\{S(0,0)^{-},S(\mathbf{r},t)^{+}\}\rangle$ (in the ab plane) given by

$$\mathbf{S}_{\perp}(\mathbf{q},\omega_n)=\frac{1}{2\pi}\sum_{\mathbf{r_i}}\int_{-\infty}^{\infty}dt\cdot\exp\left[i(\mathbf{q}\cdot\mathbf{r_i}-\omega_n t)\right]\cdot\left\langle\left\{S(0,0)^{-},S(\mathbf{r_i},t)^{+}\right\}\right\rangle \qquad (2.14)$$

The summation r_i is over the lattice positions of the i electron spins. Using the fluctuation-dissipation theorem [99], we can express Eq. (2.14) in terms of the imaginary part of the spin susceptibility, $\chi''_{\perp}(\mathbf{q},\omega_n)$ (in units of emu/[mol f.u.]), as such

$$\chi''_{\perp}(\mathbf{q},\omega_n)=\frac{\omega_n}{T}\left(\frac{N_A\mu_B^2}{2k_B}\right)\mathbf{S}_{\perp}(\mathbf{q},\omega_n) \qquad (2.15)$$

Eq. (2.15) is valid in the limit $\hbar\omega_n \ll k_BT$, which is certainly the case for current experimental conditions where $\hbar\omega_n/k_B = 1-2$ mK.

The T_1 pulse sequence we used is shown in Fig. 2-6(b) where we measure ${}^{63}1/T_1$ by first applying a π pulse to invert the nuclear spin population at time $t=0$. We then wait for time t before measuring the "spin-echo sequence" (Fig. 2-6(a)). The T_1 pulse sequence can also be expressed as such

$$\pi - - - - t - - - - [\pi - \tau - \pi/2 - \tau] - echo \qquad (2.16)$$

The time dependence of the nuclear magnetisation $M(t)$ is determined by taking the integral of the *echo* in the time domain. ${}^{63}1/T_1$ is then determined by fitting $M(t)$ to the standard recovery form [64]

$$M(t)=M(\infty)+(M(0)-M(\infty))\cdot\left[\exp\left(-\frac{3}{T_1}t\right)\right] \qquad (2.17)$$

appropriate for NQR with nuclear spin $I=3/2$. The factor 3 in the exponential in Eq. (2.17) implies that the $I=3/2$ nucleus for NQR rotates 3 times faster than a

$I = 1/2$ nucleus for NMR. In Eq.(2.17), $M(0), M(\infty)$ and $^{63}1/T_1$ are free parameters determined using a non-linear least squares fitting package to the recovery data. An example of the recovery data $M(t)$ is shown in Fig. 2-6(c) at the center of the A-line for $La_{1.84}Sr_{0.16}CuO_4$ at 295 K, with a best fit shown as the solid curve where $^{63}1/T_1 = 2885\ s^{-1}$ is deduced. The time dependence of $M(t)$ fit well to a single value of $^{63}1/T_1$, implying that the spin-lattice relaxation rate is dominated by a single fluctuation mechanism. We determine that $^{63}1/T_1$ is dominated by a spin fluctuation mechanism by measuring $^{65}1/T_1$ for the ^{65}Cu isotope in non-isotope enriched samples for which we observe the ratio $\left[\frac{^{65}1/T_1}{^{63}1/T_1}\right] \simeq 1.15$. According to Eq. (2.13) where $1/T_1 \sim \gamma_n^2$ for spin processes, this implies that $\left[\frac{^{65}1/T_1}{^{63}1/T_1}\right] = \left[\frac{^{65}\gamma_n^2}{^{63}\gamma_n^2}\right] = 1.147$, which is consistent with experiment. If on the other hand the $^{63}1/T_1$ and $^{65}1/T_1$ were dominated by charge fluctuations then $1/T_1 \sim^n Q^2$. This would result in $\left[\frac{^{65}1/T_1}{^{63}1/T_1}\right] = \left[\frac{^{65}Q^2}{^{63}Q^2}\right] = 0.856$, which is not observed experimentally.

The length of the r.f. pulses, $t_{\pi/2}$ in Fig. 2-6(a,b), and the intensity of the r.f. pulses, H_1 (i.e. the peak height of the pulses), were chosen to satisfy the resonance condition [1]

$$^{63}\gamma_n' H_1 t_{\pi/2} = \pi/2. \tag{2.18}$$

γ_n' is the effective nuclear gyro-magnetic ratio which we determine using the following expression [1]

$$^{63}\gamma_n' = \sqrt{I(I+1) - m_I(m_I - 1)} \cdot ^{63}\gamma_n \tag{2.19}$$

for all quadrupole split transitions ($\{m_I - 1\} \leftrightarrow m_I$) with $m_I > 0$. $^{63}\gamma_n = 11.285$ MHz/Tesla is the bare nuclear gyro-magnetic ratio for ^{63}Cu. In the case of ^{63}Cu NQR $^{63}\gamma_n' = \sqrt{3} \cdot ^{63}\gamma_n$. Note that the factor $\sqrt{3}$ in $^{63}\gamma_n'$ accounts for the factor 3 in the recovery $M(t)$ in Eq. (2.17), given that $^{63}1/T_1 \propto (^{63}\gamma_n')^2$ according to Eq. (2.13) for spin relaxation. Once the resonance condition in Eq. (2.18) is satisfied, our results of $^{63}1/T_1$ were independent of the pulse length $t_{\pi/2}$ and $t_\pi = 2t_{\pi/2}$. Typically, we used a short pulse length $t_{\pi/2} \sim 3\mu s$, implying $H_1 \sim 40$ G.

Another experimental parameter in the T_1 and spin-echo pulse sequences (Fig. 2-6 and Eq. (2.16)) is the $(\pi/2 - \pi)$ pulse separation time τ. In the case of large

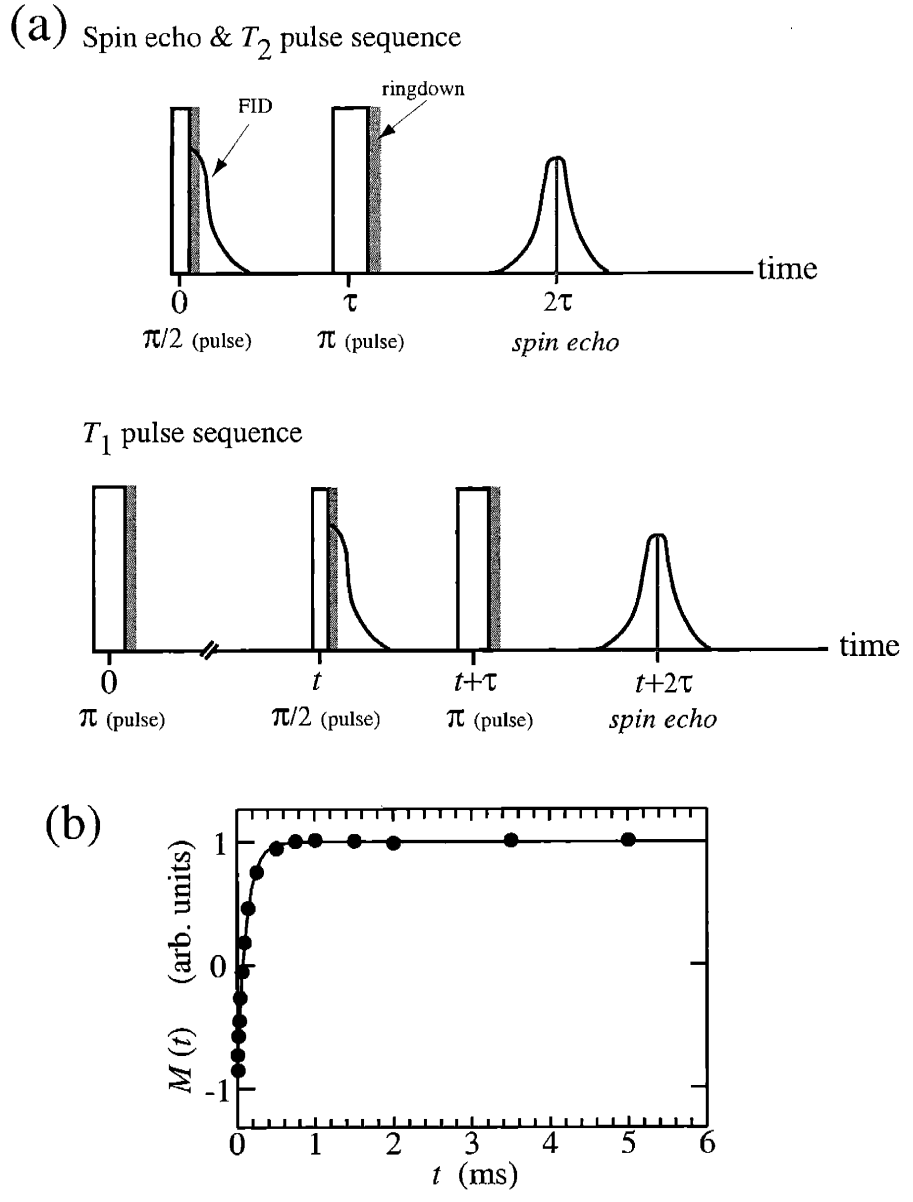

Figure 2-6: (a) The r.f. pulse sequence used for measuring the spin echo. (b) The r.f. pulse sequence used to measure $1/T_1$ where the time-integral of the spin-echo, $M(t)$ (i.e. the magnetisation), is measured as a function of delay time t. (c) An example of the recovery of $M(t)$ for $La_{1.84}Sr_{0.16}CuO_4$ at 295 K from which $^{63}T_1 = 0.3466$ ms is determined from the solid line fit. A fixed $\pi/2 - \pi$ pulse separation of $\tau = 12\mu$s was used for all data presented in this thesis.

doping $x \gtrsim 0.16$ and low temperatures $T \lesssim 150$ K, we found a slight dependence of $^{63}1/T_1$ depending on what value of τ was used. In the case of $x = 0.16$ at 100 K, increasing τ from 12 to 24 μs resulted in a roughly uniform ~ 10 % decrease in $^{63}1/T_1$ across the NQR line. In appendix B we show that the observed τ dependence of $^{63}1/T_1$ is a consequence of a multiple exponential recovery for $M(t)$. The multiple exponential recovery for $M(t)$ implies that there is a distribution in $^{63}1/T_1$ values at fixed frequency, i.e. there are multiple magnetic relaxation mechanisms for which the nuclei can relax back to thermal equilibrium. In the case of $x = 0.16$ at 100 K, we analyze the multiple exponential recovery for $M(t)$ and deduce the distribution in $^{63}1/T_1$ at fixed frequency. We also show that the distribution in $^{63}1/T_1$ can be naturally accounted for by an underlying intrinsic lattice broadening, $^{63}\Delta\nu_{latt}^{T1}$, which we calculate.

2.2.3 The Hyperfine Form Factors

The hyperfine form factor $^{63}A(\mathbf{q})_{(\perp,1)}$ arises from the geometry of the hyperfine couplings between the electron spin S and the nuclear spin I. Typically, the nuclear spin has significant hyperfine interaction only with the electron spin of its atom and nearest neighbor atoms. The hyperfine form factor is the Fourier transform of the local hyperfine interactions defined as [75]

$$^{63}A(\mathbf{q})_{\perp} = \sum_i {}^{63}A_{\perp}^{i} e^{i\mathbf{q}\cdot\mathbf{r}_i} \tag{2.20}$$

where the summation is over all electron spins, i, with hyperfine interaction $^{63}A_{\perp}^{i}$, and $\mathbf{r}_i$ is the vector from the atomic site of the electron spin to the nucleus.

The hyperfine interactions, $^{63}A^{i}$, are usually given in units of kOe/μ_B. A typical hyperfine interaction in copper-oxide materials is $|A(\mathbf{q})| \sim 100$ kOe/μ_B. This can be understood as an amount ~ 100 kOe of hyperfine magnetic field at the site of the nucleus produced by one Bohr magneton μ_B of bulk electron spin susceptibility. This method of specifying the hyperfine interaction has the advantage that it is a property of the electronic structure alone and does not depend on the nucleus used

to measure the field. Another unit for $^{63}A^i$ is in eV's, which typically corresponds to $g_\perp \gamma_n \hbar |A(\mathbf{q})| \sim 10^{-6}$ eV for a whole μ_B of susceptibility, where $g_\alpha \sim 2$ is the anisotropic electron g-factor.

The hyperfine form factor is important because it determines what wavevectors, $\mathbf{q}$, of electron spin fluctuations that $1/T_1$ is sensitive to. Differences in the hyperfine form factors for different nuclear sites can be used to obtain information about the wavevector dependence of the spin susceptibility. In these antiferromagnetic copper oxide compounds, the spin susceptibility at low energies is strongly peaked near the antiferromagnetic wave vector, $\mathbf{Q_{AF}} = (\pi/a, \pi/a)$ [29, 39, 73]. If the hyperfine form factor at the antiferromagnetic wave vector, $\mathbf{Q_{AF}}$, is non-zero, then $1/T_1$ is sensitive to the antiferromagnetic spin fluctuations as in the case of ^{63}Cu NQR. If the hyperfine form factor is 0 at $\mathbf{Q_{AF}}$, then antiferromagnetic fluctuations do not affect $1/T_1$. Typically in copper oxide materials, copper $^{63}1/\mathrm{T}_1$ does measure antiferromagnetic electron spin fluctuations, but the planar oxygen ^{17}O, $^{17}1/\mathrm{T}_1$, does not.

This can be seen by looking at the typical hyperfine form factors for copper and oxygen in these materials, as shown in figure 2-7. For a copper nucleus, a hyperfine field, A_α in the spatial direction α, is produced by the onsite electron spins. The hyperfine interaction between the electron spins and the nucleus can be divided into four different contributions [2, 57].

$$A_\alpha = A^{contact} + A^{cp} + A_\alpha^{dipole} + A_\alpha^{spin-orb} \tag{2.21}$$

The first contribution is the contact interaction, $A^{contact}$, which expresses the interaction for s-like orbitals, which have some probability for the electron to be at the site of the nucleus. This leads to a relatively large interaction proportional to the probability for the electron to be at the nucleus site. The second contribution, A^{cp}, is from core polarization. Even if the electron spins are not in an s-like orbital, the polarization of the outer electrons may cause a small polarization of the inner (core) electrons, which interact with the nucleus. Typically, this core polarization effect is negative because the core electrons are polarized opposite to the outer electron spins.

These first two contributions are isotropic because s-like orbitals have an isotropic probability distribution.

The last two terms in Eq. (2.21) are from non-s orbitals which are anisotropic. The third effect is the dipolar interaction between the electron and nuclear spins, A_α^{dipole}. The fourth interaction, $A_\alpha^{spin-orb}$, arises from the spin-orbit interaction of the electron spin magnetic moment and the electron orbital magnetic moment. This interaction polarizes some of the orbital magnetic moment when the electron spin is polarized and this orbital magnetic moment interacts with the nuclear spin.

In addition, the nearest neighbor copper spins also contribute a significant hyperfine field, B. This hyperfine field from the nearest neighbor copper spins is discussed by F. Mila and T.M. Rice [57] as arising from the hybridization of the copper electron orbitals to include the 4s orbital of the nearest neighbor copper ions. This means that the copper electrons spend some time on the 4s orbital of the neighboring copper ions, thus providing an isotropic contact hyperfine interaction, B, with the neighboring copper nuclei. It is this contribution from the off site electron spins which creates a wavevector dependence in the hyperfine form factor. It is simple to see from Fig. 2-7 that for wavevector $\mathbf{q} = 0$ where all the electron spins point the same direction, ${}^{63}A(\mathbf{q} = \mathbf{0})_\alpha = A_\alpha + 4B$, which for the perpendicular direction ${}^{63}A(\mathbf{q} = \mathbf{0})_\perp \simeq 206$ kOe/μ_B [36]. For antiferromagnetic wavevector $\mathbf{Q}$ where the electron spins alternate directions, ${}^{63}A(\mathbf{q} = \mathbf{Q_{AF}})_\alpha = A_\alpha - 4B$, which for the perpendicular direction ${}^{63}A(\mathbf{q} = \mathbf{Q_{AF}})_\perp \simeq -130$ kOe/μ_B [36]. The full wavevector dependence is given by

$$ {}^{63}A(\mathbf{q})_\alpha = A_\alpha + 2B\left(\cos(q_x a) + \cos(q_y a)\right) \tag{2.22} $$

The oxygen atoms in the copper oxide planes are located in the middle between two copper atoms. These two copper atoms both contribute a hyperfine field, C_α, at the oxygen nuclear site as shown in Fig. 2-7. For wavevector $\mathbf{q} = 0$, ${}^{17}A(\mathbf{q} = 0)_\alpha = 2C_\alpha$. For the antiferromagnetic wavevector $\mathbf{Q_{AF}}$ where the electron spins alternate

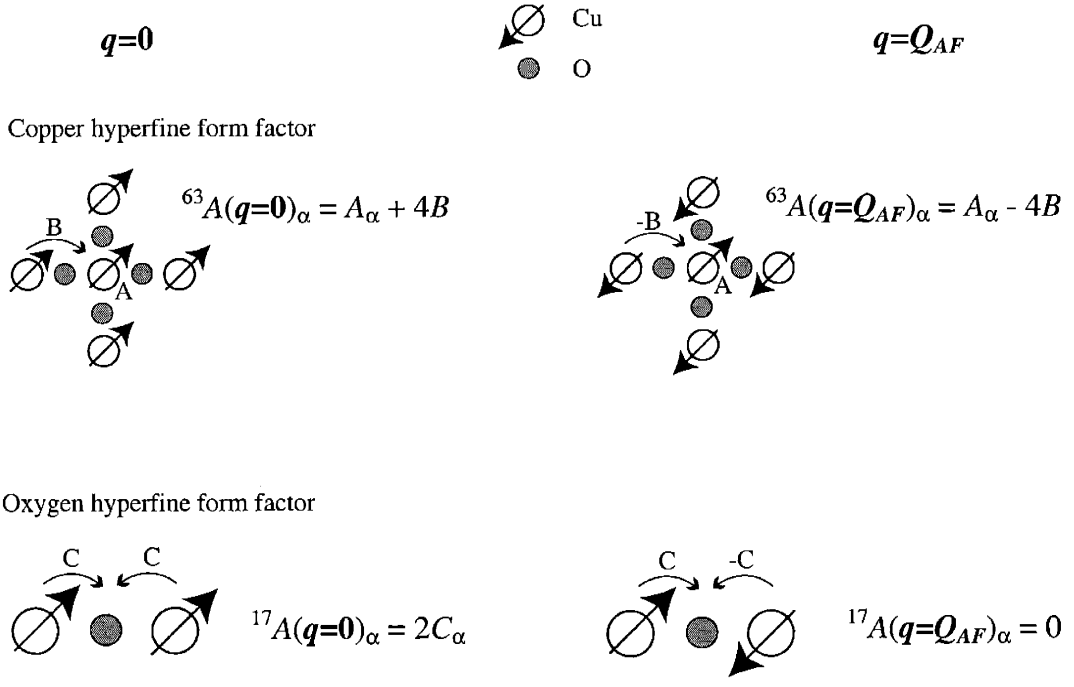

Figure 2-7: Hyperfine form factors, $A(\mathbf{q})_\alpha$, in the α spatial direction, for copper $^{63}A(\mathbf{q})$ and oxygen $^{17}A(\mathbf{q})$ atoms in the copper-oxide materials. Left hand side illustrates $A(\mathbf{q}=\mathbf{0})_\alpha$ and right hand side illustrates $A(\mathbf{q}=\mathbf{Q_{AF}})_\alpha$. Full wavevector dependence given in Eq. (2.22) and Eq. (2.23).

directions, ${}^{17}A(\mathbf{q}=\mathbf{Q_{AF}})_\alpha = 0$. The full wavevector dependence is

$$ {}^{17}A(\mathbf{q})^\alpha = \left[2C^{//}\cos\left(\frac{q_x a}{2}\right), 2C^{\perp}\cos\left(\frac{q_y a}{2}\right), 2C^{c}\cos\left(\frac{q_z c}{2}\right)\right] \tag{2.23} $$

where it is convenient in the case of oxygen to label the three distinct crystal axes as such: the first is along the Cu-O-Cu bond direction which we denote as // since it is parallel to the bond, another is along the c-axis which we denote as c, and the last is perpendicular to both // and c which we denote as $\perp$. According to Ref. [80], we find

$$ \left[2C^{//}, 2C^{\perp}, 2C^{c}\right] = [146, 89, 88] \tag{2.24} $$

in units of kOe/μ_B. It is also found that the hyperfine coupling constants for both ^{63}Cu and ^{17}O are the same in $La_{2-x}Sr_xCuO_4$ [36,59] and $YBa_2Cu_3O_y$ [91].

To summarize, there is a large contribution to ${}^{63}1/T_1$ from the anit-ferromagnetic wavevector $\mathbf{Q_{AF}} = (\pi/a, \pi/a)$. Since $\chi''_\perp(\mathbf{q}, \omega_n)$ is peaked in the vicinity of $\mathbf{q} = \mathbf{Q_{AF}}$, this implies that ${}^{63}1/T_1$ NQR is a local probe of the low frequency antiferromagnetic spin fluctuations in the plane. In the case of ^{17}O, there is no contribution to ${}^{17}1/T_1$ $\mathbf{q} = \mathbf{Q_{AF}}$, rather, ${}^{17}1/T_1$ is dominated spin fluctuations in the vicinity $\mathbf{q} \approx \mathbf{0}$.

2.3 NQR/NMR electronics

The NQR and NMR measurements were conducted using state-of-the-art equipment with particularly good signal to noise. The electronics, shown in Fig. 2-8, are required to do two things. Firstly, they send out the r.f. pulses to excite and resonate the nuclei in the sample and at a later in time when the nuclear spin echo forms, the echo signal is acquired. The echo signal is typically very low intensity and much care has to taken to reduce unwanted r.f. noise. Our NQR/NMR spectrometer is based around the Aries spectrometer by Tecmag ©, which communicates with the Macintosh © computer. The general flow of the electronics is as follows. The r.f. frequency source (PTS 310 or 500) produces continuous r.f. which is gated into pulses by the TTL signals from the Aries spectrometer. These r.f. pulses are then amplified

by the power amplifier (Kalmus LP1000, 1 kW) to peak voltages of up to 300 V. The amplified r.f. pulses are fed through paired diodes into the NQR/NMR probe. The NQR/NMR probe consists of two adjustable capacitors and an inductive coil. This allows the circuit to be tuned to the chosen r.f. frequency and also matched to 50 ohms impedance of the co-axial cables. In appendix C we discuss the simple circuit theory behind the resonance condition of the parallel capacitance/inductance circuit. The sample is placed inside the inductive coil, and is thus exposed to the RF oscillations of the magnetic field of the inductor.

The next two parts beyond the NQR/NMR probe help shield the sensitive signal amplifiers from the large r.f. pulses. A quarter-wavelength ($\lambda/4$) cable is inserted between the NQR/NMR probe and paired diodes that are grounded. Typically for 50 Ω co-axial cable, $\lambda/4 \simeq 45/\nu$ for the $\lambda/4$ in m and ν is the resonance frequency in MHz. The grounded diodes prevent the large voltages of the RF pulses from entering the signal amplifiers. Since a quarter-wavelength is the distance between the zero voltage point of the wave and the peak voltage, the quarter-wavelength cable allows the voltage to be large at the NQR/NMR probe while the voltage is small at the grounded diodes.

For acquiring the signal, the same inductive coil also provides an induced voltage $\sim \mu$V from the nuclear spin precession. The signal is not attenuated by the grounded diodes as long as the signal is below the threshold voltage of the diodes ($\sim$0.6 V). The signal is amplified by the r.f. signal amplifiers (LN-2L or LN-2M by Doty). Generally, we have two Doty amplifiers which are separated by a pair of r.f. mixers (Mini-circuits ZAD-1) which we use as switches. The switches are only turned on when we want to acquire the signal to avoid unnecessary saturation of the amplifiers. For the third r.f. amplifier, we use a Mini-circuits ZFL-500LN. This amplified signal is then split (Mini-circuits ZFSC-2-1W) and mixed with the original continuous r.f. with two different phases, ϕ =0 and ϕ =90 degrees. This is referred to in the NQR/NMR literature as quadrature detection. Mixing with the two different phases essentially allows us to get both the cosine and sine components of the signal at the chosen frequency (or equivalently the real and imaginary parts of the Fourier transform). After mixing

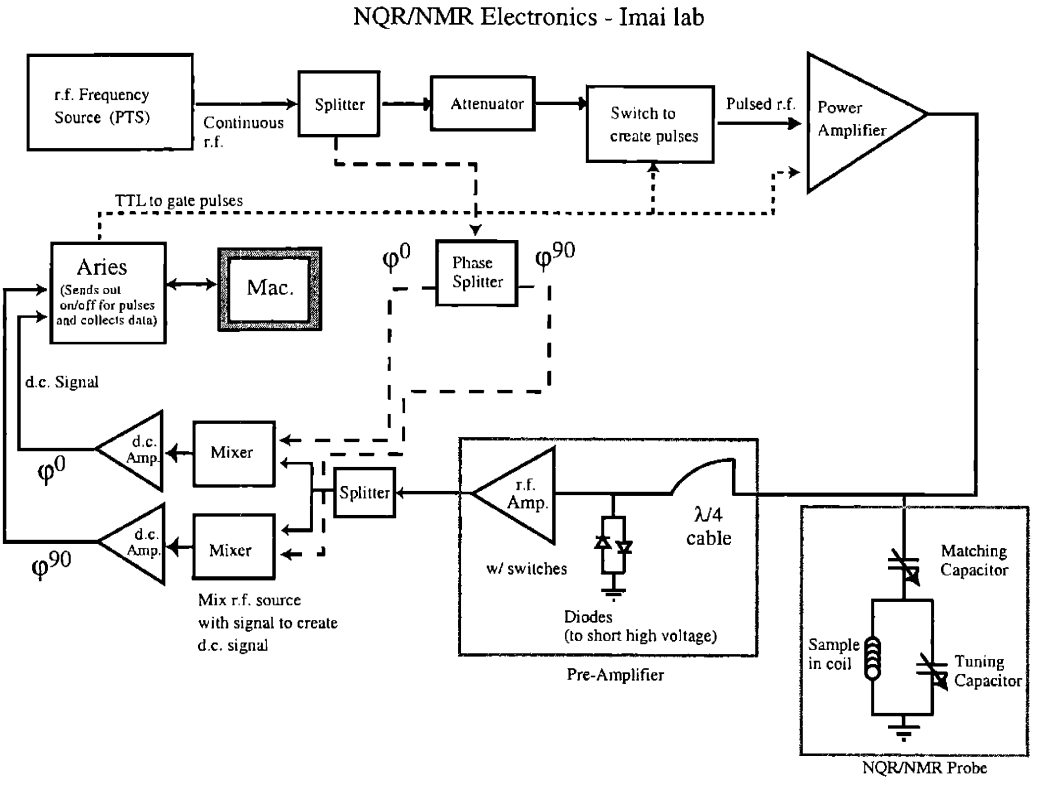

Figure 2-8: Schematic of electronics for NQR/NMR spectrometer, Imai Labs.

with the original r.f., the signal is close to d.c.. We amplify the signal once more with an op-amp (AD521) based circuit with a gain of 100 and a complementary bandwidth of ~100 kHz. This final signal can be viewed on an oscilliscope and is digitized by the Aries spectrometer. In addition to the software provided with the Aries spectrometer, K.R. Thurber wrote some additional functions to provide the data analysis that we needed.

A NQR/NMR technique that is crucial for separation of the small spin echo signal from the decay (ringdown) of the r.f. pulses is phase cycling [68]. In our resonant circuit (Q ~50 for Cu NQR) (see appendix C), the r.f. pulses require some time to decay and can obscure the spin echo signal. The pulse sequences shown in Fig. 2-6 are repeated with different phases for the r.f. pulses in order to cancel the decay of

the r.f. pulse. For example, for the spin echo sequence, we use four different phases and add or subtract the resulting signal based on the sign of the echo:

$(\pi/2)_{+x}$	τ	$(\pi)_{+x}$	τ	echo_{+x}	Add
$(\pi/2)_{-x}$	τ	$(\pi)_{+x}$	τ	echo_{-x}	Subtract
$(\pi/2)_{-x}$	τ	$(\pi)_{+y}$	τ	echo_{+x}	Add
$(\pi/2)_{+x}$	τ	$(\pi)_{+y}$	τ	echo_{-x}	Subtract

where $(\pi/2)$ and (π) refer to the 90 degree and 180 degree pulses with the subscript indicating the phase of the r.f. pulse. In this sequence, any ringdown of the 90 degree or 180 degree pulses is cancelled. For the T_1 sequence, we have an additional π pulse. We repeat the above four phase sequence twice, once with $(\pi)_x$ for the first π degree pulse, and again with $(\pi)_{-x}$. In addition to cancelling any ringdown of the pulses, this also cancels the stimulated echoes that can occur with three pulses [68]. The phase cycling technique dramatically helps to measure the spin echo at short $\tau \sim 12\mu$s in the case of ^{63}Cu NQR.

Chapter 3

^{63}Cu NQR Experimental Results

Due to the experimental ease of the measurement, the temperature dependence of $^{63}1/T_1$ is generally only measured at the peak of the ^{63}Cu NQR or NMR spectrum. The most striking feature of our ^{63}Cu NQR data we present in this chapter, however, is that $^{63}1/T_1$ shows qualitatively different *temperature dependence* depending on where along the NQR line it is measured [79]. As we shall show, this implies , without invoking any kind of model, that certain regions of the CuO_2 plane are more metallic while others are more insulating.

In order to measure the frequency dependence in $^{63}1/T_1$ and obtain any quantitative information over a wide temperature range, it is *essential* to separate the signal from 63 and 65 isotopes. Previous work by S. Fujiyama *et al.* [22] measured $^{(63,65)}1/T_1$ for naturally abundant Cu in which they successfully deduced that a substantial frequency dependence exists across the $^{(63,65)}$Cu NQR spectrum, however, no statement beyond that could be inferred in particular regarding the temperature dependence.

In Fig. 3-1 we explicitly show the frequency dependence of $^{63}1/T_1$ across the ^{63}Cu NQR line at a fixed temperature of 295 K. We first remark on the overlap between samples with different nominal hole concentration x, shown in Fig. 3-1(b). Taking $x = 0.115$ as an example, we see that the upper (lower) half intensity point of the $x = 0.115$ A and B-lines roughly coincides with the peaks of the $x = 0.16(0.07)$, which implies that the characteristic local hole concentration $^{63}x_{local}$ is given by $^{63}x_{local} \leq 0.16$ in more metallic regions, while is given by $^{63}x_{local} \geq 0.07$ in more insulating

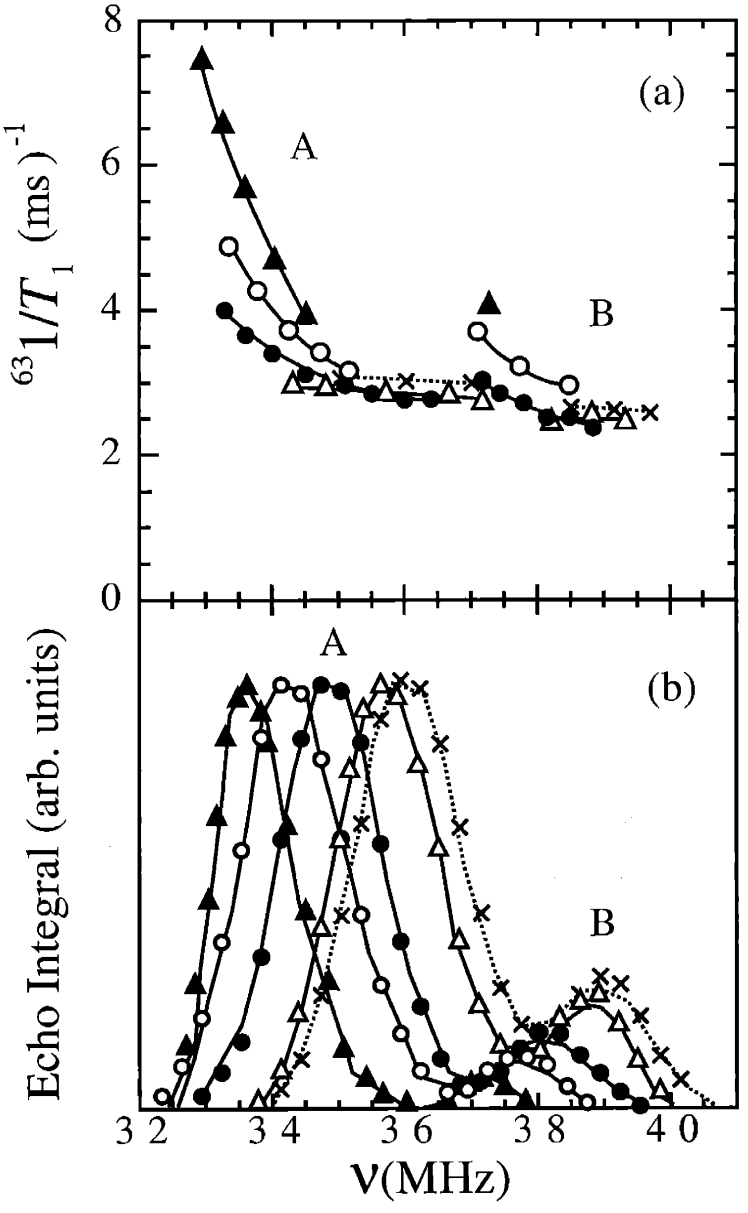

Figure 3-1: (a) Frequency dependence of $^{63}1/T_{1,A}$ and $^{63}1/T_{1,B}$ across the A and B-lines of the ^{63}Cu NQR spectrum of ^{63}Cu isotope enriched $La_{2-x}Sr_xCuO_4$ for $x = 0.20$ ($\times$), $x = 0.16$ ($\triangle$), $x = 0.115$ ($\bullet$), $x = 0.07$ ($\circ$) and $x = 0.04$ ($\blacktriangle$). All data is at 295 K. Solid curves in (a) are a guide for the eye. (b) ^{63}Cu NQR spectrum of the A and B-lines where the same symbols as (a) are used. Solid curves in (b) are calculated fits using patch-by-patch model of spatial variation in local hole concentration $^{63}x_{local}$ with a lower bound for the patch radius (using d_1 dopants) of $^{63}R_{patch} = 2.1 - 3.1$ nm for increasing x, respectively.

regions. The reason why only an upper boundary for $^{63}x_{local}$ can be deduced, is that we are assuming that the linewidths in Fig. 3-1(b) are dominated by $^{63}x_{local}(\neq x)$ alone. In fact, as we calculate in chapter 4, there is a substantial intrinsic lattice broadening defined as $^{63}\Delta\nu_{latt}$ which is independent of the broadening arising from $^{63}x_{local}$. $^{63}\Delta\nu_{latt}$ originates from the distribution in local EFG values due to the random positioning of $^{+2}$Sr ions in the lattice, and we calculate its size by using a point charge lattice summation. In Fig. 3-2 we illustrate the extent of $^{63}\Delta\nu_{latt}$ as the dashed curves, which is comparable to the full experimentally observed broadening shown as the data points. The influence of $^{63}\Delta\nu_{latt}$ convoluted with that of $^{63}x_{local}$ complicates our analysis. Therefore, in order to get a better estimate of $^{63}x_{local}$ using ^{63}Cu NQR, we must measure $^{63}1/T_1$ at various positions across the line as shown in Fig. 3-1(a).

Before proceeding to the main results for $^{63}1/T_1$, we define the values of $^{63}1/T_{1,A}$ and $^{63}1/T_{1,B}$ taken at various positions across the NQR lineshape shown in Fig. 3-2: $^{63}1/T_{1,A}^{(0)}$ defines $^{63}1/T_1$ measured at the CG (center of gravity) of the A-line, $^{63}1/T_{1,A}^{(+)}$ defines $^{63}1/T_1$ measured at the half intensity of the upper (+) frequency side of the A-line, $^{63}1/T_{1,A}^{(-)}$ at the lower half intensity side, and $^{63}1/T_{1,A}^{(-1/10)}$ at the lower one-tenth intensity of the A-line. We shall use these definitions to determine $^{63}x_{local}$ as a function of temperature and x. In Fig. 3-2 we also define the corresponding quantities for $^{63}1/T_1$ across the B-line, and we shall show that $^{63}1/T_1$ across the B-line yields consistent values of $^{63}x_{local}$ to the A-line.

3.1 $^{63}1/T_1$ at the CG of the NQR spectrum

Our ultimate goal is to extract $^{63}x_{local}$ from the frequency dependence of $^{63}1/T_1$ across the NQR spectrum of the A or B-lines. However, in order to do so, we must first make a systematic study of $^{63}1/T_{1,A}^{(0)}$ and $^{63}1/T_{1,B}^{(0)}$ measured at the CG of the A and B-line respectively (labelled in Fig. 3-2). In our analysis, $^{63}1/T_{1,A}^{(0)}$ and $^{63}1/T_{1,B}^{(0)}$ both represent the spin-lattice relaxation rates of the nominal hole concentration x, regardless of the underlying broadening. Once a systematic study of the temperature

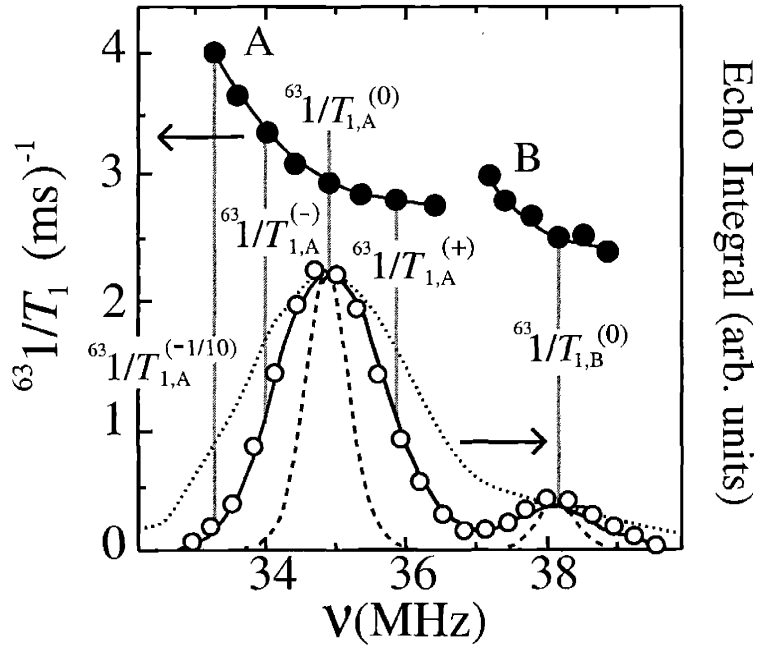

Figure 3-2: Frequency dependence of $^{63}1/T_{1,A}$ and $^{63}1/T_{1,B}$ (•) across ^{63}Cu NQR lineshape (○) for $x = 0.115$ at 295 K taken from Fig. 3-1. We also define $^{63}1/T_{1,A}^{(-1/10)}$, $^{63}1/T_{1,A}^{(-)}$, $^{63}1/T_{1,A}^{(0)}$, and $^{63}1/T_{1,A}^{(+)}$ at the lower one-tenth, the lower half, the CG (center of gravity), and upper half intenisty position of the A-line, along with $^{63}1/T_{1,B}^{(0)}$ at the CG of the B-line. Curves show fit using patch-by-patch model with a lower bound for the patch radius of $^{63}R_{patch} = 1.6$ nm (dotted curve), $^{63}R_{patch} = 2.6$ nm (solid curve), and $^{63}R_{patch} = \infty$ (dashed curve).

and x dependence of ${}^{63}1/T_{1,A}^{(0)}$ and ${}^{63}1/T_{1,B}^{(0)}$ is made, we can then make quantitative statements from the frequency dependence of ${}^{63}1/T_{1,A}$ and ${}^{63}1/T_{1,B}$ from the nominal values at the CG, and thereby determine ${}^{63}x_{local}$ as a function of temperature.

In Fig. 3-3 and Fig. 3-4 we present the temperature dependence of ${}^{63}1/T_{1,A}^{(0)}$ (shown as the data points in Fig. 3-3) and ${}^{63}1/T_{1,B}^{(0)}$ (shown as the data points in Fig. 3-4), respectively. While the solid curves through the ${}^{63}1/T_{1,A}^{(0)}$ data in part Fig. 3-3 are guides for the eye, the solid curves in part Fig. 3-4 represent $\left(\epsilon \cdot {}^{63}1/T_{1,A}^{(0)}\right)$ taken from part Fig. 3-3. We plot part Fig. 3-4 as such to be able to directly compare the temperature dependence of $\left(\epsilon \cdot {}^{63}1/T_{1,A}^{(0)}\right)$ with ${}^{63}1/T_{1,B}^{(0)}$, where ϵ is a uniform scaling factor taken to be $\epsilon = [0.87, 0.87, 0.90, 0.84]$ for $x = [0.20, 0.16, 0.115, 0.07]$, respectively. As shown in part Fig. 3-4, we find semi-quantitatively the same temperature dependence between the CG of the A and B-lines, with an overall 10 - 16 % smaller value of ${}^{63}1/T_{1,B}$ compared to ${}^{63}1/T_{1,A}$, i.e. ${}^{63}T_{1,A}/{}^{63}T_{1,B} = 0.9 - 0.84$. Previous reports in *non*-isotope enriched samples [40, 41] also found that ${}^{63}T_{1,A}/{}^{63}T_{1,B} < 1$.

At first glance of Fig. 3-4, our data for $x = 0.16$ and $x = 0.20$ below $\sim$ 150 K may suggest that the ratio ${}^{63}T_{1,A}/{}^{63}T_{1,B}$ tends to decrease $\sim 10 - 15$ % with decreasing temperature, similar to previous trends reported in [40] for $x = 0.20$. We point out, however, that it is dangerous to attach any great significance to the such changes in the ratio ${}^{63}T_{1,A}/{}^{63}T_{1,B}$ for the following reasons: first note that we use the same experimental conditions at all temperatures, namely, we fix the pulse separation time at $\tau = 12\mu$s (Eq. (2.16)). However, in the case where ${}^{63}1/T_1$ is distributed at fixed frequency (which we observed to be for $x = 0.16$ and $x = 0.20$ below $\sim$ 150 K (appendix B)), using a finite τ results in a smaller contribution from Cu nuclei with large spin-spin relaxation rates ${}^{63}1/T_2 (> {}^{63}1/T_1)$ which have correspondingly large values of ${}^{63}1/T_1$. Therefore, ${}^{63}1/T_1$ will always tend to be underestimated from the bulk average in cases when it is distributed and a finite pulse separation time τ is used. The extent of the underestimation of ${}^{63}1/T_1$ depends on the extent of the distribution in ${}^{63}1/T_1$ itself, the value of τ that is used, and also the exact correspondence between the distribution in ${}^{63}1/T_1$ and the distribution in spin-spin relaxation rate ${}^{63}1/T_2$. We note, however, that in order to retain the maximum possible signal intensity

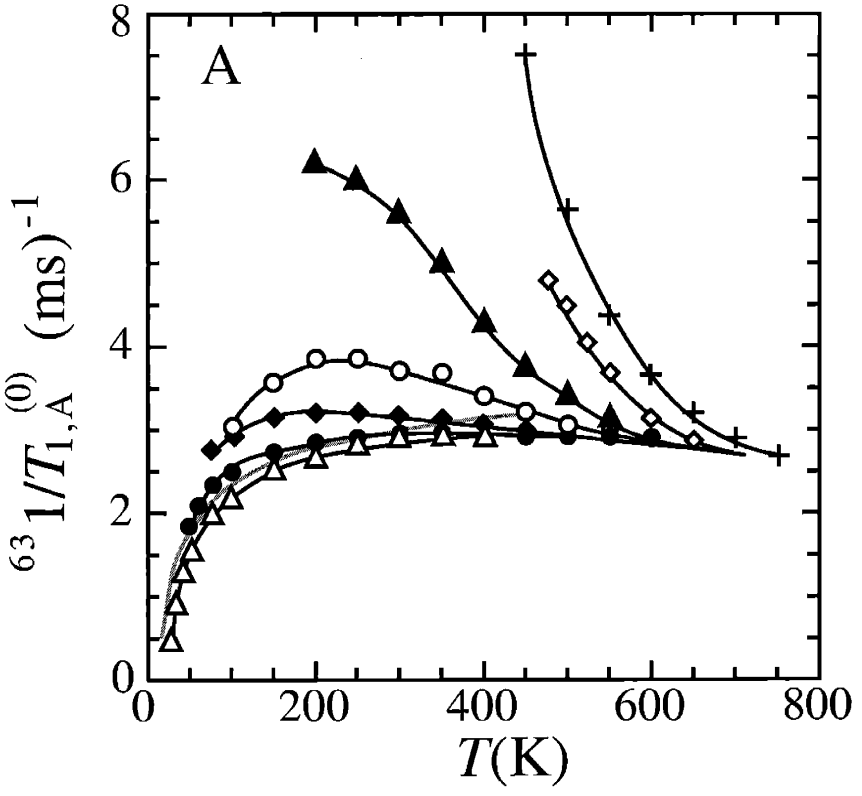

Figure 3-3: Temperature dependence of $^{63}1/T_{1,A}^{(0)}$ at the CG (center of gravity) of the A-line for $x = 0.20$ (solid grey line), $x = 0.16$ ($\triangle$), $x = 0.115$ ($\bullet$), $x = 0.09$ ($\blacklozenge$), $x = 0.07$ ($\circ$), $x = 0.04$ ($\blacktriangle$), $x = 0.02$ ($\diamond$), and $x = 0.0$ (+). All data are taken above the ^{63}Cu wipeout temperature T_{NQR} using a fixed pulse separation time $\tau = 12$ μs. Solid black curves are a guide for the eye.

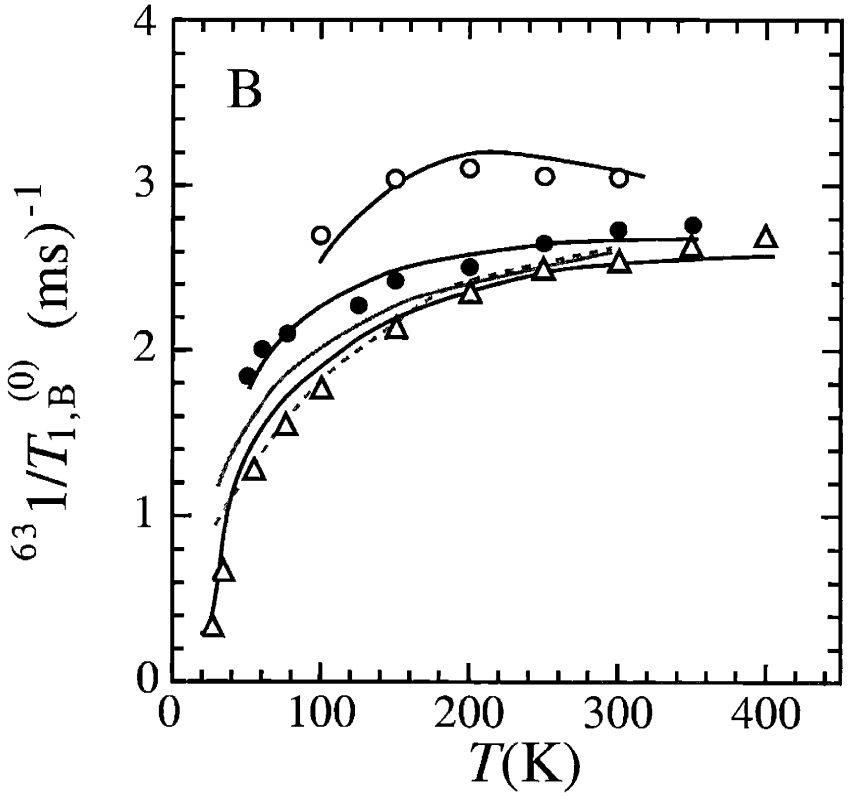

Figure 3-4: Temperature dependence of $^{63}1/T_{1,B}^{(0)}$ at the CG of the B-line where the same data symbols from part Fig. 3-3 are used, together with the black solid lines which represent $(\epsilon \cdot {}^{63}\, 1/T_{1,A}^{(0)})$ data taken directly from part Fig. 3-3 with a uniform scaling factor ϵ, where $\epsilon = [0.87, 0.87, 0.90, 0.84]$ for $x = [0.20, 0.16, 0.115, 0.07]$, respectively. Gray dashed line represents $^{63}1/T_{1,B}^{(0)}$ for $x = 0.20$.

and measure the most representative value of $^{63}1/T_1$ in each case, we always use the shortest possible value $\tau = 12\mu s$ the experiment allows.

We also recall that with decreasing temperature the spin-spin relaxation rate tends to get faster and faster for both the A and B-lines, and eventually leads to the onset of ^{63}Cu NQR wipeout at T_{NQR} [20, 31, 32, 77]. This implies that using fixed τ conditions will result in increased underestimations of $^{63}1/T_1$ with decreasing temperature. These changes in the underestimation of $^{63}1/T_1$ would be the same for both the A and B-lines provided that the ratio of the spin-spin relaxation rates between the A and B-lines remain constant with decreasing temperature, and furthermore, provided that the curvature of the spin-spin relaxation decay were constant with decreasing temperature. However with decreasing temperature, it is known that the Gaussian like component of the spin-spin relaxation rate tends to get smaller while the Lorenztian like component becomes more dominant, and eventually below T_{NQR}, the spin-spin relaxation rate becomes totally Lorentzian like [20, 31, 32, 77]. These factors have to be properly accounted when deducing meaningful information from the temperature dependence of $^{63}T_{1,A}/^{63}T_{1,B}$. Ideally, if one knew the exact correspondence between the distribution in $^{63}1/T_1$ and the distribution in *both* components of the spin-spin relaxation rate at both the A and B-sites, one could in principle adjust τ as a function of temperature and obtain a meaningful ratio $^{63}T_{1,A}/^{63}T_{1,B}$.

3.2 Frequency Dependence of $^{63}1/T_1$ and $^{63}x_{local}$

In Fig. 3-5 we follow the temperature dependence of $^{63}1/T_{1,A}$ measured at various positions across the A-line labelled in Fig. 3-2. In the background of Fig. 3-5 we also show $^{63}1/T_{1,A}^{(0)}$ taken directly from Fig. 3-3 which represent curves of constant x. The most surprising discovery of the present work is that $^{63}1/T_1^{(+)}$, $^{63}1/T_1^{(-)}$ and $^{63}1/T_1^{(-1/10)}$ all show *qualitatively and quantitatively different* temperature dependence. For example with $x = 0.07$, $^{63}1/T_1^{(+)}$ exhibits semi-quantitatively the same behaviour as $^{63}1/T_{1,A}^{(0)}$ for $x = 0.115$, while $^{63}1/T_1^{(-)}$ for $x = 0.07$ exhibits semi-quantitatively the same behaviour as $^{63}1/T_{1,A}^{(0)}$ for $x = 0.04$. This is consistent with

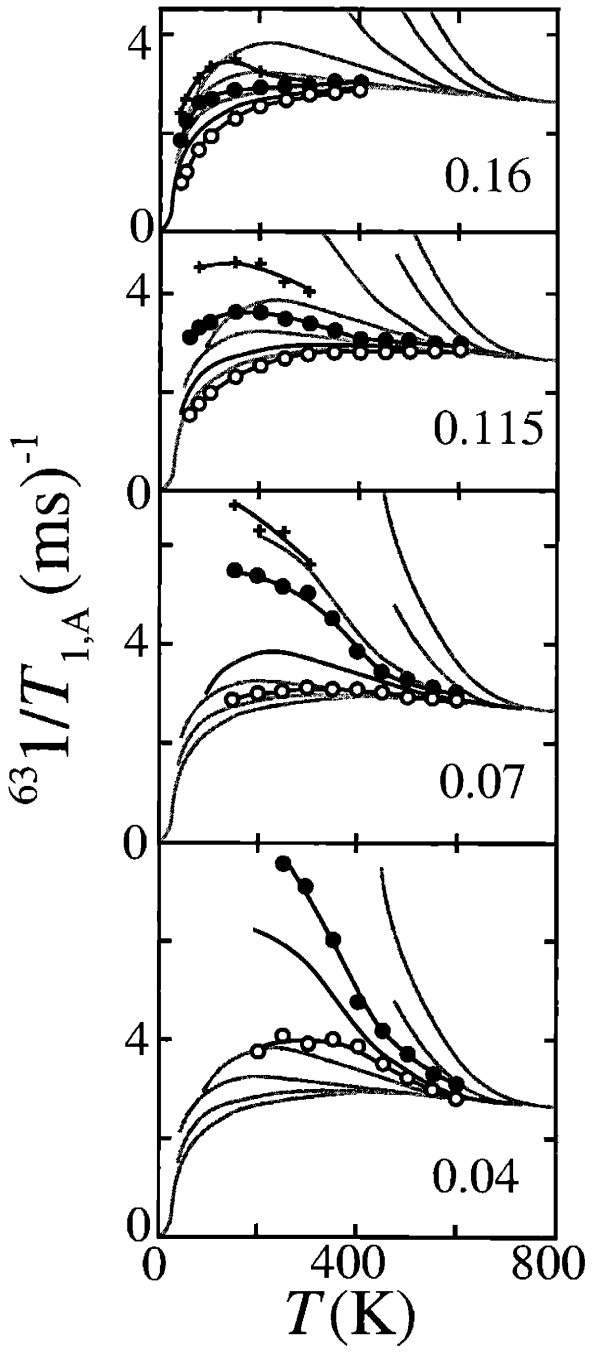

Figure 3-5: Temperature dependence of $^{63}1/T_{1,A}^{(-1/10)}$ (×), $^{63}1/T_{1,A}^{(-)}$ (•), $^{63}1/T_{1,A}^{(0)}$ (black curve), and $^{63}1/T_{1,A}^{(+)}$ (○) for nominal hole concentration x given in each panel. Gray curves are $^{63}1/T_{1,A}^{(0)}$ for $x = 0.00$, 0,02, 0.04, 0.07 ,0.09, 0.115, and 0.16 where $^{63}1/T_{1,A}^{(0)}$ monotonically decreases with increasing x.

the fact that the upper (lower) frequency side of the NQR spectrum for $x = 0.07$ roughly coincides with the peak NQR frequency of $x = 0.115$ ($x = 0.04$) respectively, as shown in Fig. 3-1. We also note that with decreasing temperature, $^{63}1/T_1^{(+)}$, $^{63}1/T_1^{(-)}$ and $^{63}1/T_1^{(-1/10)}$ do not exactly follow $^{63}1/T_{1,A}^{(0)}$ for a given x, which indicates that $^{63}\Delta x_{local}$ is growing with decreasing temperature.

In Fig. 3-6 we illustrate the details of the process used to extract $^{63}x_{local}$ from the data in Fig. 3-5. We first take the data from Fig. 3-5 and plot $^{63}1/T_{1,A}^{(+)}$, $^{63}1/T_{1,A}^{(-)}$ and $^{63}1/T_{1,A}^{(0)}$ for each x at a fixed temperature of 295 K. For clarity we connect the $^{63}1/T_{1,A}$ data at fixed x by the dashed black lines. We then create a smooth interpolation of $^{63}1/T_{1,A}^{(0)}$ for all x shown by the solid grey curve. Next, we show the process used to determine $^{63}x_{local}$ explicitly in the case of $x = 0.07$ shown as the solid black vertical and horizontal lines. In the case of $^{63}1/T_1^{(+)}$, the horizontal black line determines what value of $^{63}1/T_{1,A}^{(0)}$ (solid grey curve) corresponds to $^{63}1/T_1^{(+)}$, then the vertical line gives $^{63}x_{local}$ in the more metallic regions $^{63}x_{local}^{(+)} = 0.10$. A similar procedure for $^{63}1/T_1^{(-)}$ gives $^{63}x_{local}$ in the more insulating regions $^{63}x_{local}^{(-)} = 0.043$. The upper and lower frequency side therefore yield a consistent deviation $^{63}\Delta x_{local} = 0.028 \pm 0.001$ from the nominal concentration $x = 0.07$, where $^{63}\Delta x_{local}$ is defined as such

$$^{63}x_{local} = x \pm ^{63}\Delta x_{local} \tag{3.1}$$

$^{63}\Delta x_{local}$ represents the characteristic amplitude or extent of the spatial variation $^{63}x_{local}$. Note that we consistently define $^{63}\Delta x_{local}$ (and therefore $^{63}x_{local}$) with respect to the half intensities of the NQR spectrum. However, similar analysis using $^{63}1/T_{1,A}^{(-1/10)}$ yields a uniform 20-40 % increase in our estimate of $^{63}\Delta x_{local}$ and does not effect our conclusions.

We then determine $^{63}x_{local}^{(+)}$ and $^{63}x_{local}^{(-)}$ for all x depending on available $^{63}1/T_{1,A}^{(0)}$ data and desired accuracy. For instance, we cannot determine $^{63}x_{local}^{(-)}$ for $x = 0.04$ since we do not have $^{63}1/T_{1,A}^{(0)}$ data below $x = 0.04$ at 295 K. The reason for this is that 295 K corresponds to the wipeout temperature T_{NQR} for $x \leq 0.035$ [31] (see chapter 6), and we can only determine $^{63}x_{local}^{(-)}$ from our data for $T \geq T_{NQR}$ where full

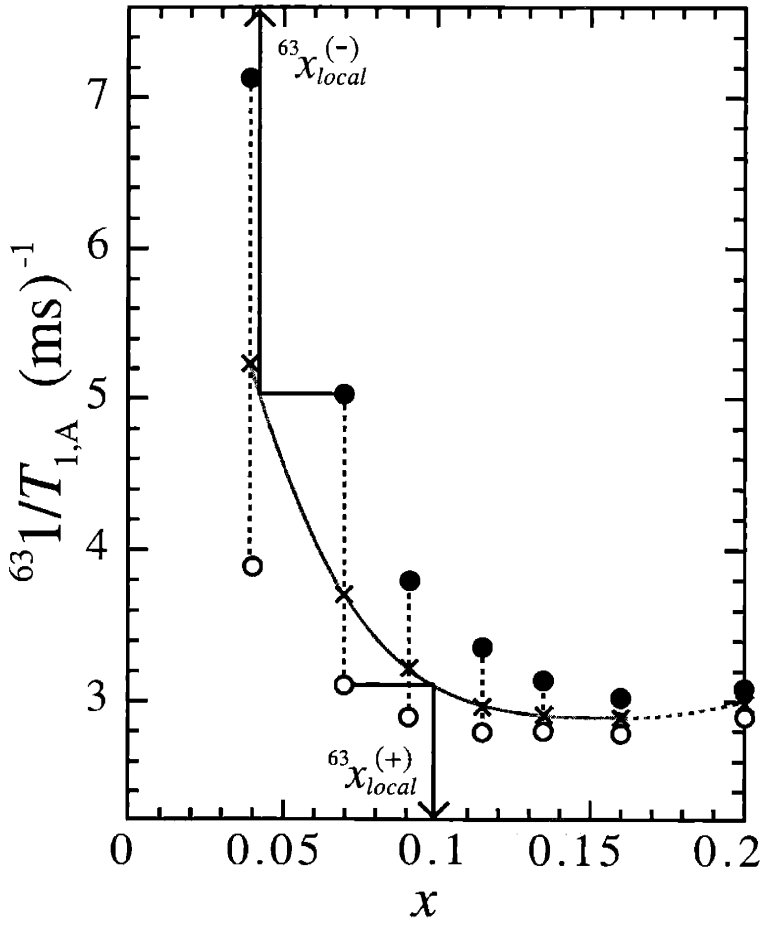

Figure 3-6: x dependence of $^{63}1/T_{1,A}^{(-)}$ (•), $^{63}1/T_{1,A}^{(0)}$ (×), and $^{63}1/T_{1,A}^{(+)}$ (○) at 295 K where the vertical dashed lines connect the data for each x. Gray solid curve shows interpolation of $^{63}1/T_{1,A}^{(0)}$ for all x, while dashed gray line shows overdoped regime. The solid black horizontal and vertical lines illustrate how to extract $^{63}x_{local}$ in the case of $x = 0.07$ according to $^{63}1/T_{1,A}^{(+)}$ at the upper frequency side of the ^{63}Cu NQR spectrum defined as $^{63}x_{local}^{(+)}$, and according to $^{63}1/T_{1,A}^{(-)}$ at the lower frequency side defined as $^{63}x_{local}^{(-)}$.

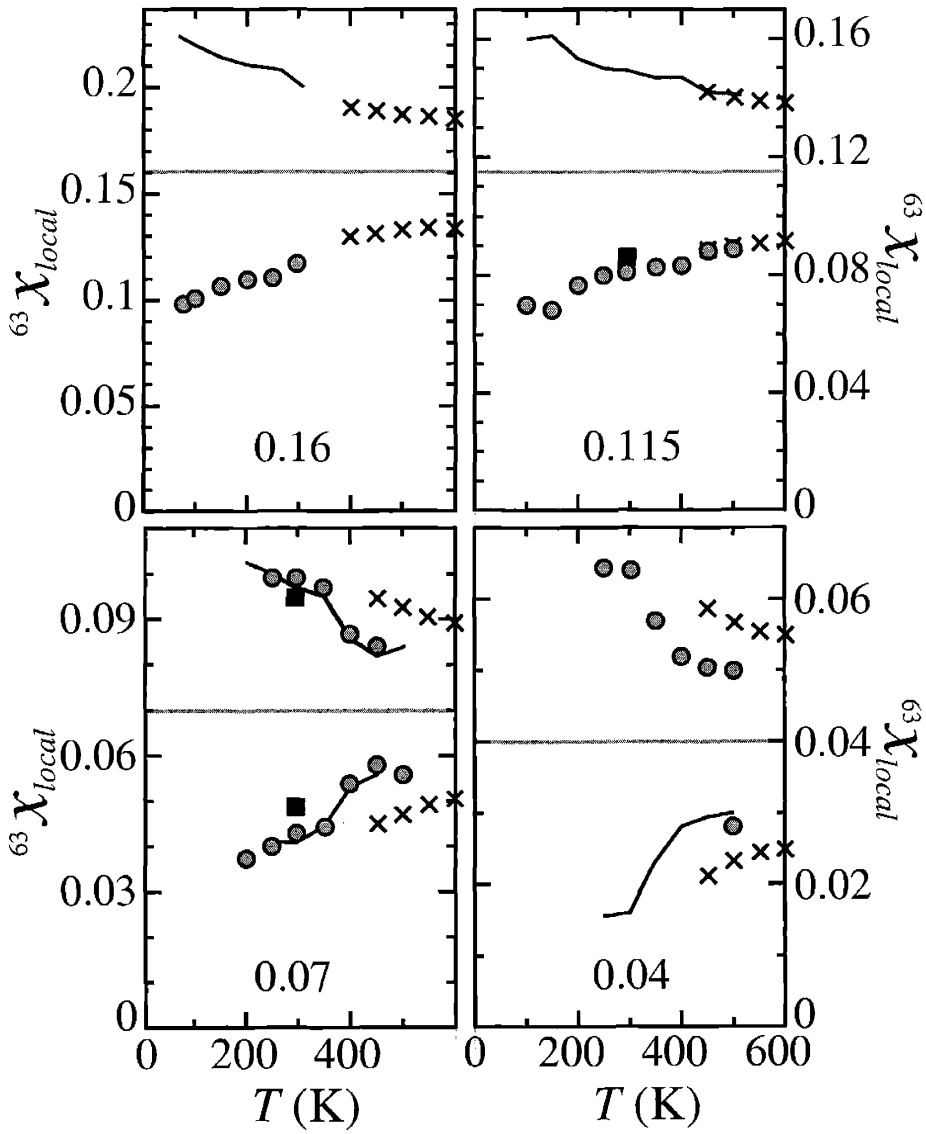

Figure 3-7: Temperature dependence of the local hole concentration ${}^{63}x_{local}$ (gray filled •) deduced from the upper frequency side of the A-line using ${}^{63}1/T_{1,A}^{(+)}$ (${}^{63}x_{local}^{(+)} > x$), and also from the lower frequency side using ${}^{63}1/T_{1,A}^{(-)}$ (${}^{63}x_{local}^{(-)} < x$), where x is indicated in each section and shown as the gray horizontal lines. Solid black lines show reflections of (gray filled •) data through x lines. Also shown is ${}^{63}x_{local}$ deduced using ${}^{63}1/T_{1,B}^{(+)}$ and ${}^{63}1/T_{1,B}^{(-)}$ at the B-line (■), together with the upper boundary ${}^{63}x_{patch}$ (×) deduced from calculated fit to the ^{63}Cu NQR spectrum using a patch-by-patch model for the spatial variation ${}^{63}x_{local}$.

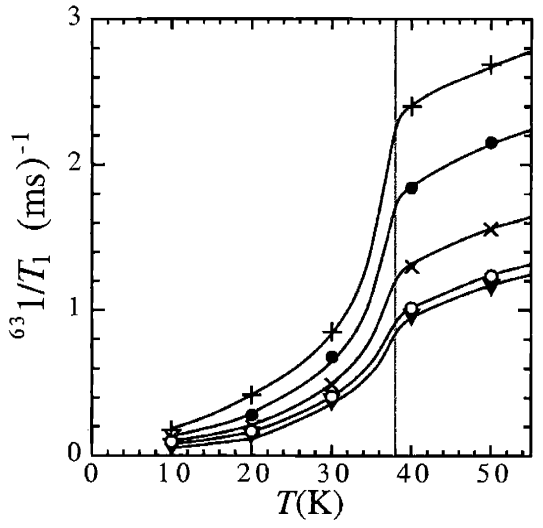

Figure 3-8: Temperature dependence of $^{63}1/T_1$ for $x = 0.16$ across superconducting boundary at $T_c = 38$ K (shown as grey verticle line) at various positions across the ^{63}Cu NQR line including $^{63}1/T_{1,A}^{(-1/10)}$ (+), $^{63}1/T_{1,A}^{(-)}$ (•), $^{63}1/T_{1,A}^{(0)}$ (×), $^{63}1/T_{1,A}^{(+)}$ (○), and $^{63}1/T_{1,B}^{(0)}$ (▼). Black curves are a guide for the eye.

Cu signal intensity is observable. As for the limitations of $^{63}x_{local}^{(+)}$, we note that at 295 K, $^{63}1/T_{1,A}^{(0)}$ tends to merge to the same value of ~ 3 ms^{-1} for $x \geq 0.09$ [36]. This implies that one needs to measure $^{63}1/T_1^{(+)}$ beyond the experimental uncertainties in order to get a reliable estimate of $^{63}x_{local}^{(+)}$.

The whole procedure is repeated at different temperatures, the final results of which are summarized in Fig. 3-7. At different temperatures we find similar experimental limitations in determining $^{63}x_{local}^{(+)}$ and $^{63}x_{local}^{(-)}$, however, in cases such as $x = 0.07$ where both can be determined, we consistently find that $^{63}x_{local}^{(+)} \simeq^{63} x_{local}^{(-)}$. In the overdoped region $x \geq 0.20$ we find a comparable frequency dependence of $^{63}1/T_1$ across the NQR line to that of $x = 0.16$. However, as shown in Fig. 3-5, we also find that $^{63}1/T_{1,A}^{(0)}$ starts to *increase* with increasing x for $x \geq 0.20$, and the same is true at all temperatures. We therefore separate the $^{63}1/T_{1,A}^{(0)}$ data for $x \geq 0.20$ shown as the dashed gray line in Fig. 3-5.

Our rough upper bound estimate discussed at the beginning of this chapter from

Fig. 3-1(b) showed that the upper frequency side of the ^{63}Cu NQR spectrum for $x = 0.07$ coincided with the CG of $x = 0.115$, i.e. $^{63}x_{local}^{(+)} \simeq 0.115$ for $x = 0.07$ at 295 K. Our estimate of $^{63}x_{local}$ in Fig. 3-6 based on $^{63}1/T_{1,A}$ and $^{63}1/T_{1,B}$ now reveals that $^{63}x_{local}^{(+)} \simeq 0.10$. We will present a more sophisticated upper boundary to $^{63}x_{local}$ based on the overlap of the ^{63}Cu NQR spectrum in chapter 4 where we take into account the intrinsic lattice broadening and deduce $^{63}x_{patch}$ based on a patch-by-patch model. For comparison, the calculated upper boundary $^{63}x_{patch}$ we shall deduce in chapter 4 is also shown in Fig. 3-7.

In Fig. 3-8 we show the temperature dependence of $^{63}1/T_1$ for $x = 0.16$ across the superconducting boundary $T_c = 38$ K (see Fig. 2-2) at various positions across the NQR spectrum. Despite the fact that the spatial variation $^{63}x_{local}$ varies as much as $0.10 \leq^{63} x_{local} \leq 0.22$ at ~ 100 K, all values of $^{63}1/T_1$ show a comparable fractional decrease below T_c where the superconducting gap opens. In the case of $^{63}1/T_1^{(-)}$ where $^{63}x_{local} = 0.10$, T_c should be around 25 K, however, there is already a large drop in $^{63}1/T_1^{(-)}$ by 30 K. In the case of $^{63}1/T_1^{(-1/10)}$ where $^{63}x_{local} = 0.08$, T_c should be as low as 20 K, however $^{63}1/T_1^{(-1/10)}$ clearly shows a drop below 30 K. This shows that the superconducting transition is a genuine bulk phenomenon which effects all patches regardless of the local hole concentration $^{63}x_{local}$. We note that $T_{NQR} > T_c$ for $x \leq 0.115$, therefore the ^{63}Cu wipeout for $T < T_{NQR}$ complicates our interpretation of $^{63}1/T_1$ near T_c in the case of $x \leq 0.115$. This is not the case for $x = 0.16$ shown in Fig. 3-8. Note also that all $^{63}1/T_1$ data presented in this thesis are within the temperature region $T_{NQR} \lesssim T \leq 600$ K.

3.3 $^{63}\nu_Q$ results

In Fig. 3-9(a) and (b) we show the temperature dependence of the resonance frequency at the CG of the NQR spectrum defined as $\langle ^{63}\nu_Q^k \rangle$ where $k = (A, B)$ for the A and B-lines, respectively. We determine the CG position of the NQR spectrum as

such

$$\begin{aligned} \left\langle {}^{63}\nu_Q^k \right\rangle &= \frac{\sum_j^{63} \nu_{j,Q}^k}{\sum_j} \\ {}^{63}\Delta\nu_Q^k &= \sqrt{\alpha_0} \cdot \sqrt{\frac{\sum_j \left({}^{63}\nu_{j,Q}^k - \left\langle {}^{63}\nu_Q^k \right\rangle \right)^2}{\sum_j}} \end{aligned} \tag{3.2}$$

where ${}^{63}\nu_{j,Q}^k$ corresponds to the jth data point of the observed NQR spectrum and $\alpha_0 = Ln(4)$. For a Gaussian distribution, as experimentally found to be the case for $x \geq 0.07$, the use of the prefactor α_0 then reduces ${}^{63}\Delta\nu_Q^k$ to the *HWHM* (half width at half maximum) exactly.

We see two temperature regimes for $\left\langle {}^{63}\nu_Q^k \right\rangle$ illustrated as the black lines and the gray lines which we define as the temperature regions above and below T_Q. Above T_Q we see a linear decrease of $\left\langle {}^{63}\nu_Q^A \right\rangle$ with decreasing temperature and a nearly constant value of $\left\langle {}^{63}\nu_Q^B \right\rangle$. In chapter 4 we attribute the temperature dependence above T_Q to thermal contraction of the lattice constants within the tetragonal phase, and in appendix A we also use this region to determine the necessary NQR parameters for the patch-by-patch model calculation. The second feature, below T_Q, is the change in curvature in $\left\langle {}^{63}\nu_Q^k \right\rangle$ for both A and B-lines shown as the solid gray curved region. The increase in this region is due to the local orthorhombic distortions [36] which in the case of $x \geq 0.04$ set in above the orthorhombic structural phase transition temperature $T_{st}(\leq 515$ K) according to LRO [100]. In the case of $x = 0.20$, we see evidence for local orthorhombic distortion starting as high as $T_Q = 400$ K where neutron results show no sign of LRO. In the chapter IV we use the data below T_Q to calculate the degree of local tilting of the CuO_6 octahedra away from the c-axis, defined as θ_{local}, and we see that there is a sharp onset in θ_{local} only the case of $x = 0.0$. For $x > 0.0$ we see a somewhat rounded transition into the local orthorhombic phase. We note that these local precursive effects to the LRO are consistent with PDF (pair distribution function) analysis of neutron powder diffraction data [12] and XAFS (X-ray Absorption Fine Structure) analysis [28] which also see evidence for local lattice distortions in the temperature region above T_{st} and into the overdoped regime

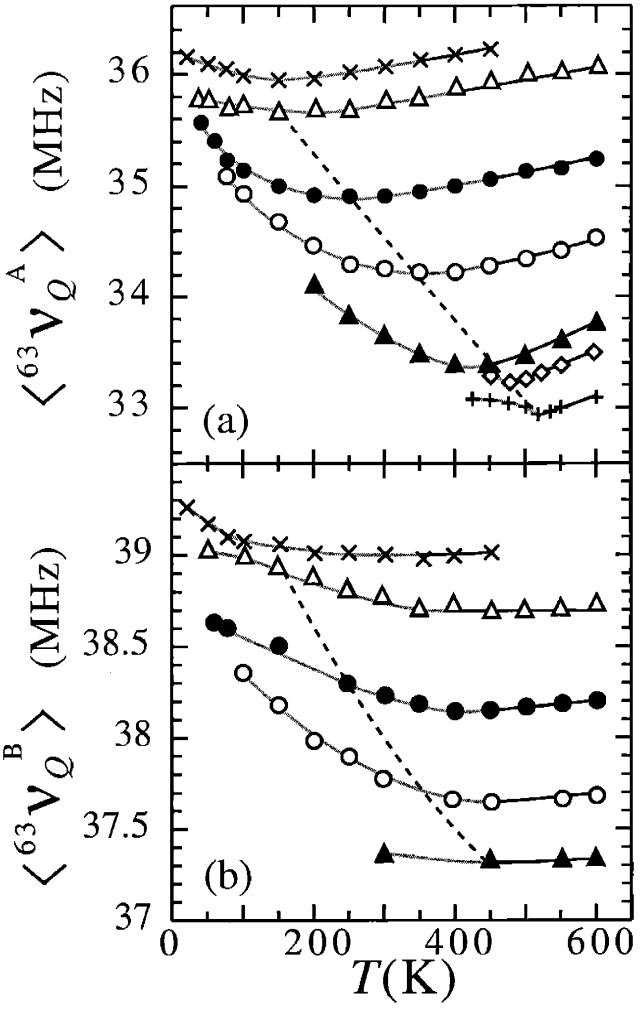

Figure 3-9: Temperature dependence of CG of the ^{63}Cu NQR spectrum (a) $\langle {}^{63}\nu_Q^A \rangle$ at the A-line, and (b) $\langle {}^{63}\nu_Q^B \rangle$ at the B-line for $x = 0.20$ ($\times$), $x = 0.16$ ($\triangle$), $x = 0.115$ ($\bullet$), $x = 0.07$ ($\circ$), $x = 0.04$ ($\blacktriangle$), $x = 0.02$ ($\diamond$), $x = 0.0$ (+). Black curves show fit to temperature region above T_Q where ${}^{63}x_{patch}$ is deduced, while gray curves show fit to data below T_Q where local orthorhombic distortions are deduced. Dashed black line shows onset of orthorhombic phase according to LRO [100].

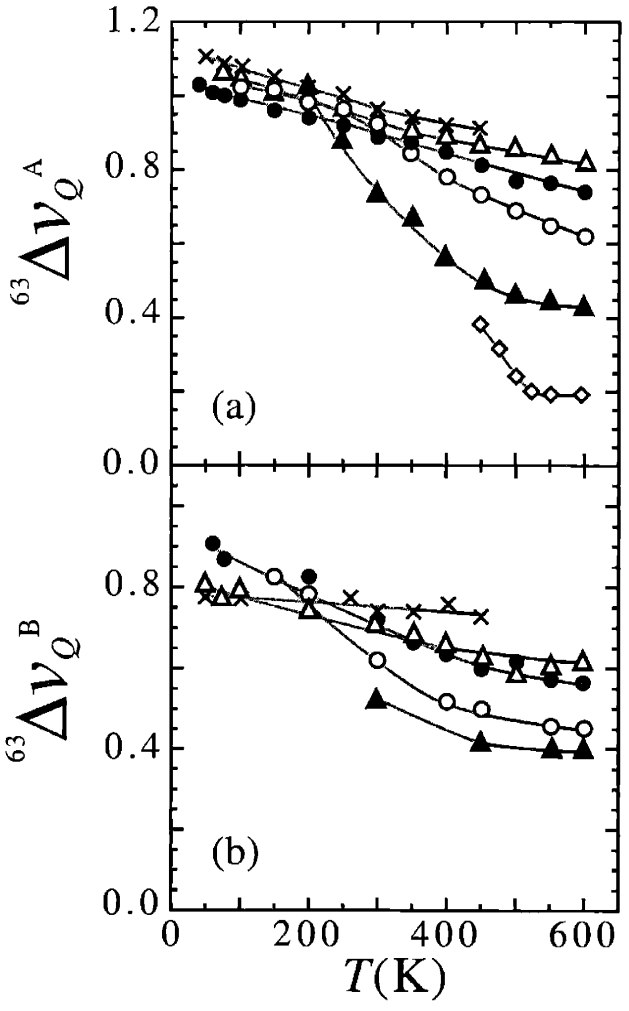

Figure 3-10: Temperature dependence of *HWHM* (half width at half maximum) of the ^{63}Cu NQR spectrum (a) $^{63}\Delta\nu_Q^A$ at the A-line, and (b) $^{63}\Delta\nu_Q^B$ at the B-line for $x = 0.20$ ($\times$), $x = 0.16$ ($\triangle$), $x = 0.115$ ($\bullet$), $x = 0.07$ ($\circ$), $x = 0.04$ ($\blacktriangle$), $x = 0.02$ ($\diamond$). Black and gray curves indicate temperature region above and below T_Q respectively.

$x \gtrsim 0.20$.

The temperature dependence of the observed $HWHM$ ${}^{63}\Delta\nu_Q^k$ of the NQR spectra, defined using Eq. (3.2), is presented in Fig. 3-10. We also reproduce the temperature regions above and below T_Q, taken from Fig. 3-9, as the black and gray curves respectively. In chapter 4 we use the ${}^{63}\Delta\nu_Q^k$ data for $T > T_Q$ to deduce a lower bound for the patch radius ${}^{63}R_{patch}$, and the corresponding an upper bound ${}^{63}\Delta x_{patch} (\propto 1/{}^{63}R_{patch})$.

Chapter 4

Patch-by-Patch model of ^{63}Cu NQR data

The goal of this chapter is to create the static real-space model of the spatial variation in local hole concentration $^{63}x_{local}$. We shall use a point charge lattice summation incorporating randomness effects to calculate the inhomogeneous *distribution* in the EFG (electric field gradient) which constitutes the observed ^{63}Cu NQR spectrum. To the best of our knowledge, such calculations incorporating randomness effects into the EFG calculation have not been reported. We shall deduce all parameters necessary for this task in a self-consistent way by using our pool of NQR data, and we shall successfully account for the entire ^{63}Cu NQR spectrum, including the B-line, with one adjustable parameter $^{63}R_{patch}$ which defines the length scale of the spatial variation in hole concentration x_{local}. Once $^{63}R_{patch}$ is optimized to fit the ^{63}Cu NQR spectrum, we deduce an upper boundary $^{63}x_{patch}$ for the spatial variation defined as

$$^{63}x_{patch} = x \pm ^{63}\Delta x_{patch} \tag{4.1}$$

, where $^{63}\Delta x_{patch}(\propto 1/^{63}R_{patch})$ is the calculated upper bound to the extent of the spatial variation. As shown in Fig. 3-7, $^{63}x_{patch}$ is found to be consistent with $^{63}x_{local}$, where $^{63}x_{local}$ is determined in a model independent way.

As we shall show, the distribution in the EFG is determined by (a) the random

substitution of donor ions, (b) the variation in local hole concentration ${}^{63}x_{local}$ over short length scales ${}^{63}R_{patch} = 3.0 - 4.0$ nm, and (c) the distribution in local lattice distortions. Without *a priori* knowing the lattice distortions in (c), we attribute the whole NQR linebroadening to mechanisms (a) and (b). This implies that the deduced ${}^{63}R_{patch}$ we present is a lower bound and correspondingly ${}^{63}x_{patch}$ is an upper boundary. However we shall demonstrate that ${}^{63}x_{patch} \sim^{63} x_{local}$, where ${}^{63}x_{local}$ is model independent, which implies that using mechanisms (a) and (b) alone is justified in the temperature range $T > T_Q$. Below T_Q where local orthorhombic distortions set in (Fig. 3-9), we terminate our analysis of ${}^{63}x_{patch}$. The reason for this is that we also see an increase in the NQR linewidth (Fig. 3-10) below T_Q in the case of $x \leq 0.07$, which suggests that ignoring mechanism (c) above is no longer justified for $T < T_Q$. In chapter 4.-F we make predictions about the magnitude of mechanism (c) by attributing the extra linebraodening for $T < T_Q$ to distributions in the lattice distortions. We note, however, that with the exception of chapter 4.4, we ignore mechanism (c) in our analysis.

There are two approaches for computing the EFG. The first is an *ab initio* approach [33, 52, 71] which involves quantum chemistry calculations, and the second approach makes use of the experimental data [69, 76, 79, 90, 98] to deduce all the necessary parameters in an empirical way. The *ab initio* approach has been extensively used to calculate the EFG at the ^{63}Cu site in La_2CuO_4 [33, 52, 71], and gives a consistent value for the observed resonance frequency $\nu_{NQR} = 33$ MHz [36] to within uncertainties in the quadrupole moment ${}^{63}Q$. The basic idea behind this approach is that since the EFG decreases rapidly as $1/r^3$ away from origin of the calculation, the most significant contributions should be from local EFG components. One can justifiably separate a cluster of ions in the immediate vicinity of the Cu nucleus whose contributions are calculated using a full spin-polarized DF (density functional) or HF (Hatree-Fock) calculation, while the rest of the ions in the crystal are treated as point charges. The smallest realistic cluster is typically CuO_6/Cu_4La_{10}, where the central $(CuO_6)^{-10}$ ionic cluster consists of 23 molecular orbitals for each spin projection made up of linear combinations of 5 $3d$ and 18 $2p$ atomic orbitals. Such calculations are

found to depend on the cluster size used, where the larger clusters are more reliable yet involve increasingly complex calculations. They also depend on whether one uses DF or HF, however both successfully predict that the molecular orbital with the highest energy is the antibonding hybridization between the Cu $3d_{x^2-y^2}$ orbital and the O $2p_x$ and $2p_y$ orbitals. The DF method, however, predicts [33] a predomnantly covalent bonding picture where the localized atomic spin density on the Cu is $\rho_{Cu} = 0.67$, while HF predicts more of an ionic bonding picture where $\rho_{Cu} = 0.90$.

Before discussing our new approach for calculating the inhomogeneous distribution of the EFG, let us clarify exactly what inhomogeneous broadening implies in the context of ^{63}Cu NQR. The linebroadening of the ^{63}Cu NQR spectrum for $x > 0.02$ is dominated by the *inhomogeneous* distribution in the EFG. The inhomogeneous broadening may be pictured as such: say there is a Cu nucleus j lying in a particular EFG with value V_j which resonates at frequency ν_j, while a distant nucleus k sits in a distinct EFG environment V_k and resonates at ν_k. As is predominantly the case across the sample, the separation between the two nuclei $\mathbf{r}_{(j,k)}$ is *larger* than the range $\xi_{AF} \sim 3\ a$ of the indirect nuclear spin-spin coupling [70] where ξ_{AF} is the correlation length of the anti-ferromagnetic fluctuations. In such cases, one may flip the j nucleus using an r.f. pulse and observe its echo *without* being effected by the influence of the r.f. pulse on the k nucleus. One then measures the ^{63}Cu NQR spectrum by resonating at ν_j and effectively counting the number of nuclei N_j in the sample with EFG values V_j, then changing the resonance frequency to ν_k and counting the number of nuclei N_k, thereby building up the *inhomogeneous* NQR spectrum.

As one approaches the undoped limit $x < 0.02$, the random effects become less and less significant, and the linebroadening becomes predominantly *homogeneous* in nature and dominated by the indirect nuclear spin-spin coupling. As we show in appendix B, in the case of pure homogeneous broadening for $x = 0.0$, there is no distribution in $^{63}1/T_1$ across the NQR spectrum, even in the orthorhombic phase $T < T_{st}$. We note that the two *distinct* length scales ξ_{AF} and $^{63}R_{patch}$ which determine the linebroadening of the homogeneous and inhomogeneous NQR spectra, respectively, have qualitatively different temperature dependences. As we shall show,

$^{63}R_{patch}$ decreases with decreasing temperature, while ξ_{AF} increases with decreasing temperature [100]. Furthermore $^{63}R_{patch} \gg \xi_{AF}$ within the x and temperature range of interest.

4.1 The EFG Calculation

In the experimental approach, the EFG tensor $V^{(\beta,\gamma),k}$ (see Eq. (2.11)) along the orthognal spatial directions (β,γ) for the Cu site $k = (A,B)$ is segregated into an onsite $3d$ contribution $V_{3d}^{(\beta,\gamma)}$ and an offsite lattice contribution $V_{latt}^{(\beta,\gamma),k}$ as such:

$$V^{(\beta,\gamma),k} = \zeta_{3d}^{k} V_{3d}^{(\beta,\gamma)} + \zeta_{latt}^{k} V_{latt}^{(\beta,\gamma),k} \tag{4.2}$$

where we introduce the isotropic anti-shielding factor [81] ζ_{3d}^{k} originating from the local $3d$ electrons and the isotropic anit-shielding factor ζ_{latt}^{k} orginating from the lattice. We also leave the possibilty open that they depend on which Cu site $k = (A,B)$ is being calculated. In appendix A we deduce that $\zeta_{3d}^{A} \simeq 0.9$, $\zeta_{latt}^{A} \simeq 23$, $\zeta_{3d}^{B} \simeq 0.82$, and $\zeta_{latt}^{A} \simeq 18.6$, all in a self consistent way using our pool of NQR data. We shall also show that the onsite EFG contribution $V_{3d}^{(\beta,\gamma)}$ is overall negative while the lattice contribution $V_{latt}^{(\beta,\gamma),k}$ is overall positive.

The anti-shielding factors must be determined experimentally, while in the *ab initio* approach they are, in a sense, already accounted for. The anti-shielding factors are found *not* to vary significantly between different classes of high T_c cuprates [76]. Likewise, the anti-shielding factors deduced in a similar way for the planar oxygen site [80, 90, 98] is also found to be consistent between different classes of cuprates, which supports the use of the experimental approach.

In accord with A. Abragam, B. Bleaney and co-workers [2,10], the principle value of the onsite contribution $V_{3d}^{(c,c)}$ arising from $3d_{x^2-y^2}$ hole is taken to be

$$V_{3d}^{(c,c)} = -\frac{4}{7} e \left(1 - 4 f_{\sigma}^{o}\right) \left\langle r_{3d}^{-3} \right\rangle \tag{4.3}$$

where we have allowed for covalency in the form of f_{σ}^{o} which represents the fractional

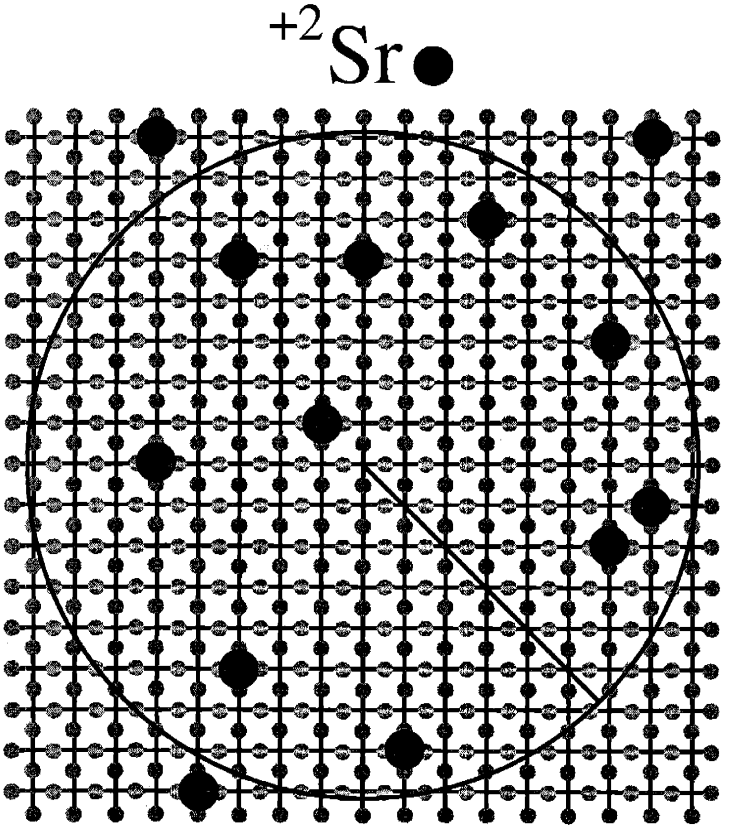

Figure 4-1: Illustration of a CuO_2 plane where the $^{+2}$Sr ions are randomly placed in the lattice. The corners of each square represent a Cu site. The $^{+2}$Sr donor ions (•) immdediatley above or below the Cu sites in the plane are shown. Planar oxygen sites are shown as (gray •). Also shown is a typical patch (circle) with a patch radius $^{63}R_{patch} = 3.0$ nm (=8 a) shown as the black line. For this particular random configuration κ, the local hole concentration is $^{63}x^{\kappa}_{local} = 0.05$.

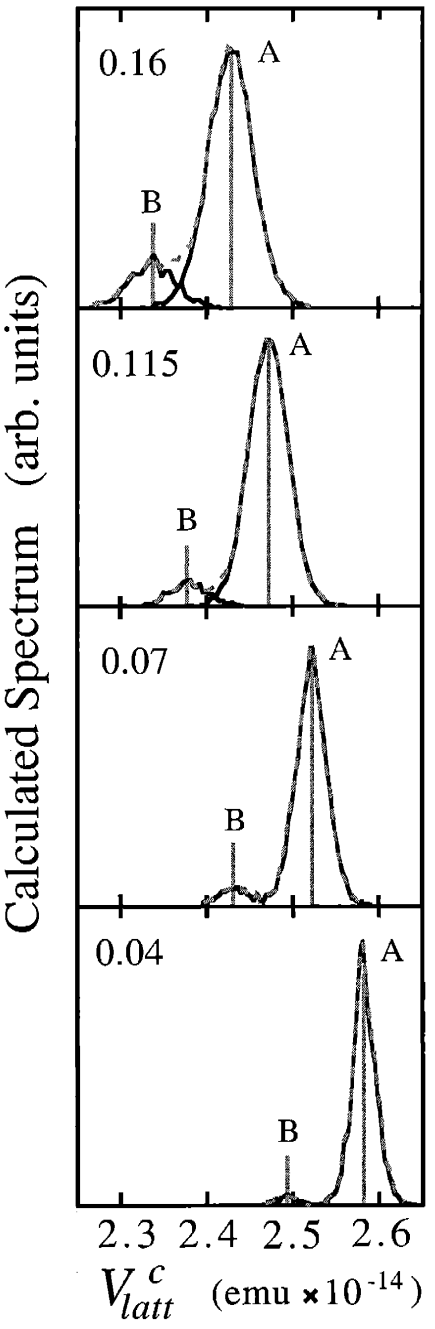

Figure 4-2: Results of the EFG calculation incorporating the random positioning of $^{+2}$Sr ions in the lattice. Data shows the spectrum of the principle values V_{latt}^{c} of the EFG in [emu $\times 10^{-14}$] at 600 K for various x shown in each part. Gray vertical dashed lines indicate CG position $\left\langle V_{latt}^{c,k} \right\rangle$ for $k = (A, B)$ used to calculate anit-shielding factors.

spin denisty on the four neighbouring planar oxygen $2p_\sigma$ orbitals. In order to be consistent with our results of ^{17}O hyperfine coupling analysis we use $f_\sigma^o = 0.076$ [80] which favours the covalent bonding model. Using the ionic model with $f_\sigma^o = 0$ results in an overall $\sim$ 14 % increase in $^{63}R_{patch}$ and corresponding $\sim$ 12 % decrease in our theoretical estimate $^{63}\Delta x_{patch}$ over the covalent model. We note that $f_\sigma^o = 0.076$ deduced from the oxygen hyperfine couplings [80, 98] is consistent with Cu hyperfine coupling analysis using NMR [91] where $f_{Cu} = (1 - 4f_\sigma^o) = 0.7$ was observed. It is also generally accepted that the *ab initio* DF calculation which favors stronger covalency is a more realistic approach than the HF approach.

The lattice contribution $V_{latt}^{(\beta,\gamma)}$ to the total EFG is simulated using a point charge lattice summation with fractional point charges. We use the standard expression for the summation

$$V_{latt}^{(\beta,\gamma)} = \sum_j q_j \left(3x_{\beta,j}x_{\gamma,j} - r_j^2\delta_{\beta,\gamma}\right)/r_j^5 \tag{4.4}$$

where the sum over j refers to the sum over the surrounding point charges q_j in the lattice a distance r_j away. The charges q_j are assigned as follows

$$\begin{aligned} q_{Cu} &= +(2 - 4f_\sigma^o)\,e \\ q_{O_{pl}} &= -(2 - 2f_\sigma^o - x/2)\,e \\ q_{O_{ap}} &= -2e \\ q_{La} &= +3e \\ q_{Sr} &= +2e \end{aligned} \tag{4.5}$$

where x is the nominal hole concentration, O_{pl} stands for the planar oxygen site, O_{ap} stands for the apical oxygen site and $e > 0$ is the electronic charge in emu units. Note that we make use of the full difference in valency between the $^{+3}$La and $^{+2}$Sr ions. This implies that depending on the the geometrical distribution of the $^{+2}$Sr ions in the lattice, $V_{latt}^{(\beta,\gamma)}$ takes on different values. In Fig. 4-1 we illustrate the random positioning of the $^{+2}$Sr ions surrounding the central Cu site from which the EFG is calculated.

The standard approach in all earlier works, except for [79], has been to set $q_{La} = q_{Sr} = -(3 - x/2)$ which effectively bypasses any randomness effects and results in delta function spectra of the EFG. For this section of the calculation we effectively take ${}^{63}R_{patch} = \infty$ and uniformily place the donated holes x from the ${}^{+2}$Sr ions with full mobility onto the planar O sites, which correspondingly reduces $|q_{O_{pl}}|$ in Eq. (4.5), bearing in mind that there are two planar oxygens per unit cell. Placing the donated holes onto the planar oxygen sites as such is consistent with high energy spectroscopy studies [21].

The positions $\mathbf{r}_j(x,T)$ of the ions (as a function of x and T) were taken from a systematic X-ray powder diffraction study by P.G. Radaelli *et al.* [72]. $\mathbf{r}_j(x,T)$ were defined with respect to an orthorhombic unit cell which consisted of $4\times(La_{2-x}Sr_xCuO_4)$ primitive cells, each with the K_2NiF_4 structure [24]. The absolute values of the lattice constants $[a_o, b_o, c]$ were calibrated at 295 K using our data from Fig. 2-3. The EFG calculation is naturally sensitive to inputs $\mathbf{r}_j(x,T)$, therefore we used smooth interpolation of the values $\mathbf{r}_j(x,T)$ for different x in order to avoid unnessecary scattering in the output $V_{latt}^{(\beta,\gamma)}$. We used the same thermal expansion coefficients [14, 72] $\alpha_a = +1.45\cdot 10^{-5}K^{-1}$ and $\alpha_c = +1.42\cdot 10^{-5}K^{-1}$ for all x, consistent with corresponding thermal coefficients found in $La_{2-x}Ba_xCuO_4$ [86].

The lattice summation was carried out to a radius of 50 Å away from the Cu atom at the origin $[0,0,0]$. The proceedure for the random placement of the ${}^{+2}$Sr ions is carried out as follows: a different random number λ with a flat probability distribution $0 < \lambda < 1$ is generated at each La site. If $\lambda > x/2$ at a particular La site, a La ion with charge $+3e$ is assigned to that site, while if $\lambda < x/2$, a Sr ion with charge $+2e$ is assigned. In equation form this gives the perscription

$$\begin{aligned} \lambda > x/2 \quad (\rightarrow) \quad +3e \\ \lambda < x/2 \quad (\rightarrow) \quad +2e \end{aligned} \tag{4.6}$$

at each La site where $0 < \lambda < 1$. The factor $1/2$ in the probability condition arises because there are 2 La sites per formula unit. Once this is carried out at each La site,

we have achieved the particular random configuration κ of $^{+2}$Sr ions in the lattice, an illustration of which is given in Fig. 4-1. In our formulation, we exclude the possibility of any $^{+2}$Sr - $^{+2}$Sr clustering beyond probablilty theory, which is supported by the absence of any significant diffuse scattering in neutron diffraction experiments [13].

Once the random configuration κ is determined, the summation in Eq. (4.4) is carried out and ${}^{\kappa}V_{latt}^{(\beta,\gamma)}$ is diagonalised and the principle value is stored into a vector P_{latt}. The calculation is computed in the tetragonal phase where the principle value of ${}^{\kappa}V_{latt}^{(\beta,\gamma)}$ is found to lie along the c-axis, i.e. ${}^{\kappa}V_{latt}^{(\beta,\gamma)}$ reduces to ${}^{\kappa}V_{latt}^{c}$. Next, the whole lattice is re-randomized and a new random configuartion κ' of $^{+2}$Sr ions is determined, the lattice summation in Eq. (4.3) is computed and the new value of ${}^{\kappa'}V_{latt}^{c}$ is stored into P_{latt}. This proceedure is re-iterated $\sim 10^4$ times until the dimension of P_{latt} is sufficiently large to create a histogram spectrum of P_{latt} with $\sim$ 50 bins across the lineshape, the results of which we show for a selection of x at 600 K in Fig. 4-2 shown by the solid gray lines. Note that we always calculate the EFG for the Cu site at the origin using a different random configuration of $^{+2}$Sr ions for each run. An equivalent approach is to stick to one random configuration κ for each sample and calculate the EFG at each Cu site in the lattice thereby building up P_{latt}, however, this latter approach is computationally more intense. Since we are dealing with a purely random system, both methods are equivalent, therefore we use the former method.

We notice three immediate features about the results. The first is the overall decrease in CG (center of gravity) $\langle V_{latt}^{c} \rangle$ with increasing x. This is a consequence of the change in lattice paramters and the decrease in $|q_{O_{pl}}|$ with increasing x. The second feature is the change in *HWHM* defined as ΔV_{latt}^{c} which is computed in an analogous manner using Eq. (3.2). ΔV_{latt}^{c} is shown to increase with increasing x which is a consequence of the increased amount of quenched disorder in the lattice due to the increased randomness from the $^{+2}$Sr ions. The third feature in our lattice summation is the presence of the secondary peak known as the B-line.

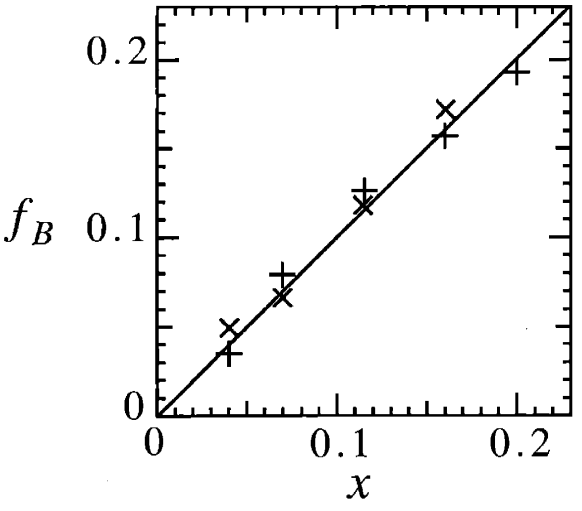

Figure 4-3: x dependence of the fractional B-line intensity f_B defined as $f_B = \frac{I_B}{I_A+I_B}$, where I_A and I_B have been corrected for differences between the spin-spin relaxation rates at the A and B-sites, respectively, at 300 K (+) and 600 K ($\times$). Solid line shows prediction by model $f_B = x$ where the site assigment for the B-site is specifically shown in Fig. 4-4.

4.2 The B-line

The ^{63}Cu NQR spectrum is known to show a secondary peak known as the B-line [101]. One can gain insight into the origin of the B-line by comparing the observed relative intensity of the B-line I_B to the total intensity $I_A + I_B$ defined as f_B^{exp} where

$$f_B^{exp} = \frac{I_B}{I_A + I_B} \tag{4.7}$$

In Fig. 4-3 we show f_B^{exp} as a function of x after correcting both I_A and I_B for differences in the spin-spin relaxation rates. The spin-spin relaxation rate is found to be uniformily $\sim$ 15 % lower for the B-line compared to the A-line, similar to the differences between $^{63}1/T_1$. Our data in Fig. 4-3 at both 300 K and 600 K clearly show that $f_B^{exp} \simeq x$ over a large range $0.04 \leq x \leq 0.20$. In this section we present various evidences that the B-line is primarily *structural* in origin [71, 79]. In particular, the Cu B-sites correspond to Cu nuclei located at $\mathbf{r} = [n_a a, n_b b, n_c c]$ (where $[n_a, n_b, n_c]$ are $\pm$ integers ranging from zero to ∞) with distinct EFG values due to the presence of $^{+2}$Sr ions located at positions $\mathbf{r} = [n_a a, n_b b, (n_c \pm 0.361)c]$. We illustrate the Cu B-site assignment in the orthorhombic unit cell [24] shown in Fig. 4-4. The relative intensity of such Cu sites f_B is then given by the concentration of $^{+2}$Sr ions x, i.e. $f_B = x$. This site assignment for the B-site Cu nuclei naturally accounts for the observed relative intensity $f_B^{exp} \simeq x$ shown in Fig. 4-3.

Generally, the origin of the B-line has been attributed to such structural effects from the dopant ions [82, 101], but the limited range of x investigated in earlier studies did not allow unambiguous identification of the origin of the B-line. In fact, there has been a persistent claim that the origin of the B-line is more exotic in nature [26, 52, 83] and originates from an intrinsic response of the material to the presence of doped holes. Such a conjecture that the B-line is an electronic rather than a structural effect was based on the observed similarity between the A-B line splitting $\sim$ 3 MHz for both $La_{2-x}Sr_xCuO_4$ and $La_2CuO_{4+\delta}$ systems [26, 52, 83]. It was thought that the similar value of the A-B line splitting between such distinct systems was clear evidence that the second site was a result of the presence of the

doped holes themselves independent of the means of doping. If this is the case, however, then it should equally well be observed in other 214 compounds such as $La_{2-x}Ba_xCuO_4$. However, a much larger A-B line splitting of $\sim$ 6 MHz [32, 101] is observed in $La_{2-x}Ba_xCuO_4$ where the $^{+2}$Ba ion is known to cause much larger ionic size effect disorder [12] than the $^{+2}$Sr ion, and which also stablizes an additional structural phase transition at low temperatures [86]. We also recall that the ^{63}Cu NQR spectrum in $La_{2-x-y}Eu_ySr_xCuO_4$ for ^{63}Cu isotope enriched samples [32] shows a third structural peak (the C-line) whose fractional intensity is observed to equal y. The C-line corresponds to a Cu nucleus directly above or below a $^{+3}$Eu ion.

Another piece of evidence that the B-line is primarily structural in origin is the similarity in the frequency dependence of $^{63}1/T_1$ to that of the A-line, as shown in Fig. 2-1 and Fig. 3-1. Furthermore, as shown in Fig. 3-7 a similar analysis of the extent of the frequency dependence across the B-line showed a consistent value of $^{63}x_{local}$ to that at the A-line. The similarity between the frequency dependence in $^{63}1/T_1$ indicates that the length scale of the spatial variation in $^{63}x_{local}$ is *larger* than the average $^{+2}$Sr - $^{+2}$Sr distance $l_{Sr} = a/\sqrt{x}$, or equivalently the average B-site to B-site distance. Later we explicitly show that the deduced length scale $^{63}R_{patch} \gtrsim 3$ nm is larger than l_{Sr} in the region of interest $x > 0.02$.

We also note that in Fig. 3-4 we showed that $^{63}T_{1,A}/^{63}T_{1,B}$ = 0.9-0.84, i.e. that $^{63}1/T_{1,B}$ is uniformily suppressed compared with $^{63}1/T_{1,A}$. Our systmetic study up to $x = 0.20$, also showed that in the overdoped region $x \geq 0.20$, $^{63}1/T_1$ increases with increasing x. This implies that if there is hole localisation in the vicinity of a Cu B-site as claimed in Ref. [26, 52, 83], then $^{63}1/T_{1,B}$ at the B-site should be *larger* than $^{63}1/T_{1,A}$ in the case of $x = 0.16$. Fig. 3-4 clearly shows that this is not the case, and further supports our interpretation that the B-line is primarily structural in origin. The most likely explanation for $^{63}T_{1,A}/^{63}T_{1,B} = 0.9 - 0.84$ is that the hyperfine couplings $|^{63}A(\mathbf{Q_{AF}})|$ is 5-10 % lower at the B-site due to the increased lattice distortions in the vicinity of a $^{+2}$Sr ion. It is known from XAFS [27] that the $^{+2}$Sr ion causes major structural distortions in its vicinity, which could well account for such changes in the hyperfine couplings.

We now proceed with our calculation and take the B-line to originate from structural effects illustrated in Fig. 4-4. We separate the A and B-sites within the calculation by separating any randomly generated ${}^{\kappa}V^{c}_{latt}$ value with a $^{+2}$Sr ion in a position illustrated in Fig. 4-4, and placing it into a new vector ${}^{B}P_{latt}$, while placing all other generated ${}^{\kappa}V^{c}_{latt}$ values into ${}^{A}P_{latt}$. In this way we can separate the A and B lines as shown by the solid black lines in Fig. 4-2, and separately determine the CG for both lines $\left\langle V^{c,A}_{latt} \right\rangle$ and $\left\langle V^{c,B}_{latt} \right\rangle$ (deduced in a similar fashion to Eq. (3.2)). The values for $\left\langle V^{c,k}_{latt} \right\rangle$ are illustrated as the dashed vertical lines in Fig. 4-2. In appendix A we outline how to determine the anti-shielding factors for both the A and B-lines separately using the calculated $\left\langle V^{c,k}_{latt} \right\rangle$ values and the experimentally observed resonance frequencies $\left\langle {}^{63}\nu^{k}_{Q} \right\rangle$ also at the CG, taken from Fig. 3-9.

Using the anti-shielding factors we can now compare the calculated intrinsic lattice width ΔV^{c}_{latt} (deduced in a similar fashion to Eq. (3.2)) from the lattice broadening alone, to the experimentally observed widths $\Delta\nu^{k}_{Q}$ shown in Fig. 3-10. Note that we do not attach a $k = (A, B)$ superscript to ΔV^{c}_{latt} since the calculation yields the *same* widths for both the A and B-lines. We then assume that the total width from the calculation $\Delta\nu^{k}_{latt}$ is proportional to the intrinsic lattice width as such

$$\Delta\nu^{k}_{latt} = \frac{e|{}^{63}Q|}{2h}\zeta^{k}_{latt}\Delta V^{c}_{latt} \tag{4.8}$$

with NO corresponding width from the onsite contribution, i.e. $\Delta V^{c,k}_{3d} = 0$. We justify this approach by the fact that the ratio of widths between the A and B-lines is experimentally found to be $\Delta\nu^{B}_{Q}/\Delta\nu^{A}_{Q} \simeq 0.63$ in the temperature region $T > T_{Q}$. According to appendix A, this ratio is closer to the ratio of the anti-shielding factors for the lattice $\zeta^{B}_{latt}/\zeta^{A}_{latt} = 0.67$ than for the onsite $\zeta^{B}_{3d}/\zeta^{A}_{3d} = 0.89$. The anit-shielding factors are deduced without any information about the widths, therefore we have self-consistently shown that the observed width $\Delta\nu^{k}_{Q}$ is dominated by the intrinsic lattice width ΔV^{c}_{latt}.

Using the anti-shielding factors we now convert the calculated EFG spectra shown in Fig. 4-2 to equivalent resonance frequencies, the result of which were expicilty

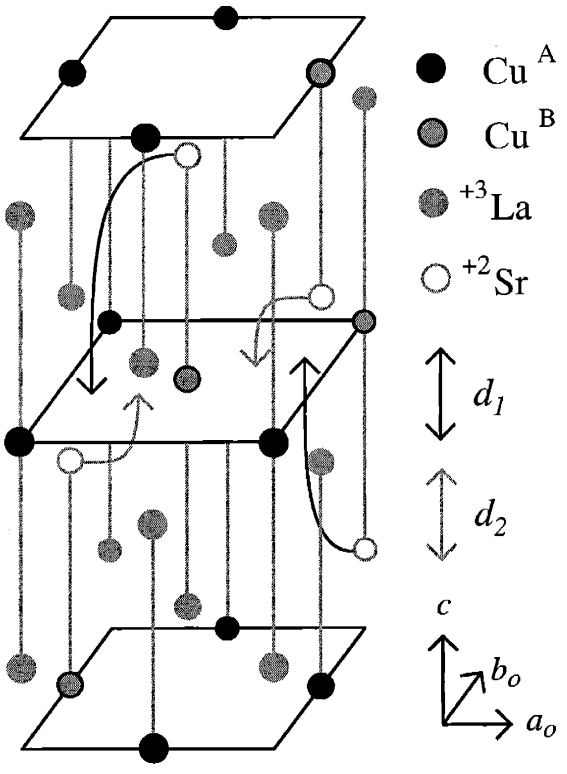

Figure 4-4: Pictorial representation of the A-site Cu nucleus (•) and B-site Cu nucleus (gray filled ○) determined according to adjacent positions of $^{+3}$La ion (gray •) and $^{+2}$Sr ion (gray ○), respectively. Also shown are methods of doping into central plane using d_1 $^{+2}$Sr sites (black curves) or d_2 $^{+2}$Sr sites (gray curves). Illustration is shown using an orthorhombic cell.

shown for $x = 0.115$ in Fig. 3-2 by the dashed line. Up to this point in the EFG calculation, we have effectively taken care of the random placement of $^{+2}$Sr ions in the lattice, however, we are still assuming that the holes are uniformily distributed across the plane, i.e. $^{63}R_{patch} = \infty$. Clearly this is not the whole picture since our calculation of $\Delta\nu^k_{latt}$ underestimates the observed width $\Delta\nu^k_Q$ by a factor ~ 2 as shown in Fig. 3-2 for $x = 0.115$, and the same is found for other samples.

4.3 Deducing $^{63}R_{patch}$

As outlined in the introduction of this section, there are two additional mechanisms besides $\Delta\nu^k_{latt}$ that can be used to account for the experimental data $^{63}\Delta\nu^k_Q$. The first additional broadening mechanism is the spatial variation in local hole concentration $^{63}x_{local}$ over which $^{63}1/T_1$ varies which we define as $\Delta\nu^k_{R_{patch}}$ and reduces to $\Delta\nu^k_{latt}$ in the limit $^{63}R_{patch} = \infty$. The second independent broadening mechanism is distributions in local orthorhombic distortions. In this section we attribute all the additional broadening to the variation in $^{63}x_{local}$, while in chapter 4.4 we discuss the effects of the lattice distortions.

The introduction of the spatial variation in local hole concentration $^{63}x_{local}$ into the EFG calculation is an extension of what we have described in arriving at the intrinsic width $\Delta\nu^k_{latt}$. We start by randomly positioning the $^{+2}$Sr donor ions into the $^{+3}$La sites as described earlier. Next, we ascribe a patch (i.e. a circle) of radius $^{63}R_{patch}$ around the central Cu site at the origin from which the EFG is calulated as shown in Fig. 4-1. We then determine the total number of Cu sites $N^{R_{patch}}$ within $^{63}R_{patch}$ by multipying the area ($\pi^{63}R^2_{patch}$) the patch covers by the areal Cu density ($1/a^2$) as such

$$N^{R_{patch}} = \frac{\pi^{63}R^2_{patch}}{a^2} \tag{4.9}$$

where we round $N^{R_{patch}}$ to the nearest integer. These $N^{R_{patch}}$ Cu sites within the radius $^{63}R_{patch}$ will uniformily share the donated holes from neighbouring $^{+2}$Sr ions. Next, we determine how many donated holes N^{κ}_{Sr} are to be shared within $^{63}R_{patch}$, where N^{κ}_{Sr} itself is the random number to be calculated. As shown in Fig. 4-4, there

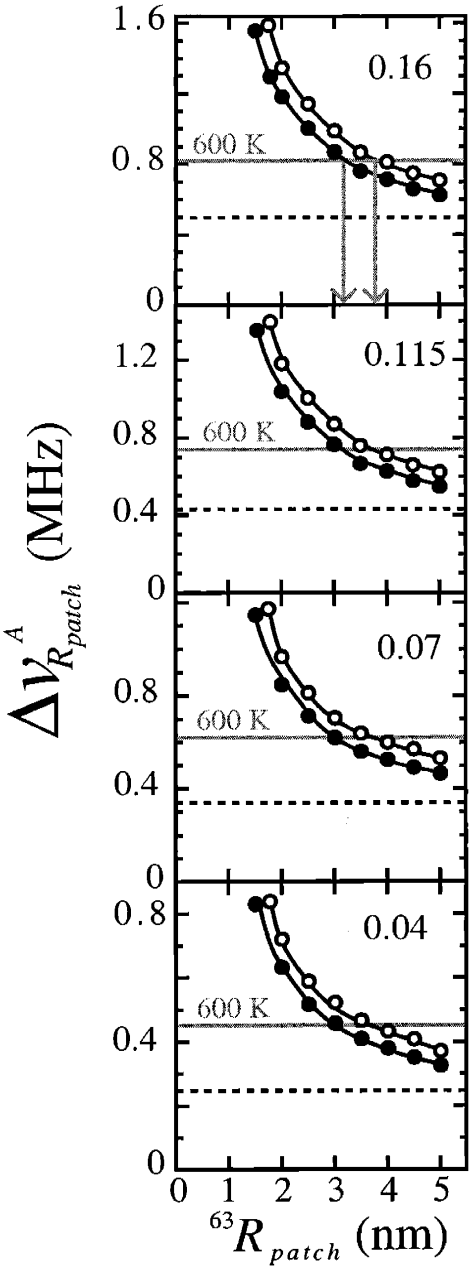

Figure 4-5: Calculated value of *HWHM* $\Delta\nu^{A}_{R_{patch}}$ (MHz) for the A-line as a function patch radius $^{63}R_{patch}$ (nm) for different x shown in each part using the $^{+2}$Sr dopant ions d_1 $\Delta\nu^{A}_{R_{patch},d_1}$ ($\circ$), and d_2 dopants $\Delta\nu^{A}_{R_{patch},d_2}$ ($\bullet$). Solid black curves through data are guides for the eye. Gray solid horizontal line shows experimental data $^{63}\Delta\nu^{A}_{Q}$ at 600 K while dashed black line shows intrinsic lattice width $\Delta\nu^{A}_{latt}$ reached in the limit $^{63}R_{patch} = \infty$.

are two distinct Sr/La sites, labelled d_1 and d_2, from which we can donate holes. This comes about because there are two distinct Sr/La sites within the unit cell. For donation of holes from d_1, we accept a donor hole into ${}^{63}R_{patch}$ provided there is a ${}^{+2}$Sr ion which satifies the position

$$\begin{aligned} \mathbf{r}^{d_1} &= [n_a a, n_b b, \pm 0.361c] \\ \sqrt{n_a^2 + n_b^2} &< {}^{63}R_{patch}/a \end{aligned} \tag{4.10}$$

relative to the Cu site at the origin. For donation of holes from d_2, we accept a donor hole into ${}^{63}R_{patch}$ provided there is a ${}^{+2}$Sr ion which satifies the position

$$\begin{aligned} \mathbf{r}^{d_2} &= [(n_a + 1/2)a, (n_b + 1/2)b, \pm 0.139c] \\ \sqrt{n_a^2 + n_b^2} &< {}^{63}R_{patch}/a \end{aligned} \tag{4.11}$$

and in both cases, n_a and n_b are $\pm$ integers ranging from zero to ∞. We do not a priori know which site d_1 or d_2 are the donor sites, or if the donors come from a combination of d_1 and d_2. We therfore treat both or combinations of both as equal possibilities. Technically, the n.n. (nearest neighbour) d_2 is the closest hole donor to the central Cu nucleus when occupied by a ${}^{+2}$Sr ion. The n.n. d_1 site on the other hand has more bonding with the central Cu via the apical oxygens. The n.n d_1 site has the largest effect on ${}^{63}\nu_Q$ when occupied by a ${}^{+2}$Sr ion and in particular gives rise to the B-site.

Once we have counted all the N_{Sr}^{κ} satisfying either Eq. (4.10) or Eq. (4.11) for a particular random configuration of ${}^{+2}$Sr ions κ, we deduce the local hole concentration ${}^{63}x_{local}^{\kappa}$ as such

$${}^{63}x_{local}^{\kappa} = N_{Sr}^{\kappa}/N^{R_{patch}} \tag{4.12}$$

We now carry out the EFG summation in Eq. (4.3) for the particular configuration of ${}^{+2}$Sr ions κ but with the following planar oxygen charge

$$q_{O_{pl}}^{\kappa} = -\left(2 - 2f_{\sigma}^{o} - {}^{63}x_{local}^{\kappa}/2\right)e \tag{4.13}$$

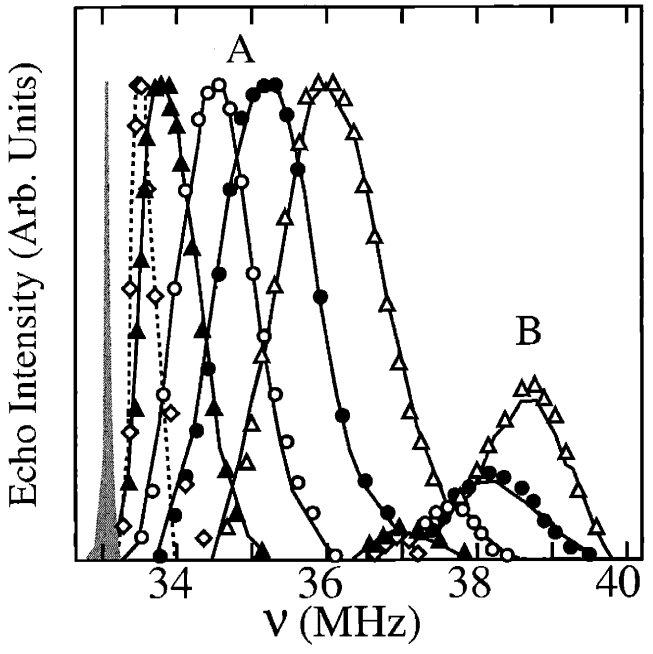

Figure 4-6: ^{63}Cu NQR lineshape at 600 K for $x = 0.16$ ($\triangle$), $x = 0.115$ ($\bullet$), $x = 0.07$ ($\circ$), $x = 0.04$ ($\blacktriangle$), $x = 0.02$ ($\diamond$) and $x = 0.0$ (grey region). Solid lines are fits using patch-by-patch model using d_1 dopants with lower bound to the patch radius $^{63}R_{patch} = 3.0 - 4.0$ nm are shown in Fig. 4-7.

for planar oxygens within the patch radius ${}^{63}R_{patch}$ where we have replaced x with ${}^{63}x^{\kappa}_{local}$ in Eq. (4.5). All other planar oxygen sites outside the radius ${}^{63}R_{patch}$, including those on other CuO_2 planes, are assigned the uniform hole concentration x. Using this scheme effectively ignores 3-d correlations of ${}^{63}x^{\kappa}_{local}$ from neighbouring CuO_2 planes, however, such effects are small and of higher order.

Using Eq. (4.3) and Eq. (4.13) the lattice summation is then computed for the configuration κ and ${}^{\kappa}V^{(\beta,\gamma),k}_{latt}$ is inserted into Eq. (4.2) and diagonalised to obtain ${}^{\kappa}V^{c,k}$ along the main principle axis which, even in the presence the random lattice, is very close to the c-axis in the tetragonal phase. Finally, we obtain a random frequency

$$ {}^{\kappa}\nu^{k} = \frac{e|{}^{63}Q|}{2h}{}^{\kappa} V^{c,k} \tag{4.14} $$

which is stored into a vector P^{k}_{ν}.

The position of ${}^{+2}$Sr ions is now re-randomized to obtain a new random configuration κ' of ${}^{+2}$Sr ions in the lattice, then a new value of ${}^{\kappa'}\nu^{k}$ is deduced and stored into P^{k}_{tot}. This proceedure is repeated $\sim 10^4$ times until a sufficient number of data points exist in P^{k}_{tot} so as to create a histogram spectrum of the lineshape over ~50 bins. The CG of the spectra $\langle P^{k}_{\nu} \rangle$ coincide with the means of the experimental data $\langle \nu^{k}_{Q} \rangle$ by design as we set the magnitude of the anti-shileding factors in a self-consistent way. The second moments are computed as such

$$ \begin{aligned} \langle P^{k}_{\nu} \rangle &= \frac{\sum_j P^{k}_{j,\nu}}{\sum_j} \\ \Delta\nu^{k}_{R_{patch}} &= \sqrt{\alpha_0} \cdot \sqrt{\frac{\sum_j \left(P^{k}_{j,\nu} - \langle P^{k}_{\nu} \rangle \right)^2}{\sum_j}} \end{aligned} \tag{4.15} $$

similar to Eq. (3.2).

We then repeat this whole proceedure and calculate $\Delta\nu^{k}_{R_{patch}}$ for various patch sizes, the results of which are shown in Fig. 4-5 for the A-line. The results for the B-line are exactly the same but with a uniform decrease $\Delta\nu^{B}_{R_{patch}}/\Delta\nu^{A}_{R_{patch}} = \zeta^{B}_{latt}/\zeta^{A}_{latt} = 0.67$. Also shown in Fig. 4-5 is how to deduce the best fit value of ${}^{63}R_{patch}$

to the lineshape at 600 K. We match experimental values of $\Delta\nu_Q^A$ shown by the gray horizontal line to the calculation shown by the solid black curves, and extrapolate ${}^{63}R_{patch}$ shown by the gray vertical arrows.

Note that according to the arrows, ${}^{63}R_{patch}^{d_2}$ deduced using dopants from ${}^{+2}$Sr ions at d_2 is 15 % smaller than ${}^{63}R_{patch}^{d_1}$ deduced using dopants from ${}^{+2}$Sr ions at d_1. Put in another way, when we do the calculation for fixed ${}^{63}R_{patch}$, we deduce a $\sim$ 15 % smaller value of $\Delta\nu^k_{R_{patch},d_2}$ compared to $\Delta\nu^k_{R_{patch},d_1}$. The reason for $\Delta\nu^k_{R_{patch},d_2} < \Delta\nu^k_{R_{patch},d_1}$ can be explained by a correlation between the local hole concentration ${}^{63}x^{\kappa}_{local}$ on the planar oxygens and the ${}^{+2}$Sr donor ions in n.n. positions to the origin. The result of adding one hole from a n.n. ${}^{+2}$Sr ion amounts to two separate shifts to the resonance frequency. The first shift is from the added hole itself which decreases of magnitude of the surrounding planar oxygen charge $|q_{O_{pl}}|$ and results in a large *increase* in the resonance frequency, regardless of the hole's origin. We shall define this shift as $\delta\nu^{pl}(>0)$. The second effect of adding one hole from a n.n. ${}^{+2}$Sr donor ion is from the n.n. ${}^{+2}$Sr ion itself which results in a shift $\delta\nu^{Sr}$, however, the sign of shift $\delta\nu^{Sr}$ depends on whether it is at d_2 or d_1.

Let us imagine scenario (1) where the added hole specifically comes from a ${}^{+2}$Sr ion in the n.n.n. (next nearest neighbour) d_1 site. We do not use the n.n. d_1 site in this case since this is the B-line which, according to the calculation, shows the *same* difference $\Delta\nu^B_{R_{patch},d_2} < \Delta\nu^B_{R_{patch},d_1}$ to the A-line. It can be shown that a ${}^{+2}$Sr ion in the n.n.n. d_1 site causes a small positive shift $\delta\nu^{d_1} > 0$, therefore the total shift $\delta\nu^{(1)}$ in scenario (1) is given by $\left(\delta\nu^{pl} + \delta\nu^{d_1}\right) = \delta\nu^{(1)}(>0)$ where both components are positive and enhance the total effect. Next let us imagine scenario (2) where the ${}^{+2}$Sr ion from which the added hole came from is specifically located at a n.n. d_2 position to the origin. It can be shown that placing a ${}^{+2}$Sr ion at the n.n. d_2 position causes a small *negative* shift $\delta\nu^{d_2} < 0$ to the resonance frequency. The total shift $\delta\nu^{(2)}$ in scenario (2) is therefore given by $\left(\delta\nu^{pl} + \delta\nu^{d_2}\right) = \delta\nu^{(2)}(>0)$ where the individual components counteract each other. Therefore, in scenario (1) the overall positive shift to the resonance frequency is enhanced while in scenario (2) it is not. After many random runs including the independent random effects from distant ${}^{+2}$Sr ions,

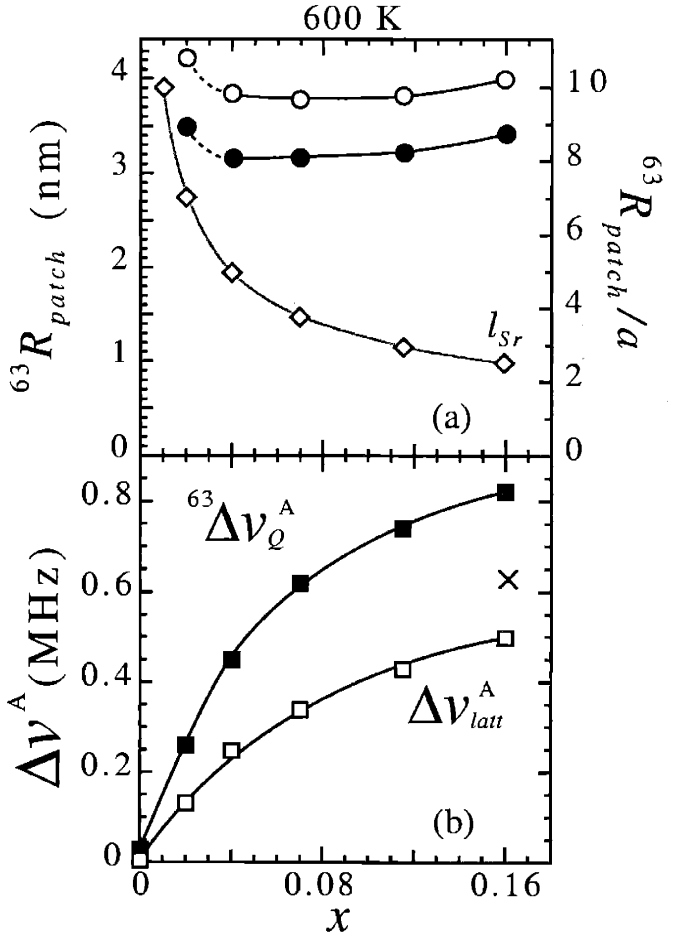

Figure 4-7: (a) Values for the lower bound to patch radius $^{63}R_{patch}$ (in units of nm on left axis and in multiples of lattice spacing a on right axis) used to fit spectra in Fig. 4-6 at 600 K using the $^{+2}$Sr donor ions d_1 (○) or d_2 (●) as donors. (◇) corresponds to $^{+2}$Sr-$^{+2}$Sr separation $l_{Sr} = a/\sqrt{x}$. (b) Experimentally deduced HWHM $^{63}\Delta\nu_Q^A$ (■) of spectra shown in Fig. 4-6 along with calculated intrinsic lattice broadening $^{63}\Delta\nu_{latt}^A$ for the A-line. All lines are a guide for the eye. Also shown is $\Delta\nu_{latt}^{T1}$ (×) for $x = 0.16$ deduced in appendix B.

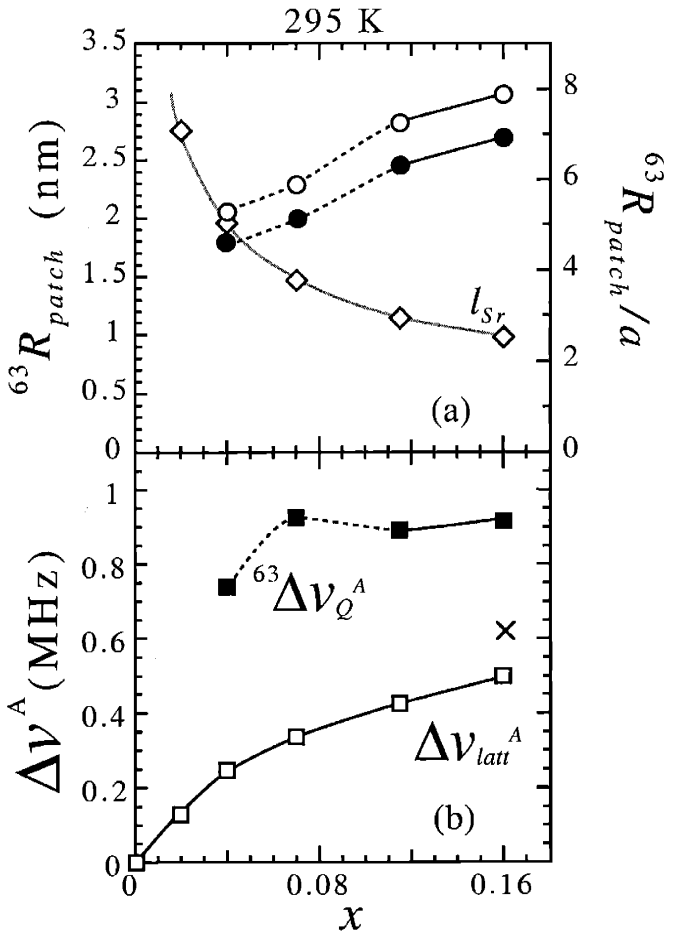

Figure 4-8: Same plot and symbols as Fig. 4-7 except at 295 K. Dashed black lines corresponds to orthorhombic structural phase for $x \leq 0.115$ according to LRO [100] and Fig. 2-3. All other lines are a guide for the eye.

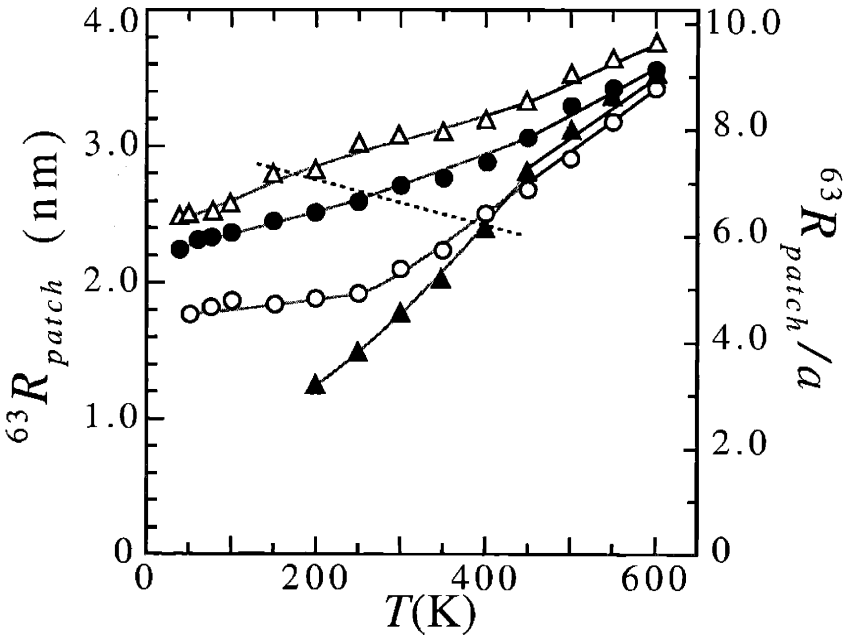

Figure 4-9: Temperature dependence of lower bound estimate of the patch radius $^{63}R_{patch}$ (defined according to average in Eq. (4.16)) deduced from the width of the ^{63}Cu NQR spectrum shown in Fig. 3-10 for $x = 0.16$ (△), $x = 0.115$ (•), $x = 0.07$ (○), $x = 0.04$ (▲). Gray lines show temperature region below T_Q where local orthorhombic distortions are present as deduced in Fig. 3-9. Dashed line corresponds to LRO structural temperature T_{st} [100].

scenario (1) will lead to a larger overall spread, therefore $\Delta\nu^k_{R_{patch},d_2} < \Delta\nu^k_{R_{patch},d_1}$.

In Fig. 4-6 we explicitly show the results for the best fit to the lineshape data at 600 K, shown by the solid black lines. The fits are deduced using d_1 dopants with $^{63}R^{d1}_{patch}$, however the same fits may be deduced using d_2 dopants with $^{63}R^{d2}_{patch}$. The values of $^{63}R^{d_1}_{patch}$ used to fit the data in Fig. 4-6, and the corresponding $^{63}R^{d_2}_{patch}$ that could equally well be used to fit the data, are shown in Fig. 4-7(a). In Fig. 4-6 we also show the data and fit for $x = 0.02$. As can be seen, however, the asymmetry in the experimentally observed line-profile for $x = 0.02$ is somewhat larger than our patch model can predict, hence we show the fit as a dashed line. It is interesting to note that in the range $x \leq 0.02$, $^{63}R^{d_1}_{patch}$ and $^{63}R^{d_2}_{patch}$ tend towards the average donor separation distance $l_{Sr} = a/\sqrt{x}$, as shown in Fig. 4-7. If $^{63}R_{patch} \simeq l_{Sr}$, our

model implies that each patch only covers one $^{+2}$Sr ion on average. In such a senario we no longer expect our model to account for the data. In fact, the critical region $x = 0.02$ which separates the spin glass phase and the anti-ferromagnetic phase for $x \leq 0.02$ [18] is known to show complex behaviour [16].

We also note in Fig. 4-6 that the intensity of the B-line is slightly underestimated by the calculation compared with the experimental data. This is simply due to the fact that the spin-spin relaxation rate is experimentally 10- 15 % smaller at the B-site together with the fact that we are measuring the data points using a finite pulse separation time $\tau = 12$ μs. After correcting for differences in the spin-spin relaxation rate, the observed relative intensity of the B-line decreases slightly and is shown in Fig. 4-3 to go as $f_B^{exp} \simeq x$, which is then consistent with the calculation. In order to fit the NQR spectrum in Fig. 4-6, we have attributed all of the extra line broadening to $^{63}R_{patch}$. In Fig. 4-7(b) we show the differences between the experimentally observed width $^{63}\Delta\nu_Q^A$ and the calculated intrinsic broadening $\Delta\nu_{latt}^A$. The difference between the two is accounted for by $^{63}R_{patch} \sim 3$ nm shown in part (a).

In Fig. 4-8 we show the same plot as Fig. 4-7 except for 295 K, where the $^{63}R_{patch}$ are deduced in a similar way to 600 K shown in Fig. 4-5. At 295 K, we see an effect not present at 600 K, namely that the observed linewidth $^{63}\Delta\nu_Q^A$ below $x < 0.115$ in Fig. 4-8(b) for 295 K no longer monotonically decrease with decreasing x as it does at 600 K. Also shown in Fig. 4-8 is the onset of the orthorhombic structural phase according to LRO [100] and Fig. 2-3 as a function of x at 295 K, shown as the dashed lines through the data points. The result of the observed enhancement of the linewidths $^{63}\Delta\nu_Q^A$ for $x \leq 0.115$ in Fig. 4-8(b) results in a large drop in the calculated $^{63}R_{patch}$ shown in Fig. 4-8(a). Comparing the x dependence in $^{63}R_{patch}$ within the tetragonal phase at 600 K and at 295 K for $x \geq 0.115$ seems to suggest that $^{63}R_{patch}$ is more or less x independent *provided* that the local lattice distortions do not dramatically enhance the observed NQR linebroadening.

The effects of the orthorhombic distortions can also be seen in Fig. 4-9 where we

plot the temperature dependence of the average ${}^{63}R_{patch}$ defined as such

$$ {}^{63}R_{patch} = \frac{{}^{63}R_{patch}^{d_1} + {}^{63}R_{patch}^{d_2}}{2} \tag{4.16} $$

In Fig. 4-9 we chose to plot the average value ${}^{63}R_{patch}$ alone for clarity, which corresponds to taking half of the donors from d_1 sites and half from d_2 sites. In Fig. 4-9 the black and grey lines correspond to regions above and below T_Q taken from Fig. 3-9, while the dashed line shows the onset of LRO T_{st} [100]. In the case of $x = 0.04$ we clearly see a dip in ${}^{63}R_{patch}$ below $T_Q \simeq T_{st}$ which is most likely due to the fact that we have neglected distributions in the local orthorhombic distortions. In chapter 4.4 we make the reasonable assumption that ${}^{63}R_{patch}$ continues to decrease lineaarly with decreasing temperature as shown for the $x \geq 0.115$ samples, and we thereby make an estimate of the local distributions in orthorhombic distortions.

4.3.1 Deducing ${}^{63}x_{patch}$

In the temperature region above T_Q we can also deduce an upper boundary ${}^{63}x_{patch}$ for the spatial vaiation ${}^{63}x_{local}$ without any further computation. We proceed exactly as in chapter 4.3 but for each random lattice configuration κ, we also store each value ${}^{63}x_{local}^{\kappa}$ used to compute ${}^{\kappa}\nu_Q^k$ into a new vector P_X^k. We then build up a vector P_X^k of randomly distributed local hole concentrations for each lattice configuration κ. The mean of the set P_X^k is just the nominal value $\langle P_X^k \rangle = x$, while the effective $HWHM$ defined in an analogous manner to Eq. (4.15) as such

$$ \begin{aligned} \langle P_X \rangle &= \frac{\sum_j P_{(j,X)}}{\sum_j} = x \\ {}^{63}\Delta x_{patch} &= \sqrt{\alpha_0} \cdot \sqrt{\frac{\sum_j \left(P_{(j,X)} - x\right)^2}{\sum_j}} \end{aligned} \tag{4.17} $$

The calculated ${}^{63}\Delta x_{patch}$ is found to be independent of which site $k = (A, B)$ is computed. By deducing ${}^{63}\Delta x_{patch}$ over a large range of parameters $[x, {}^{63}R_{patch}]$, we

find our calculated values of ${}^{63}\Delta x_{patch}$ fit well to the Binomial theorem

$$\begin{aligned} {}^{63}\Delta x_{patch} &= \sqrt{\alpha_0} \cdot \sqrt{\frac{x(1-x)}{N^{R_{patch}}}} \\ &= \frac{a}{{}^{63}R_{patch}} \sqrt{\frac{\alpha_0}{\pi} x(1-x)} \end{aligned} \tag{4.18}$$

where we have used the relation in Eq. (4.9) for the last line. In Fig. 3-7 we show the temperature dependence of ${}^{63}x_{patch}$ deduced using Eq. (4.18) with the average ${}^{63}R_{patch}$ defined in Eq. (4.16), together with Eq. (4.1). Using ${}^{63}R^{d_1}_{patch}({}^{63}R^{d_2}_{patch})$ instead of Eq. (4.16) results in a small $-(+)7$ % variation in ${}^{63}\Delta x_{patch}$.

The fact that ${}^{63}x_{patch} \sim {}^{63}x_{local}$ suggests that (a) our patch-by-patch model is appropriate in describing the spatial variation in ${}^{63}x_{local}$ (b) our estimate of the intrinsic lattice broadening ${}^{63}\Delta\nu_{latt}$ is correct in the temperature region above T_Q and (c) the static value ${}^{63}x_{patch}$ deduced from the lineshape analysis is consistent with the low frequency dynamic value ${}^{63}x_{local}$ deduced using ${}^{63}1/T_1$.

4.4 Local Orthorhombic Distortions

In the orthorhombic phase, the CuO_6 octahedra are effectively tilted an angle $\theta_c \leq 5^o$ [72] away from the c-axis towards the b_o-axis, and the primitive lattice constants in the plane are split $b_o > a_o$. We calculate the effect of these distortions to the EFG by placing the ions in an orthorhombic cell [24] (see Fig. 4-4) with appropriate orthorhombic modulations [24, 72] and compute the changes to the ${}^{63}\nu_Q$. However, we already know from Fig. 3-9 that the curvature of ${}^{63}\nu_Q$ starts change above the structural phase transition temperature T_{st} deduced from neutron and X-ray diffraction results [72]. These bulk probes detect LRO, whereas NQR is a local probe, therefore it is more appropriate to deduce the local orthorhombic distortions from our ${}^{63}\nu_Q$ data, and then compare them with LRO results.

The orthorhombic distortions cannot *a priori* be deduced from the NQR data alone. We must first take certain know relations from LRO results and apply them to NQR. In particular, we shall use the neutron diffraction results reported by P.G.

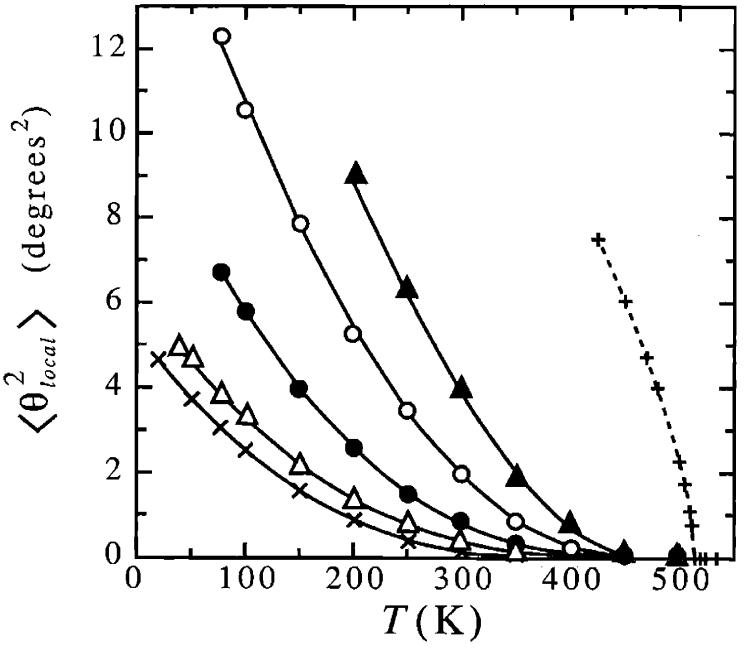

Figure 4-10: Temperature dependence of the local structural parameter squared, or equivalently the CuO_6 octahedron tilting angle squared, $\langle\theta^2_{local}\rangle$ (in degrees ^{2}) for $x = 0.20$ ($\times$), $x = 0.16$ ($\triangle$), $x = 0.115$ ($\bullet$), $x = 0.07$ ($\circ$), $x = 0.04$ ($\blacktriangle$) and $x = 0.0$ ($+$) deduced from the curves shown in Fig. 3-9(a).

Radaelli *et al* [72] which demonstrate that certain measured orthorhombic distortions such as the orthorhombic strain $(b_o - a_o)$, the tilting angle $\theta_c \leq 5^o$ which measures the departure of the O_{ap}-Cu-O_{ap} angle from the c-axis, and the "scissors" angle $\theta_{scis} \leq 90^o$ which measures the O_{pl}-Cu-O_{pl} angle, are all related to powers of the underlying orthorhombic order parameter we define as $\theta_{LRO}(x,T)$.

At low temperatures ($\lesssim$ 70 K) where lattice fluctuations are small, mean-field theory gives a good account of the observed the lattice distortions [72]. In light of this, we fit the data in Ref. [72] to a mean-field like form and deduced

$$\begin{aligned} \theta_c &\simeq \theta_{LRO}(x,T) \\ \theta_{scis} &\simeq 90 - 4 \cdot 10^{-2} \cdot [\theta_{LRO}(x,T)]^2 \\ (b_o - a_o) &\simeq 6 \cdot 10^{-4} \cdot \frac{(b_o + a_o)}{2} \cdot [\theta_{LRO}(x,T)]^2 \end{aligned} \tag{4.19}$$

where all angles are in degrees. These set of equations provide a constraint for the orthorhombic distortions which determine the position $\mathbf{r}_j(x,T)$ of the jth ion in the lattice. We now assume the LRO constraints in Eq. (4.19) also apply to the *local* constraints which determine the local position $\mathbf{r}_j(x,T)$ of the jth ion in the lattice. However, we now replace the LRO parameter $\theta_{LRO}(x,T)$ in Eq. (4.19) by the *local* structural parameter $\theta_{local}(x,T)$ as such $\theta_{local}(x,T) \equiv \theta_{LRO}(x,T)$.

The EFG lattice summation in Eq. (4.4) is now carried out in a similar way as described in chapter IVa but with the orhthorhombic distortions incoroprated into the positions of the ions. The positions $\mathbf{r}_j(x,T)$ of the ions are deduced using the absolute values of the lattice constants a_o and c at 295 K from Fig. 2-3 along with their corresponding thermal coefficients α_a and α_c as before, however, we allow b_o to vary according to the constraints in Eq. (4.19) and the unknown local structural parameter $\theta_{local}(x,T)$. We position the La/Sr ions and the apical oxygen ions according to the tilting angle $\theta_c = \theta_{local}(x,T)$ away from the c-axis towards to the b_o direction, and the planar oxygens are positioned according to θ_{sc} in Eq. (4.19) and the unknown local structural parameter $\theta_{local}(x,T)$. We now have all the ionic positions $\mathbf{r}_j(x,T)$ as a function of the $\theta_{local}(x,T)$. Using the charges in Eq. (4.5), we now compute the

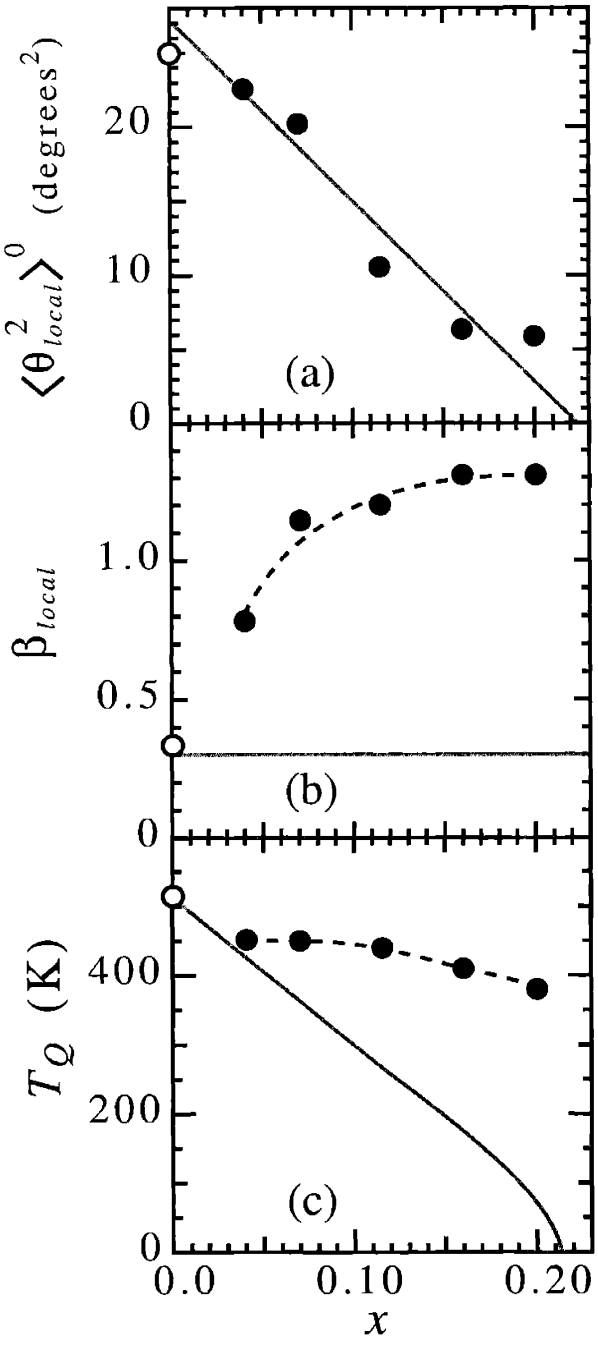

Figure 4-11: x dependence of coefficients of local structural parameter $\langle\theta^2_{local}\rangle$ including (a) maximum octahedron tilting angle squared $\langle\theta^2_{local}\rangle^0$ (degrees^2), (b) reduced temperature coefficient β_{local}, and (c) onset temperature T_Q (K) for $x = 0.0$ (○) and $x > 0.0$ (●). Dashed lines as guides for the eye. Solid gray lines are equivalent LRO patameters (a) $(\theta^0_c)^2$ (degrees^2) [72], (b) β [6,24], and (c) T_{st} [100].

EFG lattice summation in Eq. (4.4) and using the anti-shielding factors we calculate the resonance frequency $\langle \nu_\theta^A \rangle$ as a function of θ_{local}.

The results of the calculation suggest that the increase in $\langle \nu_\theta^A \rangle$ due to the effect of the orthorhombic distortions *alone*, defined as $\delta \langle \nu_\theta^A \rangle$, goes as

$$\delta \langle \nu_\theta^A \rangle \simeq c_0 \cdot \langle \theta_{local}^2 \rangle \tag{4.20}$$

where $c_0 \simeq +\ 0.12$ MHz/[degree^2] is x and T independent within $\sim \pm 10$ %. Note that in this model, NQR does not distinguish between $\pm\theta_{local}$, only the average square magnitude $\langle \theta_{local}^2 \rangle$ across the whole sample. Another conclusion we deduced from the calculation was that after diagonalising the EFG tensor, the main principle axis is tilted an angle $|\theta_{NQR}|$ away from the c-axis, where $|\theta_{NQR}| \simeq 0.9|\theta_{local}|$, while the asymmetry parameter η remains small $\eta < 0.06$.

We are now in a position to deduce the average $\langle \theta_{local}^2 \rangle$ from our experimental data $\langle {}^{63}\nu_Q^A \rangle$ in Fig. 3-9. The results of the fit are already shown as the gray and black lines in Fig. 3-9 and the values of $\langle \theta_{local}^2 \rangle$ used to deduce the gray lines in the temperature region $T < T_Q$ are shown in Fig. 4-10.

In the spirit of the LRO results, we deduced the temperature dependence of $\langle \theta_{local}^2 \rangle$ in Fig. 4-10 using the paramteric form

$$\langle \theta_{local}^2 \rangle = \langle \theta_{local}^2 \rangle^0 \cdot \left(\frac{T_Q - T}{T_Q} \right)^{2\beta_{local}} \tag{4.21}$$

where $\langle \theta_{local}^2 \rangle^0$ is the square averaged tilting angle at $T = 0$ K, β_{local} is the reduced temperature coefficient, and T_Q is local onset temperature for the orhorhombic distortions, all three of which depend on x and are taken as free variables. In Fig. 4-11 we summarize the x dependence of all three parameters $\langle \theta_{local}^2 \rangle^0$, β_{local} and T_Q and compare them with equivalent mean field parameters $(\theta_c^0)^2$, β and T_{st} according to LRO [72, 100], shown as the solid gray lines.

In the case of $x = 0.0$, all three parameters deduced by NQR are consistent with equivalent LRO parameters deduced by neutron and X-ray diffraction. We find that

$\beta_{local} \simeq 0.34$ according to NQR for $x = 0.0$, which is consistent with the LRO critical exponent $\beta \simeq 0.30$ according to neutron and X-ray scattering for all x [6, 24]. A similar critical exponent is also found in $La_{2-x}Ba_xCuO_4$ where $\beta = 0.33$ [86], which are all consistent with the theoretical prediction of $\beta = 0.35$ for a 3D XY model. For $x \leq 0.04$ we find consistent values between $\langle\theta^2_{local}\rangle^0$ and $(\theta^0_c)^2$. In the case of β_{local} and T_Q for $x > 0.04$, however, we find qualitatively differences with β and T_{st}, respectively. The fact that $\beta_{local} \sim 1$ for $x > 0.04$ indicates that locally, the transition into the orthorhombic phase is somewhat smeared in temperature. The fact that $T_Q \gtrsim 400$ K indicates that the local onset temperature is rather high and roughly x independent.

In the order-disorder dominated structural transitions proposed by local probes [12, 28] in the region $x > 0.15$, θ_{local} is argued to be locally finite in the LRO tetragonal phase $T > T_{st}$, but averaged over large length scales, $\langle\theta_{local}\rangle = 0$ implying that there is an equal probability of $\pm|\theta_{local}|$ across the whole sample. Furthermore, in the order-disorder type model, the onset of LRO for $T < T_{st}$ is a consequence that certain regions, while still retaining the same temperature independent magnitude of distortion $|\theta_{local}|$, start to preferentially tilt in a particular direction and on average over the sample $\langle\theta_{local}\rangle > 0$. The temperature dependence then arises as more and more regions preferentially align along $+|\theta_{local}|$ with decreasing temperature for $T < T_{st}$. Averaged over large length scales in the region $T < T_{st}$ will result in the appearance of a displacive transition where the magnitude of the tilting angle θ_{LRO} appears to increase with decreasing temperature. In the region $0.0 < x \lesssim 0.15$, a mixture of displacive and order-disorder type scenarios is shown to exist [12, 28].

Our new NQR results combined with LRO results support a purely displacive structural transition for $x \lesssim 0.04$, and mixture of displacive and order-disorder type structural transition in the region $x > 0.04$. For $x > 0.04$ in the region $T < T_Q$, NQR evidences local orthorhombic tilting of a displacive nature, i.e. the tilting angle of each octahedra increases with decreasing temperature below $T < T_Q$ where $\langle\theta^2_{local}\rangle > 0$. In the region $T_{st} < T < T_Q$, however, θ_{local} averaged over large length scales is $\langle\theta_{local}\rangle = 0$, i.e. there is an equal probability of $\pm|\theta_{local}|$. In the region $T <$

T_{st}, the octahedra tilting angle continues to increase with decreasing temperature, however, certain regions start to preferentially align along one direction, i.e. $\langle\theta_{local}\rangle > 0$, in an order-disorder type scenario. Our results are consistent with other local probes [12, 28], but in addition we have deduced the onset temperature T_Q for local orthorhombic distortions. In the case of $x = 0.20$ we find that $T_Q \sim 350$ K even though the LRO structural transition disappears [100].

4.4.1 Distribution in Orthorhombic Distortions

In all of our analysis of the ^{63}Cu NQR linebroadening thus far, we have ignored potential linebroadening from local lattice distortions. In the previous section we deduced the temperature dependence of the square *average* distortions $\langle\theta^2_{local}\rangle$ across the sample using the CG data $\langle {}^{63}\nu_Q^A\rangle$. We shall deduce the corresponding *distribution* of θ_{local} using the *HWHM* data ${}^{63}\Delta\nu_Q^A$. As discussed earlier, there exist three linebroadening mechanisms for the ^{63}Cu NQR lineshape (a) the random placement of $^{+2}$Sr ions in the lattice (b) the patch-by-patch variation in hole concentration ${}^{63}x_{local}$, and (c) the local lattice distortions. In 3.3 we used both broadening mechanisms (a) and (b) to account for the experimental data and deduced the lower bound ${}^{63}R_{patch}$ for the spatial variation ${}^{63}x_{local}$. We shall now use all three mechanisms (a),(b) and (c) to account for the observed *HWHM* data ${}^{63}\Delta\nu_Q^A$ in the case of $x = 0.04$. Note that we cannot *a priori* separate (a),(b) and (c), therefore in order to obtain the contribution from (c), we must first make reasonable assumptions for (a) and (b).

In Fig. 4-12 we plot the temperature dependence of the observed data ${}^{63}\Delta\nu_Q^A$ for $x = 0.04$ above and below $T_Q = T_{st} = 450$ K (▲) taken from Fig. 3-10. For $T > T_Q$ we continue to attribute all of the observed linebroadening to mechanism (a) and (b) $\Delta\nu^A_{R_{patch}}$ where ${}^{63}R_{patch}$ is optimized such that $\Delta\nu^A_{R_{patch}} = {}^{63}\Delta\nu_Q^A$. For $T < T_Q$, we make the ansatz that the underlying $\Delta\nu^A_{R_{patch}}$ continues to increase *linearly* as shown by the (×) symbols in Fig. 4-12. Assuming that $\Delta\nu^A_{R_{patch}}$ does indeed follow the (×) symbols in Fig. 4-12 instead of the experimental data (▲) results in a more reaslistic linear decrease in ${}^{63}R_{patch}$ with decreasing temperature rather than the drop below T_Q shown in Fig. 4-9. The left over broadening for $T < T_Q$ is then attributed to

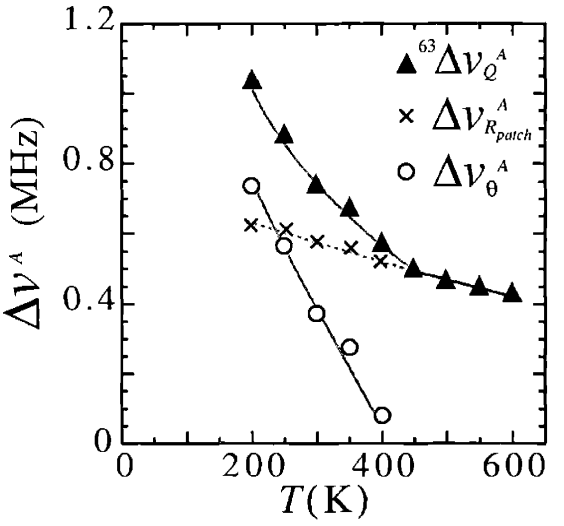

Figure 4-12: Temperature dependence of experimental $HWHM$ $^{63}\Delta\nu_Q^A$ for = 0.04 (▲) taken from Fig. 3-10 where black and gray lines show temperature region above and below $T_Q = T_{st} = 450$ K, together with $\Delta\nu_{R_{patch}}^A$ (×) assuming linear continuation of $\Delta\nu_Q^A$ below T_Q. The difference between experiment (▲) and linear extrapolation (×) may be attributed to extra width from orthorhombic distortions defined as $\Delta\nu_\theta^A$ (○).

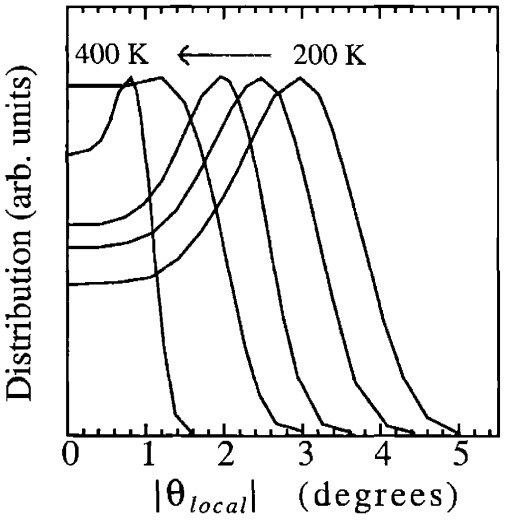

Figure 4-13: Distribution of magnitude of local tilting angle $|\theta_{local}|$ deduced from $\Delta\nu_\theta^A$ (○) in part Fig. 4-12. Arrow shows direction of increasing temperature.

mechanism (c) which represents the contribution from the lattice broadening whose *HWHM* $\Delta\nu_\theta^A$ (defined in a similar fashion to Eq. (3.2)).

We now have a constraint for $\Delta\nu_\theta^A$ below $T < T_Q$ given our assumption for $\Delta\nu_{R_{patch}}^A$ in Fig. 4-12 and the observed experimental data ${}^{63}\Delta\nu_Q^A$. Making the reasonable assumption $\Delta\nu_\theta^A$ and $\Delta\nu_{R_{patch}}^A$ are independent of each other results in the following constraint

$$ {}^{63}\Delta\nu_Q^A \simeq \sqrt{\left(\Delta\nu_{R_{patch}}^A\right)^2 + \left(\Delta\nu_\theta^A\right)^2} \tag{4.22} $$

We shall also make the assumption that all of the extra lattice broadening $\Delta\nu_\theta^A$ comes from distributions in the local tilting angle $|\theta_{local}|$ with the constraint that the average $\langle\theta_{local}^2\rangle$ is consistent with Fig. 4-10 for $x = 0.04$ at each temperature.

Next we generate a hypothetical probability distribution function for $|\theta_{local}|$ by taking a Gaussian distribution of the squared variable θ_{local}^2 centered at $\langle\theta_{local}^2\rangle$, with a width which shall be optimized to reproduce $\Delta\nu_\theta^A$ in Eq. (4.22) and Fig. 4-12. Examples of the distribution function for $|\theta_{local}|$ ($\equiv \sqrt{\theta_{local}^2}$) are shown in Fig. 4-13. Next, we proceed as in 3.3 and calculate the local hole concentration ${}^{63}x_{local}^\kappa$ for a random configuration of ${}^{+2}$Sr ions κ. We also independently choose a random value of $|\theta_{local}^\kappa|$ taken from the probability distribution functions shown in Fig. 4-13. Next, the positions of the all the ions in the lattice are calculated given the value of the local orthorhombic distortion $|\theta_{local}^\kappa|$, and all placed accordingly. We then take the lattice summation in Eq. (4.4) incorporating the positions of the ions in the distorted lattice together with the hole concentration ${}^{63}x_{local}^\kappa$ and calculate the main principle value of the diagonalised resonance frequency ${}^\kappa\nu^A$ as in Eq. (4.14). The resultant main principle axis turns out to be tilted an angle $\theta_{NQR} \simeq |\theta_{local}^\kappa|$ away from the c-axis. ${}^\kappa\nu^A$ is stored into a vector P_θ and a new random lattice κ' is re-generated along with a new value of $|\theta_{local}^{\kappa'}|$ according to the probability distribution functions, and the corresponding resonance frequency ${}^{\kappa'}\nu^A$ is stored into P_θ. As before, we repeat this proceedure $\sim 10^4$ times until P_θ is sufficiently produce a histogram spectrum. P_θ is calculated for various widths of the distribution functions of $|\theta_{local}|$ until the experimental observed lineshape is reproduced. The final optimized results of the

distribution functions of $|\theta_{local}|$ are shown in Fig. 4-13.

In order to best recreate the observed NQR spectrum one must use trial and error for the probability distribution functions of $|\theta_{local}|$, with the constraint that the CG of the distribution function is given by the values in Fig. 4-10. The final results for the probability distribution functions of $|\theta_{local}|$ are shown in Fig. 4-13.

Chapter 5

^{17}O NMR

5.1 NMR techniques

We used high-quality single crystals of $La_{2-x}Sr_xCuO_4$ with nominal hole concentrations of $x = 0.025, 0.035, 0.05, 0.07, 0.115$ and 0.15 with masses ranging from $100 - 500$ mg for our ^{17}O NMR measurements. The crystals were grown at M.I.T. (x=0.025,0.035,0.07), at Tohoku (x=0.115) and Tokyo (x=0.05 and 0.15) using an optical image furnace. ^{17}O isotope enrichment was carried out by annealing the crystals in $^{17}O_2$ enriched gas for 100 hrs at 900 C. Sample allignment for each crystal was achieved using Laue diffraction. The single crystals were not taken over 475 K in order to insure that the oxygen content did not alter from one experimental run to another. The EPMA on the $x = 0.15$ crystal was discussed previously in chapter 2.1.

For NMR experiments, one applies an external magnetic field $H_0 = 9$ Tesla which interacts with the nuclear spin vector $\mathbf{I}$ as such

$$\mathcal{H}_{spin} = -^{17}\gamma_n \hbar \mathbf{I} \cdot \left(1 + ^{17}\mathbf{K}_{app}\right) \cdot \mathbf{H}_0 \tag{5.1}$$

$^{17}\gamma_n/2\pi = 5.772$ MHz/Tesla is the bare gyro-magnetic ratio for ^{17}O, and $^{17}\mathbf{K}_{app}$ is the anisotropic apparent Knight shift which we are interested in. $I = 5/2$ in the case of ^{17}O, which according to Eq. (5.1), gives rise to $(2I + 1) = 5$ transitions. These 5 transitions are split by the quadrupole interaction into 5 well separated lines.

The central transition of the ^{17}O NMR spectrum corresponds to nuclear transitions $(m_I \leftrightarrow m_I')$ (Eq. (2.2)) given by $(-1/2 \leftrightarrow +1/2)$. The central transition has the advantage that it is broadened by local distributions in the uniform $(\mathbf{q} = \mathbf{0})$ part of the static *spin* susceptibilty χ'_{spin}, and does not have any appreciable broadening due to charge effects (i.e. no quadrupole broadening). The central transition is therefore ideal for measuring the inhomogeneity through the spin channel, and we use it to compare with the inhomogeneity measured through the charge channel in chapter 4 .

For experimental convenience we choose the c direction as the quantization axis and we apply the the magnetic field along the crystallographic c-axis. We can express the apparent Knight shift along the c-axis, $^{17}K^c_{app}$ (Eq. (5.1)), as such

$$^{17}K^c_{app}(x,T) = {}^{17}K^c_{orb} + {}^{17}K^c_{spin}(x,T) \tag{5.2}$$

where $^{17}K^c_{orb} = (+0.018\ \%)$ is the constant orbital (Van-Vleck) contribution, while $^{17}K^c_{spin}$ is the spin Knight shift we are interested in (for clarity we have already subtracted the small second order quadrupole shifts, typically $\simeq 0.01\%(\ll K_{spin})$, to central transition data in this thesis). $^{17}K^c_{spin}$ and the local spin susceptibility are related as such

$$^{17}K^c_{spin} = \frac{2C^c}{N_A\mu_B}\chi'^c_{spin}(\mathbf{q} = \mathbf{0}) \tag{5.3}$$

where χ'_{spin} is the local static spin susceptibilty (in units of emu/[mol f.u.]), and C^c is the hyperfine coupling constant from a single Cu neighbor (in units of kOe/μ_B) along the c direction discussed in chapter 2 (Eq. (2.23)).

Since the ^{17}O NMR linewidth were sharp, typical $FWHM \leq 40$ kHz (i.e. much less than the band-width $\sim$ 100 kHz of our d.c. amplifiers (chapter 2.3)), we employed the FFT (fast Fourier transform) method to measure the spectra. This consisted of taking the FFT of the spin-echo in Fig. 2-6. We also used the same sequence shown in Fig. 2-6 to measure $^{17}1/T_1$. We found that the time dependence of the magnetisation $M(t)$ fit well to the standard recovery for a $I = 5/2$ nucleus dominated by a single

valued magnetic relaxation mechanism $^{17}1/T_1$ as such [64]

$$M(t) = M(\infty) + (M(0) - M(\infty)) \cdot \sum_j \left[a_j \exp\left(\frac{-r_j}{T_1} t\right)\right] \tag{5.4}$$

In the case of the central transition $[a_j, r_j] = \left[\frac{50}{63}, 15; \frac{8}{45}, 6; \frac{1}{35}, 1\right]$.

We measured $^{17}1/T_1^c$ at various positions across central transition using a one shot run which consisted of measuring the spin-echo sequence (Eq. (5.4)) at the CG of the spectrum for various delay times t, then using the FFT of each echo to determine the $M(t)$ at each desired shift. All $^{17}1/T_1^c$ recoveries fit well to single magnetic relaxation within experimental uncertainties except when interference from apical oxygen sites gave an additional slow $^{17}1/T_1^{ap}$ component to the planar oxygen recoveries, and prohibited our measurement of $^{17}1/T_1^c$. The apical oxygen's spin shift, linewidth and $^{17}1/T_1^{ap}$ is less than the planar's because the apicals are located out of the CuO_2 plane and have a smaller hyperfine coupling constants to the uniform static and dynamic spin susceptibilities in the plane. The only crystals which had overlap for the central transition in 9 Tesla were $x = 0.025$, and to some extent $x = 0.035$, where the planar spin shift was smallest, approaching that of the apical shift.

In our analysis of the ^{17}O NMR data, we define the Knight shift at the CG of the NMR spectrum as $\langle {}^{17}K^{\alpha} \rangle$, and the $HWHM$ $^{17}\Delta K^c$ of the spectrum as such

$$\begin{aligned} \langle {}^{17}K^c \rangle &= \frac{\sum_j I_j^{17} K_j^c}{\sum_j I_j} \\ {}^{17}\Delta K^c &= \sqrt{\alpha_0} \cdot \sqrt{\frac{\sum_j I_j \left({}^{17}K_j^c - \langle {}^{17}K^c \rangle\right)^2}{\sum_j I_j}} \end{aligned} \tag{5.5}$$

where I_j and $^{17}K_j^c$ represent the intensity and shift of each data point j that constitutes the FFT spectrum along the c direction, and $\alpha_0 = Ln(4)$. Eq. (5.5) is entirely analogous to Eq. (3.2).

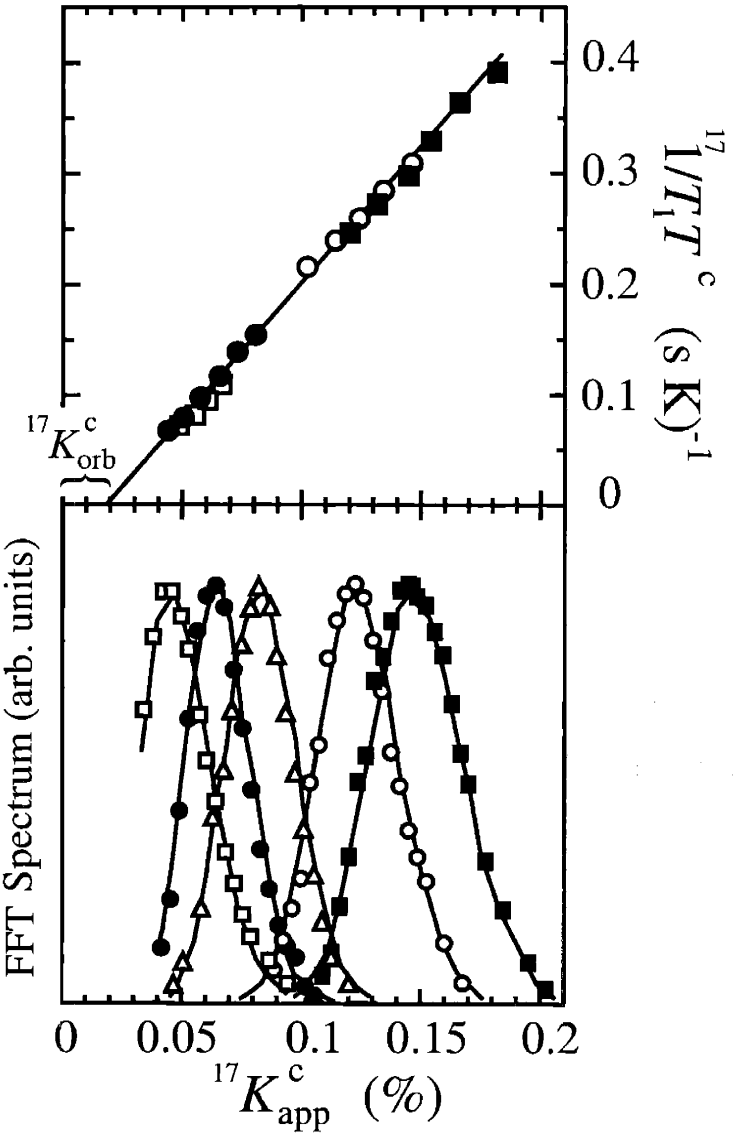

Figure 5-1: (a) Frequency dependence of ^{17}O NMR spin-lattice relaxation rate divided by temperature T, $^{17}1/T_1T^c$ (sK)$^{-1}$, across NMR spectra ($^{17}K^c_{app}$) presented in (b). Solid line in (a) is best fit to Eq. (5.7) with slope $\beta = 2.4 \pm 0.2$ (sK%)$^{-1}$ and K-axis offset equal to constant $^{17}K^c_{orb} = +0.018$ % defined in Eq. (5.2). (b) Planar ^{17}O FFT spectrum (arbitrary units) at the central transition as a function of apparent shift for c-axis aligned $La_{2-x}Sr_xCuO_4$ single crystals with $x = 0.15$ (■), $x = 0.115$ (○), $x = 0.07$ (△), $x = 0.05$ (•) and $x = 0.035$ (□). All data are taken at a fixed temperature of 295 K. Missing data points for $x = 0.035$ and 0.05 in (b) indicate region where apical oxygen signal coincides. Solid lines are best fits using a patch-by-patch model of the spatial variation in $^{17}x_{local}$ with a patch radius $^{17}R_{patch} = 3.0 - 3.5$ nm.

5.2 ^{17}O NMR Experimental results

5.2.1 $^{17}1/T_1$ scaling

The key new ^{17}O NMR evidence for the inhomoegeneous electronic state is presented in Fig. 5-1 where in (a) we show the frequency dependence, or equivalently the apparent Knight shift ($^{17}K^c_{app}$) dependence, of the spin-lattice relaxation rate divided by temperature T, $^{17}1/T_1T^c$, at the central transition of the planar ^{17}O nucleus with H_0 along the c-axis. In (b) we present the FFT (Fast Fourier transform) spectra over which $^{17}1/T_1T^c$ is measured. All data are taken at 295 K. Fig. 5-1 immediately establishes two important points regarding the inhomogeneous electronic state: firstly in (b) we see that the broadening of the central transition defined as the *HWHM* (half width at half maximum) $^{17}\Delta K^c_{app}$ results in a clear overlap of the spectrum from crystal to crystal. This suggests that within each crystal with nominal $^{+2}$Sr concentration x, there exists a substantial static distribution in the local electronic state. As an example, the upper (lower) half intensity point of the $x = 0.05$ crystal approximately coincides with the CG (center of gravity) of the $x = 0.07$ (0.035) crystal respesctively, which indicates that the more metallic regions of the $x = 0.05$ crystal have $^{17}x_{local} = 0.07$, while the more insulating regions have $^{17}x_{local} = 0.035$, at 295 K. By taking the deviations of $^{17}x_{local}$ from the nominal x, we can deduce the amplitude of the spatial variation $^{17}\Delta x_{local}$ as such

$$^{17}x_{local} = x \pm^{17} \Delta x_{local} \tag{5.6}$$

which in this particular case gives $^{17}\Delta x_{local} = 0.018(2)$. $^{17}x_{local}$ thus deduced is only an upper boundary since we do not *a priori* know that the inhomogeneous linebroadening $^{17}\Delta K^c_{app}$ is dominated by the $^{17}\Delta K^c_{spin}$ through $^{17}x_{local}$. For example, the NMR linewidth is often dominated by impurity spins, and shows a Curie-like temperature dependence in magnetic materials. The mechansim of the milder temperature dependence of the broad ^{17}O NMR linewidth in $La_{2-x}Sr_xCuO_4$ has been a mystery since the 1980's.

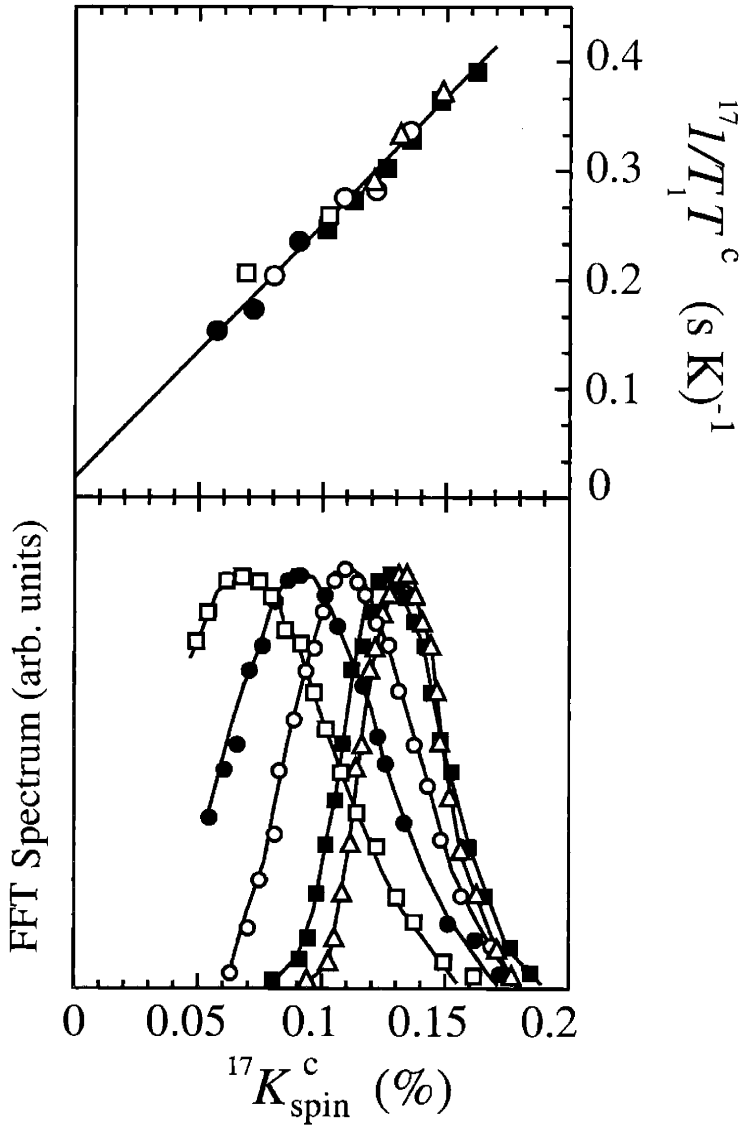

Figure 5-2: (a) Frequency dependence of ^{17}O NMR $^{17}1/T_1T^c$ (sK)$^{-1}$ for $x = 0.15$ across NMR spectra $^{17}K^c_{spin}$ (%) presented in (b). Solid line in (a) is the best fit to Eq. (5.7) with slope $\beta' = 2.2 \pm 0.2$ (sK%)$^{-1}$ (excluding 100 K data). (b) Planar ^{17}O FFT spectrum (arbitrary units) at the central transition for $x = 0.15$ at 366 K (△), 295 K (■), 230 K (○), 166 K (•), and 100 K (□). Missing data points in (b) indicate region where apical oxygen signal coincides. Solid lines are best fits using a patch-by-patch model of the spatial variation in $^{17}x_{local}$ with a patch radius $^{17}R_{patch} = 2.0 - 4.2$ nm in order of increasing T respectively.

The crucial step is shown in Fig. 5-1(a) where we find that the universal empirical scaling relation

$$^{17}1/T_1T^c = \beta\ ^{17}K^c_{spin} \tag{5.7}$$

holds *quantitatively* across *each* lineshape, and we find the slope of the linear fit is given by $\beta = 2.4 \pm 0.1$ $(\mathrm{sK\%})^{-1}$. We recall that in $YBa_2Cu_3O_{6.6}$ whose ^{17}O NMR linewidth is a factor ~ 2 smaller than our $x = 0.15$ crystal at 100 K, M. Takigawa *et al.* [91] found that the same scaling law holds with $\beta^{(CG)} \sim 2.0 \pm 0.2(\mathrm{sK\%})^{-1}$ when $^{17}1/T_1T^c$ and $^{17}K^c_{spin}$ were measured at the CG of the spectrum *as a function of temperature.*

Finding that the scaling relation in Eq. (5.7) holds *across each spectrum* immediately rules out the possibilty that the line broadening is primarily due to some kind of "dirt" effect similar to the effects of localised spins induced by ^{+2}Zn impurities, but rather that there exists a genuine local variation in the electronic state which dominates the inhomogeneous linewidth of the central transition. In terms of the linebroadening, this implies that $^{17}\Delta K^c_{app} \simeq^{17} \Delta K^c_{spin}$ for all crystals at 295 K. This now allows us to directly extract $^{17}x_{local}$ from the extent of the overlap between crystals as outlined above.

Our next task is to confirm that the same relation in Eq. (5.7) holds at different temperatures. In Fig. 5-2 we show the scaling across the inhomogeneous broadening $^{17}K^c_{spin}$, where we have subtracted $^{17}K^c_{orb} = +0.018$ % taken from Fig. 5-1, however, instead of keeping T fixed and varying x, in Fig. 5-2 we keep $x = 0.15$ fixed but vary T. As we can see, the best fit linear extrapolation of the data points shown (excluding 100 K) results in a consistent value for the slope $\beta' = 2.2 \pm 0.3$ $(\mathrm{sK\%})^{-1}$. Similar results to Fig. 5-2 hold for other crystals which now permit us to determine $^{17}x_{local}$ from the extent of the overlap as a function of temperature. However, note that in Fig. 5-2, the experimental data starts to deviate from the scaling relation (Eq. (5.7)) in the temperature region $T \lesssim 100$ K. We find a similar effect for other crystals. Defining the temperature below which scaling no longer holds as T_{scale}, we find that $T_{scale} =$ (300 K, 250 K, 175 K, 100 K) ($\pm$10 K) for the crystals $x = (0.035, 0.05, 0.115, 0.15)$,

respectively. Since the scaling relation in Eq. (5.7) no longer holds in the region $T < T_{scale}$, we limit our analysis of ${}^{17}x_{local}$ to the region $T_{scale} < T < 475$ K. We discuss the departure from scaling in more detail later in this chapter and in appendix D.

5.2.2 ${}^{17}K_{spin}$ and ${}^{17}x_{local}$

In Fig. 5-3 we present the temperature dependence of the spin Knight shift ${}^{17}K^c_{spin}$ at the central transition for the series of samples [103]. Each spectrum was taken by FFT of the spin echo in the time domain. The data points in Fig. 5-3 correspond to the CG , $\langle {}^{17}K^c_{spin} \rangle$, while the the error bars correspond to the *HWHM*, $\pm {}^{17}\Delta K^c_{spin}$, both of which are determined using Eq. (5.5). We choose to plot the data in this fashion in order to illustrate the increasing spectral overlap (and therefore ${}^{17}\Delta x_{local}$) with decreasing temperature. In Fig. 5-3 we also show the temperature scale T_{scale} (dashed line) below which the scaling relation in Eq. (5.7) no longer holds.

The temperature dependence of ${}^{17}\Delta K^c_{spin}$ is shown explicitly in Fig. 5-4. We see a monotonic increase of ${}^{17}\Delta K^c_{spin}$ (or the FFT linewidth, equivalently) from 475 K down to $\sim T_{scale}$, below which ${}^{17}\Delta K^c_{spin}$ saturates. The temperature dependence for ${}^{17}\Delta K^c_{spin}$ is consistent with previous findings for poly-crystalline aligned $x = 0.15$ [25].

As was explicitly shown in Fig. 5-1 and Fig. 5-2, there is a clear overlap of the spectrum from crystal to crystal due to the fact that ${}^{17}x_{local} \neq x$. In order to carry out a quantitative analysis of ${}^{17}x_{local}$, we first establish $\langle {}^{17}K^c_{spin} \rangle$ at the CG as a function of nominal hole concentration x at a fixed temperature shown in Fig. 5-5 at 295 K. The solid black line shows the linear interpolation whose slope we define as $\delta_x \langle {}^{17}K^c_{spin} \rangle$ for constant T. The linear relation between the CG, $\langle {}^{17}K^c_{spin} \rangle$, and nominal x, *together* with the scaling relation in Eq. (5.7) suggests a linear relation between ${}^{17}K^c_{spin}$ and ${}^{17}x_{local}$ across the entire spectrum. We therefore take a direct relation between the width $\pm {}^{17}\Delta K^c_{spin}$ and $\pm {}^{17}\Delta x_{local}$, given the slope $\delta_x \langle {}^{17}K^c_{spin} \rangle$ which is illustrated in the case of $x = 0.115$. In equation form, the relation can be expressed as

$$ {}^{17}\Delta x_{local} = \left[\delta_x \langle {}^{17}K^c_{spin} \rangle \right]^{-1} \cdot {}^{17}\Delta K^c_{spin} \tag{5.8} $$

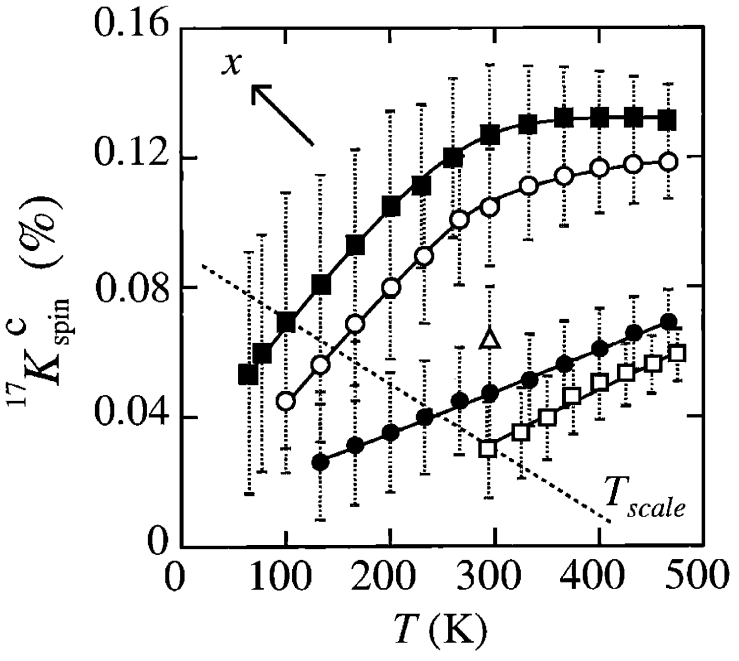

Figure 5-3: Temperature dependence of the spin Knight shift $^{17}K^{c}_{spin}$ for $x = 0.15$ (■), $x = 0.115$ (○), $x = 0.07$ (△), $x = 0.05$ (●) and $x = 0.035$ (□). Data points indicate CG of spectrum $\langle {}^{17}K^{c}_{spin} \rangle$, while error bars indicate $HWHM$ $\pm {}^{17}\Delta K^{c}_{spin}$ determined using Eq. (3.2). All curves are guides for the eye and dashed tilted line shows T_{scale}.

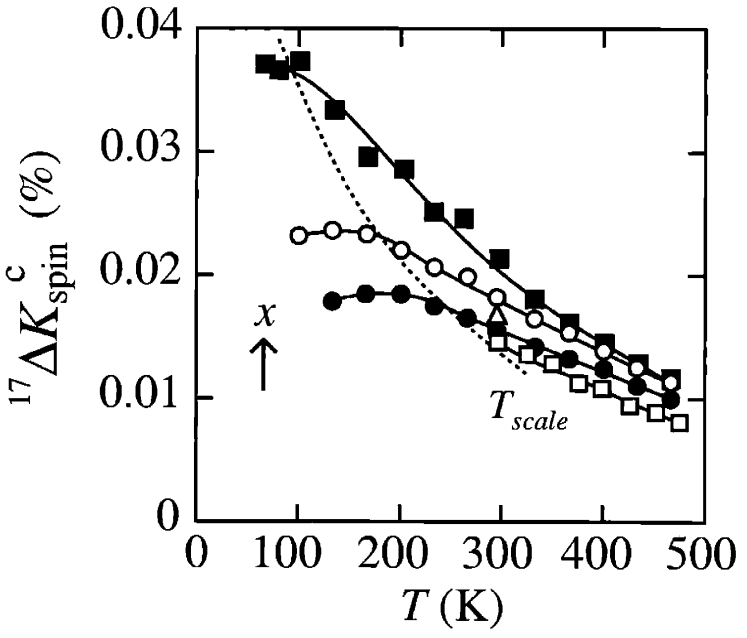

Figure 5-4: Temperature dependence of the $HWHM\ ^{17}\Delta K^{c}_{spin}$ (%) for $x = 0.15$ (■), $x = 0.115$ (○), $x = 0.07$ (△), $x = 0.05$ (●) and $x = 0.035$ (□). Solid lines are a guide for the eye and dashed curve shows T_{scale}.

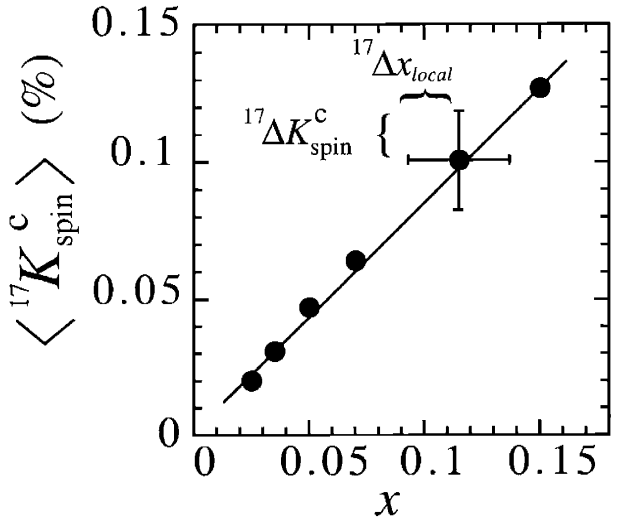

Figure 5-5: Spin Knight shift at the CG $\langle {}^{17}K^{c}_{spin} \rangle$ (•) as a function of nominal hole concentration x for 295 K. Also shown are $\pm {}^{17}\Delta K^{c}_{spin}$ and corresponding $\pm {}^{17}\Delta x^{c}_{local}$ for $x = 0.115$.

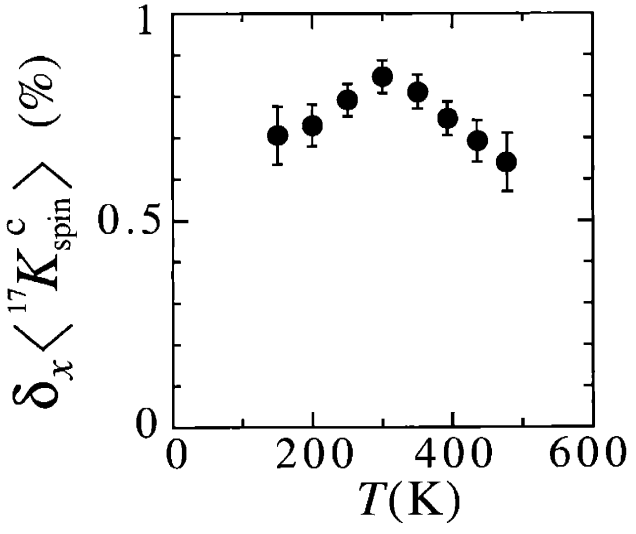

Figure 5-6: Temperature dependence of the first derivative $\delta_x \langle {}^{17}K^{c}_{spin} \rangle$ (•) deduced by linear intrapolation, an example of which is shown by the slope of the solid line fit in Fig. 5-5 at 295 K.

Since $\delta_x \langle {}^{17}K^c_{spin} \rangle$ is defined at fixed temperature T, we carry out the same process in Fig. 5-5 for different temperatures and determine $\delta_x \langle {}^{17}K^c_{spin} \rangle$ as a function of temperature, shown in Fig. 5-6. We then insert ${}^{17}\Delta x_{local}$ deduced from Eq. (5.8) into Eq. (5.6) to get ${}^{17}x_{local}$.

As summarized in Fig. 5-7, our results for the spatial variation ${}^{17}x_{local}$ are semi-quantitatively the same as ${}^{63}x_{local}$ taken from Fig. 3-7, which adds weight to our interpretations. The frequency dependence in ${}^{63}1/T_1$ does not necessarily imply a frequency dependence in ${}^{17}1/T_1T$, and the fact that ${}^{17}x_{local} \sim^{63} x_{local}$ has further consequences. As discussed in chapter 2, ${}^{63}1/T_1$ probes the low energy spin susceptibility (i.e. low energy spin fluctuations) near $\mathbf{q} = \mathbf{Q_{AF}} = (\pi/a, \pi/a)$, while ${}^{17}1/T_1T$ probes the low energy spin susceptibility *away* from $\mathbf{Q_{AF}}$ at $\mathbf{q} \approx \mathbf{0}$. Similarly, ${}^{17}K_{spin}$ probes the static susceptibility *away* from Q_{AF}, exactly at $\mathbf{q} = \mathbf{0}$. Furthermore, the linebroadening of the ^{63}Cu NQR line over which ${}^{63}1/T_1$ varies is from the *charge* channel while the linebroadening of the ^{17}O NMR line over which ${}^{17}1/T_1$ varies is from the *spin* channel, therefore our findings suggest a strong correlation between the spatial inhomogeneity in the charge and spin channels across the Brillouin zone.

5.3 Deducing ${}^{17}R_{patch}$

We now turn our attention to the real-space *static* picture of ${}^{17}x_{local}$. By using a simplified version of the analysis in chapter 4, we deduce the length scale ${}^{17}R_{local} =$ 3-4 nm (8-10 a) of the spatial variation, and show that it is consistent with previous estimates [79] using ^{63}Cu NQR. When using the spectra ${}^{17}K^c_{spin}$ to deduce ${}^{17}x_{local}$ we are dealing with the uniform *static* response from the bulk of the material [104]. The appropriate "static" timescale for NMR in this case [11] is given by the inverse spectral width $\gtrsim 0.1$ ms. Any dynamics faster than this timescale are unobservable. However, as we have shown using the scaling relation in Eq. (5.7), the uniform dynamic response given by ${}^{17}1/T_1T^c$ at the specified timescale $2\pi/\omega_n \simeq 0.012\mu$s is equivalent to the static response.

We carry out exactly the same procedure as in chapter 4, but without any quadrupole

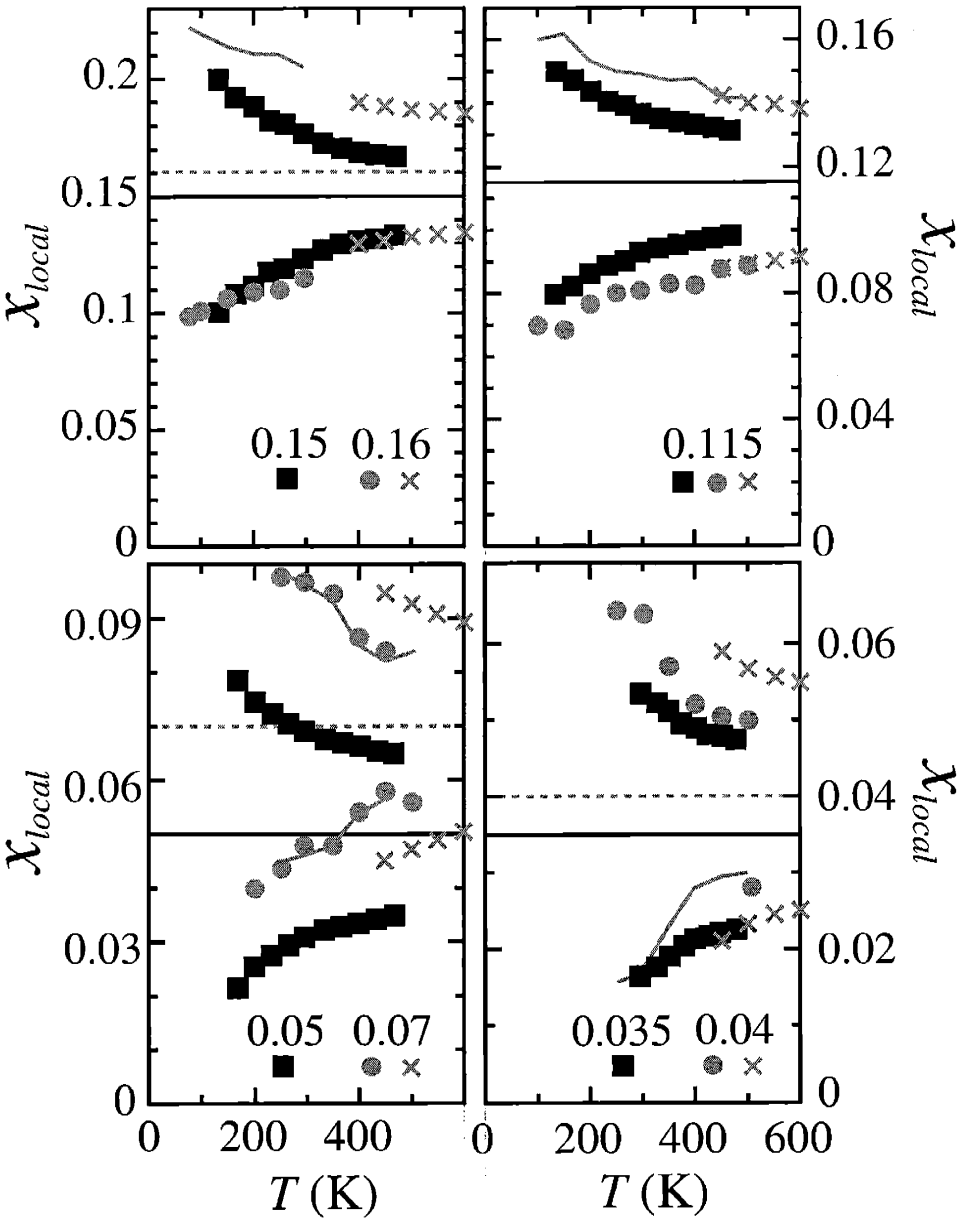

Figure 5-7: Temperature dependence of the local hole concentration $x_{local} = x \pm \Delta x_{local}$ (where Δx_{local} is the amplitude or extent of the spatial variation) according to ^{17}O NMR data $^{17}x_{local}$ (■) on single crystals where the nominal hole concentration x is listed in each part and shown as the horizontal black lines and dashed gray lines. Also shown are $^{63}x_{local}$ (gray •) and the upper boundary $^{63}x_{patch}$ (gray ×) according to ^{63}Cu NQR data taken from Fig. 3-7.

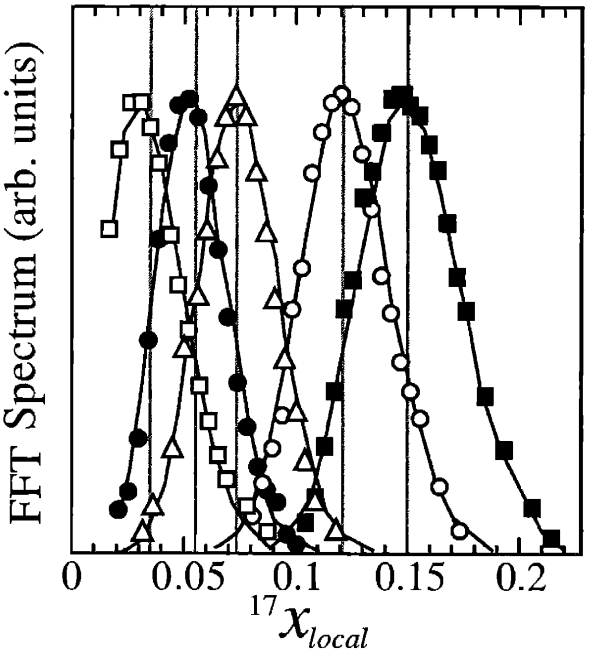

Figure 5-8: ^{17}O NMR spectrum at 295 K taken from Fig. 5-1(b) but with the K-axis converted from $^{17}K^{c}_{spin}$ to local hole concentration $^{17}x_{local}$ using experimentally determined parameters (see text). Solid black curves are fits using the patch-by-patch model for the spatial variation with a patch radius $^{17}R_{patch} = 3.0 - 3.5$ nm. Gray vertical line corresponds to the optimized CG x' for $x = 0.035$ ((□) with $x' = 0.034$), $x = 0.05$ ((•) with $x' = 0.054$), $x = 0.07$ ((△) with $x' = 0.070$), $x = 0.115$ ((○) with $x' = 0.120$) and $x = 0.15$ ((■) with $x' = 0.149$).

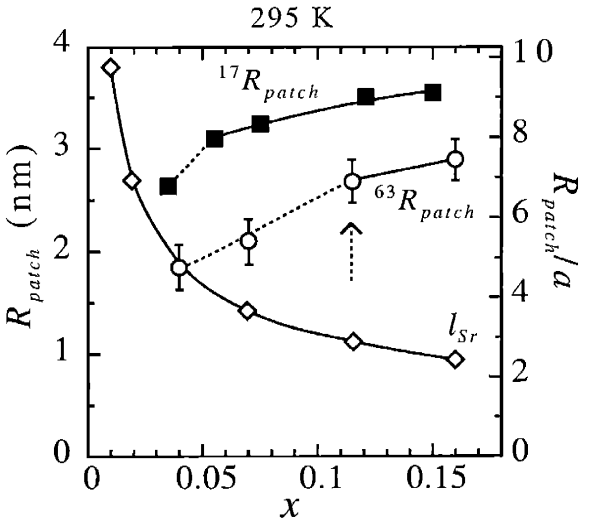

Figure 5-9: Summary at 295 K of length scales $^{17}R_{patch}$ (□). We also show $^{63}R_{patch}$ (•) and average $^{+2}$Sr-$^{+2}$Sr separation distance $l_{Sr} = a/\sqrt{x}$ (◇) as a function of nominal hole concentration x taken from Fig. 4-8. Lines are a guide for the eye. Left axis shows length scale in units of nm, while right axis is in units of the lattice constant a. Dashed arrow indicates onset LRO into orthorhombic structural phase $x \leq 0.115$ [100].

effects. We first as assign a patch radius $^{17}R_{patch}$ as is Fig. 4-1 (Note that we define $^{17}R_{patch}$ with a superscript ^{17} since we are using the ^{17}O NMR data to deduce it while for the lower bound $^{63}R_{patch}$ we are using ^{63}Cu NQR data). We assign a random number λ according to Eq. (4.6) at each of the d_1 donor sites (Fig. 4-4) (note that using d_1 or d_2 donors in this case makes no difference since there are no quadrupole effects involved). This defines the random configuration of $^{+2}$Sr donors ions κ. We then count the number of $^{+2}$Sr donors N_{Sr}^{κ} and deduce the local hole concentration $^{17}x_{local}^{\kappa}$ as such

$$^{17}x_{local}^{\kappa} = N_{Sr}^{\kappa}/N^{R_{patch}} \tag{5.9}$$

where $N^{R_{patch}}$ is defined in Eq. (4.9). $^{17}x_{local}^{\kappa}$ is then stored into a vector P_X. We then re-randomize the lattice to give a new configuration κ' of $^{+2}$Sr ions, and count the number of generated donors which satisfy Eq. (4.10) $N_{Sr}^{\kappa'}$. $^{17}x_{local}^{\kappa'}$ is then deduced using Eq. (5.9) whose value is also stored into P_X. This whole proceedure is repeated

using $\sim 10^4$ different random configurations of donor ions until P_X is sufficiently large to be sectioned into a histogram spectrum $P_{(j,X)}$ with a reasonable number of bins j, where typically $\sum_j \simeq 50$. Examples of the histogram spectrum $P_{(j,X)}$ using the optimized values of two free parameters $[x', {}^{17}R_{patch}]$ are shown as the solid black lines in Fig. 5-8 for each crystal with nominal the experimental data taken from Fig. 5-1 using the following proceedure: we first subtract ${}^{17}K^c_{orb} = +0.018$ % from all the data in Fig. 5-1, then we scale the K-axis using the linear relation between ${}^{17}K^c_{spin}$ and ${}^{17}x_{local}$. This amounts to multiplying the K-axis by the scaling factor $\left[\delta_x \left\langle {}^{17}K^c_{spin} \right\rangle\right]^{-1}$ taken from Fig. 5-5. The experimental data points, including the observed asymmetry of the lineshape, are successfully reproduced by the histogram spectrum $P_{(j,X)}$ using the optimized values $[x', {}^{17}R_{patch}]$.

The CG (center of gravity), given by $\langle P_X \rangle = x'$, and the effective *HWHM*, ${}^{17}\Delta x_{patch}$, of the histogram spectrum $P_{(j,X)}$ are defined in the same manner to Eq. (3.2) except that we optimize the CG x' (gray vertical lines) of the histogram spectrum $P_{(j,X)}$ for each crystal x. We note that due to slight misalignment with the magnetic field, we encountered a small systematic error $\Delta\nu_{sys} \sim \pm$ 2 kHz (or ${}^{17}\Delta K_{sys} \sim 0.005$ % ($\ll \left\langle {}^{17}K^c_{spin} \right\rangle$), equivalently) between different runs of experiments. We attribute the small shifts ± 0.005 of the optimized value x' from nominal x to such errors. Once x' is optimized, we optimize ${}^{17}R_{patch}$ by imposing the condition

$$ {}^{17}\Delta x_{patch} = {}^{17}\Delta x_{local} \tag{5.10} $$

where ${}^{17}\Delta x_{patch}$ is determined using Eq. (4.17) as a function of the free parameter ${}^{17}R_{patch}$, and ${}^{17}\Delta x_{local}$ are the experimental data taken from Fig. 5-7. After optimizing ${}^{17}R_{patch}$ by satisfying Eq. (5.10), we successfully reproduce the experimentally observed data points shown in Fig. 5-8. We also find that our calculation fit well to the same Binomial relation in Eq. (4.18), i.e. ${}^{17}\Delta x_{local} \propto 1/{}^{17}R_{patch}$.

The best fit values of ${}^{17}R_{patch}$ used to fit the data in Fig. 5-8 are summarized in Fig. 5-9, along with the average ${}^{+2}$Sr to ${}^{+2}$Sr separation l_{Sr} (or average hole separation distance) $l_{Sr} \simeq a/\sqrt{x}$ nm [7]. We also show previous independent results

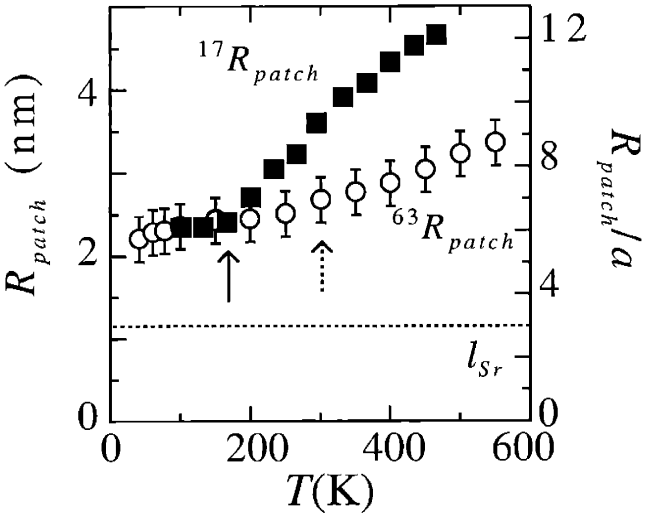

Figure 5-10: Temperature dependence of patch radius for $x = 0.115$ including $^{17}R_{patch}$ (■) and $^{63}R_{patch}$ (○) taken from Fig. 4-9. Dashed horizontal line indicates average $^{+2}$Sr-$^{+2}$Sr separation distance l_{Sr}=1.2 nm for $x = 0.115$. Dashed arrow indicates onset of LRO into orthorhombic structural phase [100], while solid arrow indicates T_{scale}.

of the lower bound estimate $^{63}R_{patch}$ determined from the inhomogeneous broadening of the ^{63}Cu NQR spectrum taken from Fig. 4-8. In Fig. 5-9 we see a sharp drop in $^{63}R_{patch}$ for $x < 0.115$ which coincides with the region of LRO (long range order) into the orthorhombic structural phase (at 295 K) [72, 100]. $^{17}R_{patch}$, on the other hand, is deduced by the inhomogeneous broadening across the spin channel and is not effected by the lattice distortions, however, for $x \leq 0.035$ the apical and planar spectra coincide which limits the accuracy with which $^{17}R_{patch}$ can be determined. For these reasons, we turn the solid line extrapolation of $^{17}R_{patch}$ and $^{63}R_{patch}$ into a dashed lines below x =0.035 and 0.115 respectively. As discussed in chapter 4, we do not expect our patch model to be valid in the region $^{17}R_{patch} \sim l_{Sr}$ where on average, each patch covers only one $^{+2}$Sr ion. If we continue to extrapolate the solid line for $^{17}R_{patch}$ to lower x, we therefore expect our simplified model to break down at $x \sim 0.02$, which coincides with the appearance of the Néel phase for $x \leq 0.02$ in oxygen depleted samples [18].

In Fig. 5-10 we present the temperature dependence of $^{17}R_{patch}$ and the lower bound $^{63}R_{patch}$ for $x = 0.115$. Both $^{17}R_{patch}$ and $^{63}R_{patch}$ show a consistent decrease with decreasing temperature. Below T_{scale} (shown by the vertical arrow), $^{17}R_{patch}$ starts to saturate due to the fact that the linewidth shown in Fig. 5-4 saturates, however, the validity of our model is questionable in this tempeature region. Other samples show similar temperature dependence to $x = 0.115$. We note that the temperature dependence of $^{17}R_{patch}$ and $^{63}R_{patch}$ is qualitatively different to that of the anti-ferromagnetic correlation length ξ_{AF} which *increases* with decreasing temperature [7, 46]. This rules out the possibility that R_{patch} and ξ_{AF} are simply related to each other. Rather, R_{patch} should be considered as an independent length scale which desrcibes the segragation of holes in the presence of a random distribution of $^{+2}$Sr ions. We remark that similar patch-by-patch models of disordered doping in the CuO_2 plane have been independently used to account for the smeared density of states found in photoemission peaks as a result of a distribution in the superconducting gap [53]. The free parameter used to account for the smearing in the density of states is the length scale of the model which is determined by the in plane superconducting coherence length $\xi_{ab} \sim 2.0 - 3.0$ nm [85]. It is interesting to note that $^{17}R_{patch} \simeq 2.5$ nm (Fig. 5-10) in the region of T_{scale} is comparable to ξ_{ab}.

5.4 Departure from Scaling

As shown in chapter 2, $^{17}A(\mathbf{q})^{\alpha}$ decreases as $\simeq (\mathbf{q} - \mathbf{Q_{AF}})^2$ in the vicinity of $\mathbf{Q_{AF}}$. Therefore $^{17}1/T_1T^c$ is dominated by contributions away from the wave-vector $\mathbf{Q_{AF}}$. In Fig. 5-11 we present the temperature dependence of $\langle ^{17}1/T_1T^c \rangle$ at the CG of the central transition for all samples, and from 475 K down to T_{scale}, we see the same overall temperature dependence as $\langle ^{17}K^c_{spin} \rangle$ shown in Fig. 5-3. To show this explicitly, in Fig. 5-12 we cross-plot $\langle ^{17}1/T_1T^c \rangle$ (from Fig. 5-11) and $\langle ^{17}K^c_{spin} \rangle$ (from Fig. 5-3), where x and T are the implicit parameters. The scaling relation at the CG of each spectrum shown in Fig. 5-12 has slope $\beta^{(CG)} = 2.5 \pm 0.2$ $(\mathrm{sK\%})^{-1}$ which agrees with $\beta = 2.4 \pm 0.2$ $(\mathrm{sK\%})^{-1}$ found in Fig. 5-1 for the scaling across the inhomogeneous

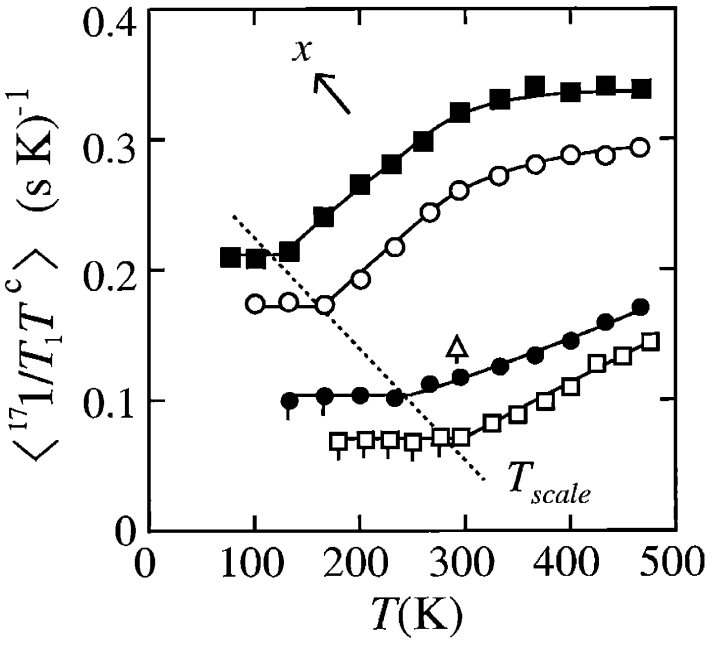

Figure 5-11: Temperature dependence of $\langle {}^{17}1/T_1T^c \rangle$ at the CG of the the central transition for $x = 0.15$ (■), $x = 0.115$ (○), $x = 0.07$ (△), $x = 0.05$ (•) and $x = 0.035$ (□). Symbols with small dashes underneath indicate $\langle {}^{17}1/T_1T^c \rangle$ measured at the CG of the first lower satellite transition instead of the central transition due to interference of the apical oxygen signal at the central transition (note that both central and satellite transitions gave the same results at their CG in the temperature regions where both were measurable). Dashed line indicates temperature region T_{scale}, and solid lines are a guide for the eye.

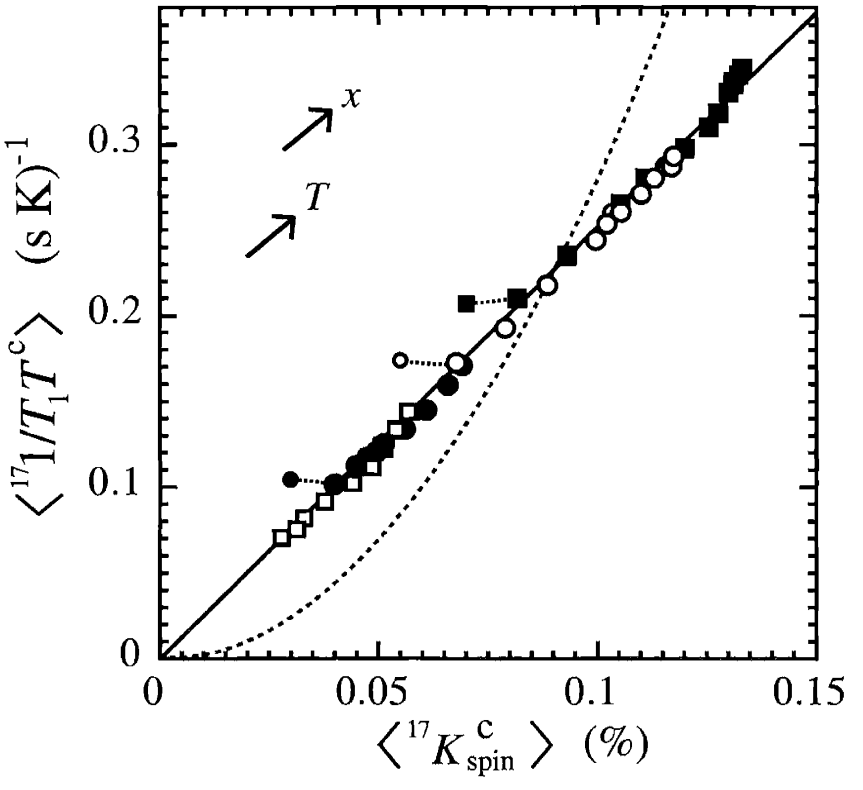

Figure 5-12: $\langle {}^{17}1/T_1T^c \rangle$ at the planar oxygen site as a function of spin Knight shift $\langle {}^{17}K^c_{spin} \rangle$, both taken at the CG of the spectrum for $x = 0.15$ (■), $x = 0.115$ (○), $x = 0.05$ (●) and $x = 0.035$ (□). Solid line shows linear fit to scaling form $\langle {}^{17}1/T_1T^c \rangle = \beta^{CG} \langle {}^{17}K^c_{spin} \rangle$ with slope $\beta^{CG} = 2.5 \pm 0.2$ (sK%)$^{-1}$, which is consistent with the slope $\beta = 2.4 \pm 0.2$ (sK%)$^{-1}$ found in Fig. 5-1 across the inohomogeneous linewidth. Dashed gray curve illustrates the Korringa relation for Fermi liquid. Data points which deviate from the scaling relation correspond to temperatures below T_{scale} and are not included in the linear fit.

broadening for various x at constant temperature. In appendix D we fit the scaling region to the phenomenological expression by H. Monien, P. Monthoux, and D. Pines (MMP) [58] and deduce the band-width parameter $\sim J(\simeq 130$ meV) (Eq. (1.1)) for the uniform spin susceptibility.

The scaling between the spin dynamics and the spin shift is eventually broken below the temperature region T_{scale}. Below T_{scale}, we find that $^{17}1/T_1T^c$ saturates (Fig. 5-11) while $^{17}K^c_{spin}$ continues to decrease (Fig. 5-12) with decreasing temperature. We also find that the temperature dependence of the linewidth (Fig. 5-4) saturates below T_{scale}.

One possible reason for the departure from scaling is that $^{17}1/T_1T^c$ picks up contributions from growing *incommensurate* spin fluctuations [54] at the NMR frequency near $\mathbf{q} \approx \mathbf{Q_{AF}}$ [43]. The presence of finite incommensurability implies that the hyperfine form factor in Eq. (2.23) does not entirely filter out the AF fluctuations, thereby causing an enhancement in $^{17}1/T_1T^c$ over the uniform susceptibility $^{17}K^c_{spin}$ and departure from scaling.

Another possible reason for the departure from scaling is that for $T \leq T_{scale}$ there are a growing number of regions where $^{17}x_{local}$ is very small. We see this in Fig. 5-7 where at T_{scale}, $^{17}x_{local}$ for the insulating side gets closer and closer to zero, implying that certain regions in the CuO_2 plane are close to being undoped. Such regions may behave as free-spin like entities which enhance $^{17}1/T_1T^c$ for neighboring sites.

We also note that the onset of wipeout T_{NQR} sets in below T_{scale}. In the case of $x = 0.035$, $T_{NQR} \simeq T_{scale}$, which suggests that both may be related. Indeed, we observe that the lower half limit $^{17}x_{local} = 0.016$ for $x = 0.035$ at 295 K, which suggests that a growing number of low doped patches exist with enhanced values of $^{63}1/T_1$. In the case of ^{63}Cu discussed in chapter 1, $^{63}1/T_1$ is so much enhanced that the ^{63}Cu signal is no longer measurable, i.e. is wiped-out.

Chapter 6

Conclusions

The nature of the inhomogeneity in $La_{2-x}Sr_xCuO_4$ (and related materials) has been a major mystery in the NMR/NQR community since its discovery in the 1980's. Such unanswered phenomena include the nature of the ^{17}O NMR linebroadening which shows an inconsistent temperature dependence to a local moments type picture for the inhomogeneity. Another is the unusually large ^{63}Cu NQR linebroadening and the nature of the "B"-line. Yet another is the nature of the tailed ^{63}Cu wipeout in the region $x < 1/8$. In light of these unresolved issues, we undertook a detailed systematic study of the inhomogeneity in the CuO_2 planes of $La_{2-x}Sr_xCuO_4$ in order to unravel these mysteries. We present these revealing studies in this thesis.

Using ^{63}Cu NQR and ^{17}O NMR in high-quality poly- and single crystal samples, we discovered that the inhomogeneity takes the form of a thermodynamic spatial variation in electronic states over short $\sim 6-8$ nm length scales. We characterized the spatial variation in terms of the local hole concentration $x_{local}(\neq x)$ which was shown to deviate from nominal x at elevated temperatures as high as 500-600 K. The extent or amplitude, Δx_{local}, of the spatial variation (where $x_{local} = x \pm \Delta x_{local}$) was found to increase with decreasing temperatures below 500-600 K, and reached values as large as $\Delta x_{local}/x = 0.4$-0.5 in the temperature range ≥ 100 K. The length scale over which x_{local} modulates in the CuO_2 planes was found to be $2R_{patch} \simeq 6-8$ nm which we deduced using a patch-by-patch model for x_{local} together with alloying effects in the lattice. Such short length scales explains why scattering techniques

(which detect coherent phenomena average over length scales larger than ten's of nm's) tend to underestimate Δx_{local}. Our use of the *local* nature of the NMR/NQR probes proved to be essential in our study of the inhomogeneity, and furthermore, our use of high-quality single crystals and poly-crystalline samples showed that x_{local} was a sample independent phenomenon, therefore the inhomogeneities reported in this thesis are *intrinsic* to the CuO_2 planes of $La_{2-x}Sr_xCuO_4$.

By taking alloying effects into account in a novel way, we once and for all clarified the nature of the ^{63}Cu "B"-line. We presented a point charge calculation which incorporated the random positioning of $^{+2}$Sr donor ions in the lattice, and we successfully reproduced the entire ^{63}Cu NQR spectrum including "B"-line, with one free parameter ($^{63}R_{patch}$). In particular, we showed that the "B"-line corresponds to ^{63}Cu nuclei with a $^{+2}$Sr ion directly above or below it. $^{63}R_{patch}$ (and $^{17}R_{patch} \sim^{63} R_{patch}$) were deduced assuming no clustering of the $^{+2}$Sr ions in the lattice beyond probability theory, however, we note that even in the case of clustering over very short length scales 3-4 nm, the presence of a short length scale is still needed to account for the observed spatial variation in electronic states. Using the temperature dependence of the ^{63}Cu NQR spectrum, we also deduced the temperature dependence of the local orthorhombic distortions which were found to start at temperatures ($T_Q \gtrsim 400$ K) above LRO in the case of $x > 0.04$. Comparison between the local orthorhombic distortions and LRO implied a mixture of order-disorder and displacive type structural transitions in the region $x > 0.04$ and $T < T_Q$.

We also showed that the ^{17}O NMR linebroadening is dominated by spatial variations in the spin susceptibility through the spatial variation $^{17}x_{local}$ by showing for the first time that the same empirical scaling relation holds across the inhomogeneous linebroadening of *each* crystal. This rules out the possibility that impurity or "dirt" effects are the dominant cause of the ^{17}O NMR linebroadening, commonly beleived to be the case in $La_{2-x}Sr_xCuO_4$. Rather, we showed that the temperature dependence of the ^{17}O NMR linebroadening is a result of the growing amplitude $^{17}\Delta x_{local}$ of the spatial variation in electronic states.

The mysterious nature of the tailed wipeout for $x < 1/8$ in the temperature

region $T_{NQR}^{inflect} < T < T_{NQR}$ (chapter 1) can naturally be accounted for in light of our results of the inhomogeneity. Note that in the temperature region $T_{NQR} \sim 300$ K for $x = 0.04$, the characteristic local hole concentration ${}^{63}x_{local}$ for insulating patches is inferred at the lower half intensity to be as low as ${}^{63}x_{local} \sim 0.015$ (Fig. 3-7). Likewise, ${}^{17}x_{local} \sim 0.016$ (Fig. 5-7) for $x = 0.035$ in the temperature region $T_{NQR} \sim T_{scale}$. Recall that ${}^{63}1/T_1$ for $x = 0.02$ at ~ 300 K is already too large for the Cu signal to be observable, therefore the insulating patches for $x = 0.04$ at 300 K are wiped-out. As one cools the $x = 0.04$ sample below 300 K, there are a growing number of patches with lower and lower hole concentration which are also wiped-out, leading to an overall increase in the wipeout fraction $F(T)$ with decreasing temperature. The fact that ${}^{63}x_{local}$ (and ${}^{17}x_{local}$) gradually fan out with decreasing temperature therefore explains the tailed temperature dependence of the wipeout fraction $F(T)$ in the region $T_{NQR}^{inflect} < T < T_{NQR}$ for $x < 1/8$.

Appendix A

^{63}Cu Anti-shielding factors

We now deduce the anit-shielding factors [81] $\zeta_{latt}^{(A,B)}$ and $\zeta_{3d}^{(A,B)}$ for the A and B-sites respectively. We first assume that all anit-shielding factors are isotropic and independent of x and T, but are allowed to vary between the A and B-lines. Next, we produce a cross-plot shown in Fig. A-1(a) of the resonance frequency at the CG of the A-line $\left\langle {}^{63}\nu_Q^A \right\rangle (x,T)$ (Fig. 3-9(a)) and the EFG at the CG of the simulation $\left\langle V_{latt}^{c,A} \right\rangle (x,T)$ for the A-line (Fig. 4-2). Likewise, we produce the same cross-plot for the B-line shown Fig. A-1(b). Note that we only use data in temperature region above T_Q in Fig. 3-9 where local orthorhombic distortions are absent.

Then we deduce the linear fit using the standard empirical form [69, 76]:

$$\left\langle {}^{63}\nu_Q^k \right\rangle = \Lambda_{3d}^k - \Lambda_{latt}^k \left\langle V_{latt}^{c,k} \right\rangle \tag{A.1}$$

where $k = (A,B)$ and all quantities are overall positive. The best fit to the data shown by the solid black lines in Fig. A-1 indicates that for the A-line $\Lambda_{3d}^A = 75.3$ MHz and $\Lambda_{latt}^A = 16.0$ MHz/[emu$\times 10^{-14}$], and correspondingly for the B-line that $\Lambda_{3d}^B = 64.6$ MHz and $\Lambda_{latt}^B = 10.7$ MHz/[emu$\times 10^{-14}$].

Using Eq.'s (2.7), (4.2) and (4.3), we express the Λ's in terms of the unknown anti-shielding factors as such

$$\Lambda_{3d}^k = \frac{4e^2|^{63}Q|}{14h}(1-4f_\sigma^o)\left\langle r_{3d}^{-3} \right\rangle \cdot \zeta_{3d}^k$$

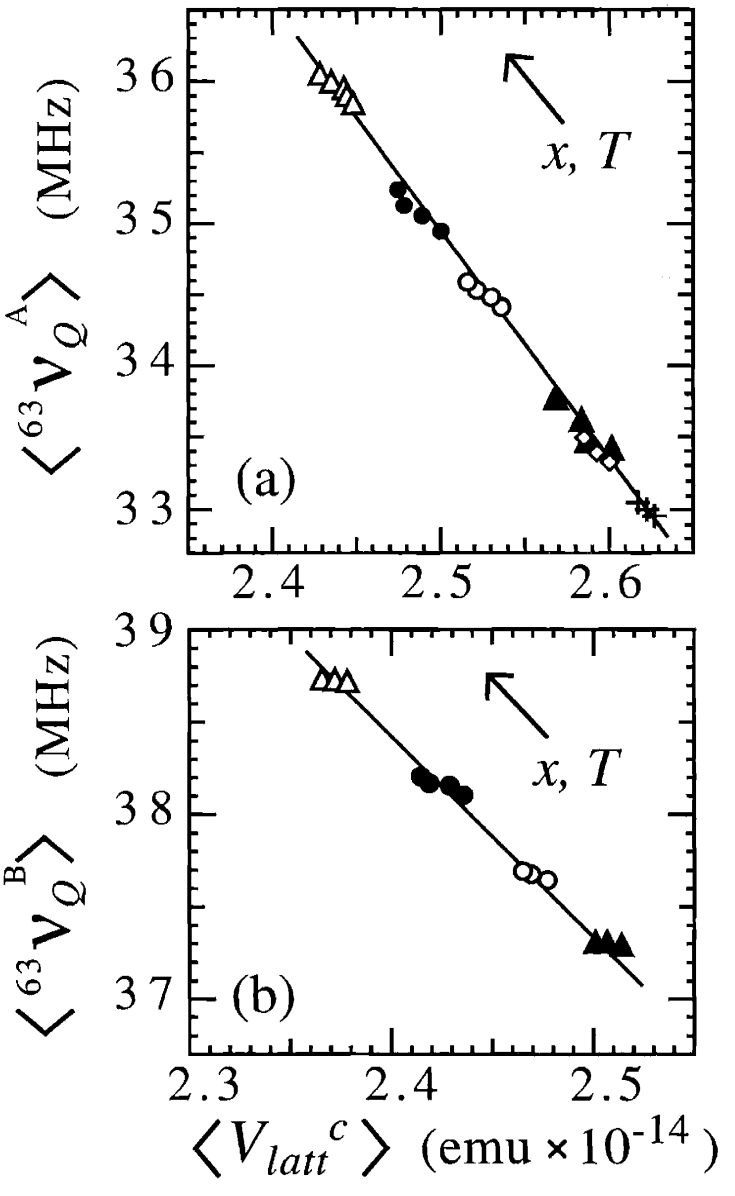

Figure A-1: Cross-plot of (a) $\langle {}^{63}\nu_Q^A \rangle$ taken from Fig. 3-9(a) and the EFG at CG $\left\langle V_{latt}^{c,A} \right\rangle$ shown in Fig. 4-2 with x and T as implicit parameters. (b) Same cross-plot as (a) but for the B-line.

$$\Lambda^k_{latt} = \frac{e|^{63}Q|}{2h} \cdot \zeta^k_{latt} \tag{A.2}$$

Using $f^o_\sigma = 0.076$ [80] , $^{63}Q = -0.16$ barns [2], and the bare value $< r^{-3}_{3d} >= 7.5$ a.u. [2] for free cupric ions, we find that for the A-line $\zeta^A_{latt} = 27.7$ and $\zeta^A_{3d} = 0.93$, while for the B-line $\zeta^B_{latt} = 18.6$ and $\zeta^B_{3d} = 0.82$. These set of results are consistent with previous estimates [69, 76].

Converting the above analysis using $^{63}Q = -0.211$ barns [84] instead of $^{63}Q = -0.16$ barns [2] results in a uniform 24.2 % decrease in our estimates of the ζ's. However, note that what really matters in converting from calculation to experiment are the Λ's in Eq. (A.1). Likewise, when accounting for the broadening in section to deduce $^{63}\Delta x_{patch}$, it is also the Λ's which ultimately matter, not the ζ's, therefore our end result for $^{63}\Delta x_{patch}$ and $^{63}R_{patch}$ are independent of what value of ^{63}Q we use.

Appendix B

$^{63}1/T_1$ Recovery

In this appendix we analyze the multiple exponential recovery of the magnetization $M(t)$ in the case of $x = 0.16$ at $T = 100$ K and deduce the distribution in $^{63}1/T_1$ at a fixed frequency. We also show that the distribution in $^{63}1/T_1$ at a fixed frequency can be naturally accounted for by a finite intrinsic lattice broadening whose *HWHM* $^{63}\Delta\nu_{latt}^{T1}$ we calculate using the recoveries $M(t)$. We find that $\Delta\nu_{latt}^{T1} = 0.62 \pm 0.09$ MHz is consistent with the independent point charge calculation $\Delta\nu_{latt} = 0.49$ MHz for $x = 0.16$ shown in chapter 4.

When there is no distribution in $^{63}1/T_1$, the experimentally observed nuclear recovery $M(t)$ may be fit to Eq. (2.17) where $M(0)$, $M(\infty)$ and $^{63}1/T_1$ are free parameters of the fit. In Fig. B-1 the fit is presented in normalized form $I(t)$, defined as

$$I(t) = \frac{M(t) - M(\infty)}{M(0) - M(\infty)} \tag{B.1}$$

for $x = 0.0$ at 475 K at various positions across the NQR spectrum including the center $^{63}1/T_{1,A}^{(0)}$, upper half intensity $^{63}1/T_{1,A}^{(+)}$ and lower half intensity $^{63}1/T_{1,A}^{(-)}$ positions. As discussed earlier, the $x = 0.0$ spectrum is homogeneously broadened and therefore shows no frequency dependence of $^{63}1/T_1$ across its lineshape, nor does it show any sign of having a multiple exponential recovery. We also note that the data in Fig. B-1 is taken at 475 K which is the orthorhombic phase, therefore we can also rule out the possibility that the orthorhombic distortions are the *direct* cause of observed

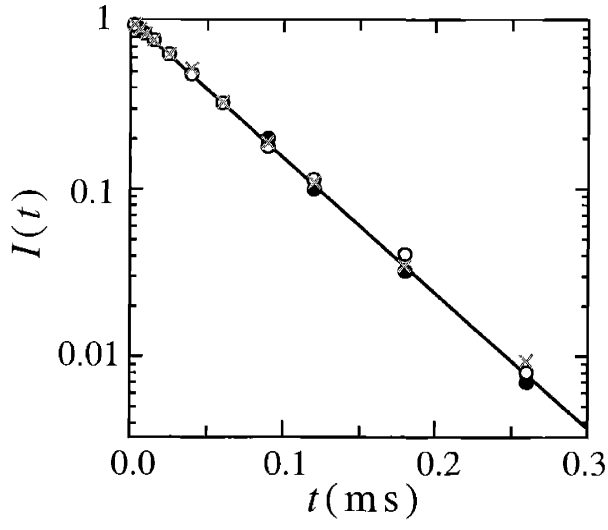

Figure B-1: Time dependence of bare recovery $I(t)$ deduced from magnetisation $M(t)$ (see Eq. (B.1) for $x = 0.0$ at 475 K.

frequency dependence in $^{63}1/T_1$ for $x \geq 0.0$.

In Fig. B-2 we show the bare recovery $I(t)$ at similar positions across the A-line of $x = 0.16$ at 100 K. There are two noticable features about the recoveries in Fig. B-2. Firstly, the slopes get steeper towards lower frequency, which corresponds to the fact that the $^{63}1/T_{1,A}^{(-)} >^{63} 1/T_{1,A}^{(0)} >^{63} 1/T_{1,A}^{(+)}$. Secondly, the solid straight lines which correspond to force fitting the recoveries $I(t)$ to a single value of $^{63}1/T_1$ does not result in the best fit. This implies that there are multiple exponential components to $I(t)$ of the form

$$I(t) = \frac{\sum_j a_j \exp\left(-\frac{3}{T_{1,j}}t\right)}{\sum_j a_j} \tag{B.2}$$

Fitting the recoveries to a single exponential form is equivalent to taking a_j =1 and $1/T_{1,j} = 1/T_1$ in Eq. (B.2), and results in the force fit values $^{63}1/T_{1,A}^{(-)}$, $^{63}1/T_{1,A}^{(0)}$ and $^{63}1/T_{1,A}^{(+)}$ shown across the NQR spectrum in Fig. B-3.

The dashed lines in Fig. B-2 show the best fit result from a sum of exponentials $1/T_{1,j}$ whose distribution coefficients a_j are presented as the dashed lines in Fig. B-4. The distribution coefficients a_j for each recovery $I(t)$ are determined using three free

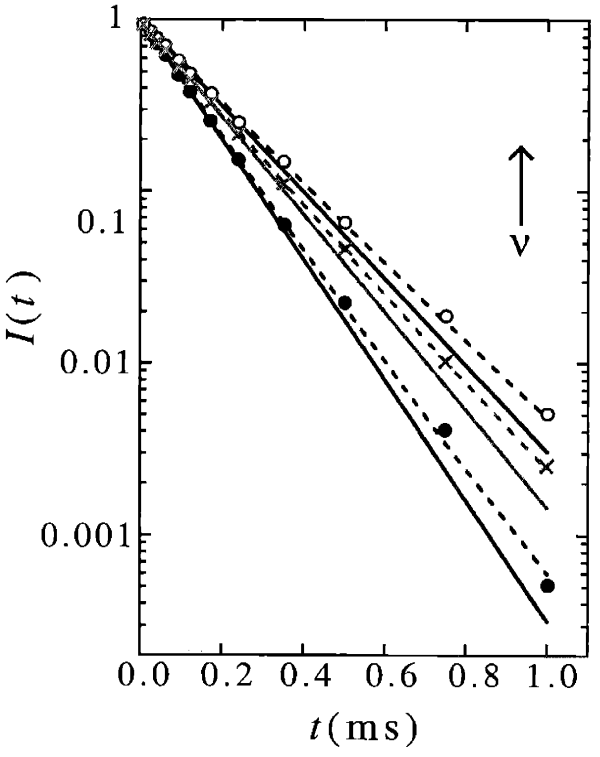

Figure B-2: $x = 0.16$ at 100 K, taken at various positions across NQR spectrum including $^{63}1/T_{1,A}^{(0)}$ (grey $\times$), $^{63}1/T_{1,A}^{(+)}$ ($\circ$) and $^{63}1/T_{1,A}^{(-)}$ ($\bullet$). Solid lines are force fits using a single exponential recovery while dashed lines are best fits using multiple exponential recoveries shown in Fig. B-4.

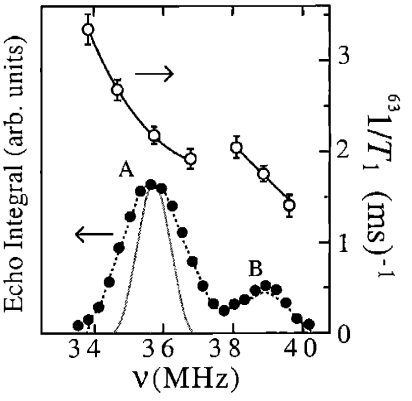

Figure B-3: ^{63}Cu NQR spectrum of $x = 0.16$ at 100 K (•) along with force fit values $^{63}1/T_1$ (○) at various positions across the line. Dashed black line through (•) shows fit using patch-by-patch model with a lower bound for the patch radius of $^{63}R_{patch} = 2.7 \pm 0.2$ nm, while gray curve illustrates relative size of intrinsic *HWHM* $\Delta\nu_{latt}^{T1} = 0.62$ MHz deduced from recoveries in Fig. B-2. Solid curves are interpolations between data points (○).

parameters and one constraint. The 3 free parameters can be expressed as such:

$$a_j^{(-)} = \exp\left(-\frac{(P_{T1} - 1/T_{1,j})^2}{(\Delta_P^{(-)})^2}\right) \tag{B.3}$$

$$a_j^{(+)} = \exp\left(-\frac{(P_{T1} - 1/T_{1,j})^2}{(\Delta_P^{(+)})^2}\right) \tag{B.4}$$

where Eq. (B.3) is used for $1/T_{1,j} < P_{T1}$ and Eq. (B.4) is used for $1/T_{1,j} > P_{T1}$. The three free parameters are the peak of the distribution P_{T1}, the width $\Delta_P^{(-)}$ for $1/T_{1,j} < P_{T1}$ and the width $\Delta_P^{(+)}$ for $1/T_{1,j} > P_{T1}$. The constraint is that the CG of the distribution, shown as the solid vertical lines in Fig. B-4, coincide with the force fit value $^{63}1/T_{1,A}$ deduced with a single exponential fit to the recovery shown across the NQR spectrum in Fig. B-3.

Using second moment analysis of the distributions in Fig. B-4 in an analogous manner to Eq. (3.2) and Eq. (4.17), we determine that the effective *HWHM* of the distributions to be $\Delta 1/T_{1,A}^{(-)} = 0.33$ (ms^{-1}), $\Delta 1/T_{1,A}^{(0)} = 0.27$ (ms^{-1}) and $\Delta 1/T_{1,A}^{(+)} = 0.20$ (ms^{-1}). Note that these *HWHM* of the distributions are only $\sim$ 15 % of the

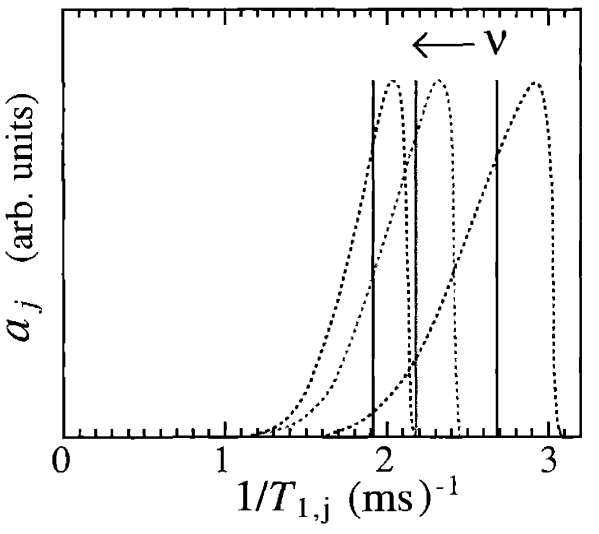

Figure B-4: Distribution coefficients a_j of $1/T_{1,j}$ (dahsed lines) deduced from best fit to recoveries $I(t)$ shown in Fig. B-2 for $x = 0.16$ at 100 K. Solid vertical lines show both force fit values $^{63}1/T_{1,A}^{(-)}$ $^{63}1/T_{1,A}^{(0)}$ (grey line) and $^{63}1/T_{1,A}^{(+)}$ in order of increasing frequency shown by arrow which coincide with CG of distributions.

value at the CG $^{63}1/T_{1,A}$, which implies that accurate recovery data $I(t)$ is needed down to $I(t) \sim 0.001$.

We can now get an estimate of the underlying intrinsic lattice broadening $\Delta\nu_{latt}^{T1}$ by converting the HWHM $\Delta 1/T_{1,A}$ deduced above into equivalent frequency widths. In order to do so we take a local derivative β_ν of the underlying frequency dependence of $^{63}1/T_{1,A}$ at a frequency ν defined as such

$$\beta^\nu = \left| \frac{\delta 1/T_{1,A}}{\delta \nu} \right| \tag{B.5}$$

where $1/T_{1,A}$ is the interpolated value of $^{63}1/T_{1,A}$ shown in Fig. 2-1 as the solid line. Using units of $^{63}1/T_{1,A}$ in (ms^{-1}) and ν in (MHz), we find that $\beta^{(-)} = 0.62$, $\beta^{(0)} = 0.39$, and $\beta^{(+)} = 0.29$, from which we deduce the HWHM (in units of MHz) as such

$$\Delta\nu_{latt}^{(-)} = \Delta 1/T_{1,A}^{(-)}/\beta^{(-)} = 0.53$$

$$\begin{aligned}\Delta\nu_{latt}^{(0)} &= \Delta 1/T_{1,A}^{(0)}/\beta^{(0)} = 0.69 \\ \Delta\nu_{latt}^{(+)} &= \Delta 1/T_{1,A}^{(+)}/\beta^{(+)} = 0.68 \end{aligned} \tag{B.6}$$

at the lower half intensity, center and upper half intensity of the spectrum respectively. Finally, we deduce the average value $\Delta\nu_{latt}^{T1}$ of the three estimates in Eq. (B.6) to be $\Delta\nu_{latt}^{T1} = 0.62 \pm 0.09$ MHz. This is consistent with $\Delta\nu_{latt} = 0.49$ MHz deduced independently using the point charge calculation shown in Fig. 4-7. We illustrate the size of $\Delta\nu_{latt}^{T1}$ in Fig. B-3 as the dashed gray curve and also in Fig. 4-7 and Fig. 4-8.

Note that $\Delta\nu_{latt}^{T1}$ is $\sim$ 25 % overestimated compared with the calculated point charge value $\Delta\nu_{latt}$. However, in order to obtain $\Delta\nu_{latt}^{T1}$ beyond the accuracy we have outlined, one needs to know the underlying distribution in $1/T_{1,A}$ beforehand. This is due to the fact that we have used finite $\tau = 12\mu$s conditions throughout this analysis. In the case where $1/T_{1,A}$ is distributed, using finite $\tau(> 0)$ conditions will suppress the faster components of $1/T_{1,A}$ at fixed frequency. Using a finite τ results in a smaller contribution from Cu nuclei with large spin-spin relaxation rates $^{63}1/T_2(>^{63} 1/T_1)$ which have correspondingly large values of $^{63}1/T_1$. Therefore, the CG of $^{63}1/T_1$ will be underestimated from the true CG measured in hypothetical $\tau = 0$ conditions. The underestimation of the CG will be more severe towards lower frequencies were $1/T_{1,A}$ gets faster overall. This implies that our derivation of β_ν will be underestimated by using finite τ, therefore $\Delta\nu_{latt}^{T1}$ in Eq. (B.6) will be overestimated. On the other hand, using $\tau = 12\mu$s conditions will also underestimate the width $\Delta 1/T_{1,A}$ in Eq. (B.6) on the faster side, therefore $\Delta\nu_{latt}^{T1}$ will be underestimated. We note that even in $\tau = 12\mu$s conditions, however, we obtain a consistent value with our independent point charge calculation.

Appendix C

The NQR/NMR probe

In this appendix we describe a few experimental aspects of the NQR/NMR probe and its resonance circuit (Fig. 2-8). The art of the NQR/NMR experiment comes down to having a good probe. The NQR/NMR probe is the most important and challenging part of the spectrometer and is the predominant factor in achieving good signal-to-noise ratio (S/N) and temperature stability. It must also be carefully designed to avoid arcing of the high power ($\sim$ 1 kW) r.f. input to ground.

A more detailed version of the resonance circuit diagram is shown in Fig. C-1. It includes the variable matching capacitor C_M, the variable tuning capacitor C_T, the sample and coil inductance L, and the parallel resistance R. C_M, C_M, L, and R represent real physical components of the probe, i.e. they are each soldered into the resonance circuit at the tip of the probe. In practice, however, all four of these physical components each come with a resistance, a capacitance and an inductance. For instance, the coil and sample have a large inductance L together with a small resistance r and a small stray capacitance. The trick in building an NQR/NMR probe is to limit the unwanted effects in each circuit component.

For instance, it is important to avoid any stray inductance in the probe which can potentially decrease the filling factor η_f. η_f defined as such

$$\eta_f = \frac{\frac{1}{8\pi}\int^{sample} \mathbf{H_1} \cdot \mathbf{B_1} d\mathbf{r}}{\frac{1}{8\pi}\int^{all-space} \mathbf{H_1} \cdot \mathbf{B_1} d\mathbf{r}} \tag{C.1}$$

where B_1 and H_1 ($\sim$ 10 G) are the amplitudes of the r.f. magnetic flux density and r.f. magnetic field strength, respectively. Eq. (C.1) represents the ratio of the magnetic energy in the volume of the sample to the magnetic energy in all space. A low filling factor ($\eta_f \ll 1$) leads to lower S/N.

It is also important to avoid any stray capacitance in the probe since this limits the tuning range of the probe. A typical tuning range we achieved for NQR was 26 MHz $\leftrightarrow$ 42 MHz (i.e. a range of $1 \leftrightarrow 1.6$), which was more than sufficient to cover a whole spectrum without having to change the coil. The tuning range was temperature independent except when the probe was submersed in liquid N_2, in which case the tuning range uniformly decreased $10 - 20$ %.

C.1 Q–factor

One important quantity which characterizes many aspects of the NQR/NMR probe is its quality factor Q. There are various equivalent definitions of Q [9]. One definition is given by

$$Q = \frac{\omega_n}{2\delta\omega} = \frac{f_n}{2\delta f} \tag{C.2}$$

where $\omega_n = 2\pi f_n$ is the resonance frequency, and δf is the half width of the response of the probe. In other words, if one tunes the capacitors in the probe to resonate at f_n, and then one switches the r.f. input to $f_n + \delta f$ without re-tuning, only half of the r.f. power will reach the sample. For ^{63}Cu NQR, $Q = 50 - 60$, which implies that in order to take a lineshape measurement, one must re-tune the capacitors every $\sim$ 100 kHz across the line, i.e. at each data point. One can measure Q by applying an r.f. pulse and looking at the oscillating decay from the probe right after the excitation pulse. One then measures τ_e on the oscilloscope by measuring the time it takes the amplitude of the oscillating voltage to decay by a factor $\frac{1}{e} \simeq 0.368$. Q is then given by

$$Q = \pi\tau_e f_n \tag{C.3}$$

The S/N of the probe depends on many factors, including Q, η_f, and f_n. The

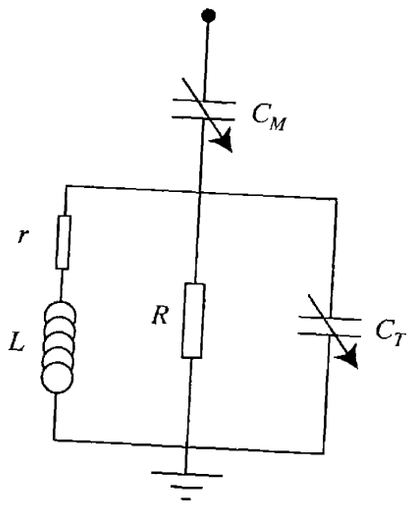

Figure C-1: The NQR/NMR parallel tuned circuit including the the variable matching capacitor C_M, the variable tuning capacitor C_T, the sample and coil inductance L, and the parallel resistance R. Also shown is the effective coil resistance r used in the circuit theory.

total S/N can be empirically expressed as such

$$S/N \sim \frac{f_n}{T} f_n^{\alpha} \eta_f^{\beta} Q^{\gamma} \tag{C.4}$$

The factor f_n/T arises from the thermal nuclear population difference between nuclear eigenstates. $hf_n/k_BT \sim 10^{-5}$ at 100 K, which implies that we are effectively measuring only $\sim 10^{-5}$ of the total nuclear population at 100 K. f_n^{α} arises from Faraday's law of induction, where $\alpha = 1$ in the limit of prefect filling (i.e. $\eta_f = 1$). Typically however, $1/2 < \alpha < 1$. Similarly, experience suggests that $1/2 < \beta < 1$ and $1/2 < \gamma < 1$.

Eq. (C.4) suggests that the higher the Q, the larger the S/N. On the other hand, Eq. (C.3) suggests that the higher the Q, the longer it takes for the ring-down (Fig. 2-6) to decay, i.e. τ_e is larger, which can sometimes be problematic. Most of the ring-down is subtracted by phase-cycling (chapter 2.3), however, any small inefficiencies in the phase cycling are amplified by the shear magnitude of the peak voltage of the

r.f. pulses ($\sim$ 100 V), which can potentially obscure the spin echo signal ($\sim 1\mu$V). Realistically, phase-cycling is never perfect, therefore every probe has a "dead-time" after the application of an r.f. pulse. In the case of $Q \sim 50$, a typical dead-time is $\sim 6\mu$s. For these reasons the shortest τ we use is $\tau \sim 12\mu$s. Choosing the right Q therefore involves a compensation between S/N and ring-down.

Q also determines the amplitude of the r.f. power H_1 in the coil. According to [81]

$$H_1 = \sqrt{\frac{10\eta_f Q P_c}{V f_n}} \tag{C.5}$$

for H_1 in Gauss and f_n in MHz. V is the volume of the coil (in cm^3), and P_c (in W) is the total power into the probe from the Kalmus amplifier (Fig. 2-8).

C.2 Circuit Theory

One way to reduce Q is to add a resistor R in parallel (Fig. C-1). Choosing a small value of R has the effect of damping the circuit, or decreasing Q. In order to understand this, it is useful to derive a back-of-the-envelope type calculation for the response of the tuned circuit (Fig. C-1). In order to do so, we introduce a small *effective* resistance r for the resistance of the coil. Following standard circuit theory [9], one can then derive the input impedance $\mathbf{Z}$ of the tuned circuit as such

$$\mathbf{Z}(\omega) = (i\omega C_M)^{-1} + \left[R^{-1} + i\omega C_T + (i\omega L + r)^{-1}\right]^{-1} \tag{C.6}$$

which one then equates to the resonance condition

$$\mathbf{Z}(\omega_n) = Z_0 + 0i \tag{C.7}$$

In an experiment, the resonance condition (Eq. (C.7)) is achieved by optimizing C_M and C_T using a magic-tee [23] at the desired resonance frequency ω_n. By rearranging Eq. (C.6), the imaginary parts of Eq. (C.7) and Eq. (C.6) are used to find an theoretical expression for the resonance frequency ω_n as a function of the circuit

components (assuming $Q \gg 1$ and $\omega L \gg r$) as such [9, 23]

$$\omega_n = \sqrt{\frac{1}{L\left(C_M + C_T\right)}} \cdot \left(1 - O\left(Q^{-2}\right)\right) \tag{C.8}$$

up to order $Q^{-2}(\ll 1)$. The theoretical expression for Q is derived below. The real parts of Eq. (C.7) and Eq. (C.6) define the matching condition which effectively matches the input impedance of the tuned circuit to the impedance of the co-axial cables, which in our case is $Z_0 = 50\ \Omega$.

The next step is to derive an expression for Q. In order to do so, one expands the impedance $\mathbf{Z}$ in Eq. (C.6) around the resonance frequency $\omega = \omega_n + \delta\omega$ [9] to get

$$\mathbf{Z}\left(\omega_n + \delta\omega\right) = Z_0\left(1 + 2iQ \cdot \frac{\delta\omega}{\omega_n}\right) \tag{C.9}$$

In the limit $Q \gg 1$ this leads to

$$\frac{1}{Q} = \frac{\omega_n L}{R} + \frac{r}{\omega_n L} \tag{C.10}$$

One can see in Eq. (C.10) that decreasing R (or damping) has the effect of decreasing Q. The advantage of introducing R into the circuit is that Q is no longer dominated by r. In general, r is temperature dependent while the resistors R that we use are temperature independent. Therefore, introducing R into the circuit drastically reduces the temperature dependence of Q. Any temperature dependence in Q would effect the S/N (Eq. C.4) which is not good for measuring absolute signal intensity, i.e. wipeout. If H_1 has temperature dependence through Q, then the length of the r.f. pulses (Eq. (2.18)) would have to be determined at each temperature. For these reasons, we typically add $R \sim 20\ \mathrm{k}\Omega$.

Another consequence of the circuit theory is a closed form expression for the values of C_M and C_T at resonance

$$C_M = \sqrt{\frac{1}{Z_0 Q L \omega_n^3}}$$

$$C_T = \frac{1}{L\omega_n^2} - \sqrt{\frac{1}{Z_0 Q L \omega_n^3}} \tag{C.11}$$

assuming $Q \gg 1$. We can test whether our simple circuit theory is correct by comparing the theoretical estimates of Q, C_M, and C_T in Eq. (C.10) and Eq. (C.11) with experiment. In order to do so we substitute reasonable values for f_n, L, R, and r into Eq. (C.10) and Eq. (C.11). Let us take a standard ^{63}Cu NQR experiment as an example. We can estimate the inductance L by [23]

$$L = \frac{N^2 a^2}{23a + 25b} \tag{C.12}$$

for L in μH. N is the number of turns in the coil, a is the coil radius (cm) and b is the coil length (cm). Using Eq. (C.12) we can deduce that typically $L \sim 1\mu$H for ^{63}Cu NQR. r is typically $r \sim 1\ \Omega$ at 295 K, and we usually take $R = 20$ kΩ. According to Eq. (C.2) for $\omega_n/2\pi \sim 40$ MHz, we then deduce that $Q \sim 60$, which is very close to the experimental value of $Q = 50 - 60$ determined using Eq. (C.3). Furthermore, Eq. (C.10) predicts that the r dependent term in Q is small ($\sim$25 %), which significantly reduces any temperature dependence in Q. Using the same input values for f_n, L, R, and r, Eq. (C.11) predicts that $C_M \sim 4.6$ pF, while $C_T \sim 11.2$ pF. These are reasonable estimates compared to the ranges $C_M = 1 - 5$ pF and $C_T = 1 - 10$ pF of the capacitors used in the experiment, bearing in mind that both C_M and C_T are uniformly increased by stray capacitances in the circuit.

Appendix D

Scaling phenomenon

For a Fermi-liquid without strong magnetic correlations, there exists a universal relation between the spin portion of the Knight-shift K_{spin} and $1/T_1T$. This relation, known as the Korringa law, takes on the form [42,81]

$$\frac{1}{T_1T} = SK_{spin}^2 \tag{D.1}$$

The functional form of Eq. (D.1) can be understood using a density of states $N(\epsilon_F)$ argument [42,81] where $1/T_1T \propto N(\epsilon_F)^2$ and $K_{spin} \propto N(\epsilon_F)$, leading directly to Eq. (D.1). As initially proposed by M. Takigawa *et al.* [91], however, the above Korringa relation does *not* hold in $YBa_2Cu_3O_y$. Rather, the ^{17}O NMR data for c-axis aligned powder strongly suggests the functional form in Eq. (5.7) with a T independent slope $\beta^{(CG)} \sim 2.0 \pm 0.2(\text{sK}\%)^{-1}$ in the case of $YBa_2Cu_3O_{6.6}$ [91] and $\beta^{(CG)} \sim 2.2 \pm 0.3(\text{sK}\%)^{-1}$ in the case of $YBa_2Cu_3O_7$ [91]. Further support for the scaling relation in Eq. (5.7) is evidenced by ^{89}Y NMR data in this system. The hyperfine form factor $^{89}A(\mathbf{q})$ decreases even more rapidly $\sim (\mathbf{q} - \mathbf{Q_{AF}})^4$ than $^{17}A(\mathbf{q})$ for $\mathbf{q} \approx \mathbf{Q_{AF}}$, therefore a similar scaling relationship should hold, as is indeed observed [3,91]. As shown in chapter 5, the scaling from in Eq. (5.7) for $La_{2-x}Sr_xCuO_4$ holds across the inhomogeneous ^{17}O NMR linebroadening as a function x (Fig. 5-1) and T (Fig. 5-2), and also at the CG of the spectrum as a fucntion of x and T (Fig. 5-12), all with comparable values of $\beta \simeq 2.4 \pm 0.2$ $(\text{sK}\%)^{-1}$.

As shown in Fig. 5-1 and Fig. 5-12, our results for the $La_{2-x}Sr_xCuO_4$ system are clearly consistent with Eq. (5.7) and not Eq. (D.1). We explicitly show the failure of Eq. (D.1) in Fig. 5-12 as the dashed grey line which corresponds to an enhanced value of $S = 4S_0$ over the free electron value S_0 for ^{17}O. Instead we find a constant slope $\beta^{(CG)} = 2.5 \pm 0.2(\text{sK\%})^{-1}$ from Fig. 5-12 over the wide range $0.035 \leq x \leq 0.15$ and $T_{scale} \leq T \leq 475$ K, and furthermore $\beta = 2.4 \pm 0.2(\text{sK\%})^{-1}$ over the inhomogeneous linebroadening in Fig. 5-1 and $\beta' = 2.2 \pm 0.3(\text{sK\%})^{-1}$ in Fig. 5-2. These results are consistent with $YBa_2Cu_3O_y$ [91], and moreover the values for all the slopes β agree to within ± 15 %.

The same observations for scaling were also reached in earlier reports for c-axis aligned $La_{1.85}Sr_{0.15}CuO_4$ powder [43], where $\beta^{pwd} = 1.4 \pm 0.1(\text{sK\%})^{-1}$ was deduced, which is somewhat smaller that our $\beta^{(CG)} = 2.5 \pm 0.2$ $(\text{sK\%})^{-1}$. We attribute the difference to the more accurate single crystal data which does not suffer the overlap with the apical oxygen site.

In order to account for the scaling relation in Eq. (5.7), one can employ the phenomenological approach used by M.M.P. [58,59] where they assume the dynamic susceptibilty in the low energy $\frac{\hbar}{k_B}\omega_0 \sim 2$ mK $\ll T$ regime consist of two parts

$$\frac{\chi''(\mathbf{q},\omega_0)}{\omega_0} = c_0\frac{\chi'}{\Gamma_B} + c_{AF}\frac{\chi'_{AF}(\mathbf{q})}{\Gamma_{AF}(\mathbf{q})} \tag{D.2}$$

where χ' is the $\mathbf{q}$ *independent* susceptibilty, Γ_B is the band-width parameter we shall derive, and c_0 and c_{AF} are dimensionless constants which depend on the particulat

The functional form in Eq. (D.2) can be used to account for both NMR and neutron scattering results while maintaining a one-component model for the spin fluid. Since both NMR and neutron scattering probe the spin susceptibilty, it was expected that $^{17}1/T_1T$ should be influenced by the substantial incommensurability [54] found in the spin fluctuations of $La_{1.86}Sr_{0.14}CuO_4$. However, the temperature dependence and magnitude of $^{17}1/T_1T$ in $La_{2-x}Sr_xCuO_4$ do not reflect the incommensurability [43], but instead, are similar to $^{17}1/T_1T$ in $YBa_2Cu_3O_y$ with similar transfer hyperfine coupling constants (Eq. (2.24)). The NMR and neutron scattering experiments are

consistent within a one-component model provided the phenomenological approach in Eq. (D.2) is used. The dynamic susceptibilty in Eq. (D.2) consists of an enhanced AF spin fluctuation term $\chi'_{AF}(\mathbf{q})$ which is peaked around $\mathbf{q}$=$\mathbf{Q}_{AF}$ and dominates the the Cu relaxation rate ${}^{63}1/T_1T$. The O relaxation rate ${}^{17}1/T_1T$ on the other hand, filters out $\chi'_{AF}(\mathbf{q})$ by the $\mathbf{q}$ dependence in the hyperfine form factor in Eq. (2.23), and therefore is dominated by the q independent susceptibilty χ'.

For c-axis alignment, according to Eq. (2.13), Eq. (D.2), and Eq. (2.15) we are then left with a modified expression

$$ {}^{17}\frac{1}{T_1T}_c = \frac{{}^{17}\gamma_n^2 k_B}{\mu_B^2} \sum_{\mathbf{q},\alpha=(//,\perp)} \left|{}^{17}A(\mathbf{q})^\alpha\right|^2 c_0 \frac{\chi'_\alpha}{\Gamma_B} \tag{D.3} $$

We can then convert Eq. (D.3) to the form in Eq. (5.7) by using Eq. (5.3) as such

$$ {}^{17}\frac{1}{T_1T}_c = \left[\frac{{}^{17}\gamma_n^2 k_B}{\mu_B} \frac{g_{ab}^2\left(C_\perp^2 + C_{//}^2\right)}{g_c^2 C_c} \cdot \frac{c_0}{\Gamma_B}\right] {}^{17}K^c_{spin} \tag{D.4} $$

where the expression in brackets is the experimentally determined β in Eq. (5.7), from which we determine the T and x independent energy scale $\hbar\Gamma_B = c_0 \cdot 75$ meV, within the model dependent constant c_0.

Our Γ can be compared with previous results for powder aligned $La_{1.85}Sr_{0.15}CuO_4$ where $\hbar\Gamma_B = c_0 \cdot 84$ meV [43], and in $YBa_2Cu_3O_y$ where $\hbar\Gamma_B = c_0 \cdot 100$ meV [91] and $\hbar\Gamma_B = c_0 \cdot 85$ meV [37] have been deduced. Certain authors then take $c_0 = 1$ [37,43] while others take $c_0 = \pi$ [30,58,59,91] depending on the details of the theoretical idea behind Eq. (D.2). Using both models as extremes gives 75 meV $\leq \hbar\Gamma_B \leq$ 223 meV, which is comparable to the exchange energy $J \simeq 130$ meV.

Bibliography

[1] A. Abragam, *Principles of Nuclear Magnetism*, (Oxford University Press, 1978), 1996 reprint.

[2] A. Abragam and B. Bleaney, *Electron Paramagnetic Resonance of Transition Ions* (Oxford University Press, New York), 1980.

[3] H. Alloul, A. Mahajan, H, Casalta, and O. Klein, Phys. Rev. Lett. **70**, 1171 (1993).

[4] J. Bardeen, L.N. Cooper, and J.R. Schrieffer, Phys. Rev. **108**, 1175 (1957).

[5] J.G. Bednorz and K.A. Müller, Z. Phys. B **64**, 189 (1986).

[6] R.J. Birgeneau, C.Y. Chen, D.R. Gabbe, H.P. Jenssen, M.A. Kastner, C.J. Peters, P.J. Picone, Tineke Thio, T.R. Thurston, H.L. Tuller, J.D. Axe, P.Böni, and G. Shirane, Phys. Rev. Lett. **59**, 1329 (1987).

[7] R. J. Birgeneau, D. R. Gabbe, H. P. Jenssen, M. A. Kastner, P. J. Picone, T. R. Thurston, G. Shirane, Y. Endoh, M. Sato, K. Yamada Y. Hidaka, M. Oda, Y. Enomoto, M. Suzuki, and T. Murakami, Phys. Rev. B **38**, 6614 (1988).

[8] R.J. Birgeneau, M. Greven, M.A. Kastner, Y.S. Lee, B.O. Wells, Y. Endoh, K. Yamada, and G. Shirane, Phys. Rev. B **59**, 13788 (1999).

[9] B.I. Bleaney and B. Bleaney, *Electricity and Magnetism*, Oxford University Press, 1976, Reprint 1991.

[10] B. Bleaney, K.D. Bowers, and M.H.L. Pryce, Proc. R. Soc. London, A **228**, 166 (1955).

[11] J. Bobroff, H. Alloul, S. Ouazi, P. Mendels, A. Mahajan, N. Blanchard, G. Collin, V. Guillen, and J.-F. Marucco, cond-mat/0203225.

[12] E.S. Božin, S.J.L. Billinge, G.H. Kwei, and H. Tagaki, Phys. Rev. B **59**, 4445 (1999).

[13] M. Braden, M. Meven, W. Reichardt, L. Pintschovius, M.T. Fernandez-Diaz, G. Heger, F. Nakamura, and T. Fujita, Phys. Rev. B **63**, 140510 (2001).

[14] M. Braden, P. Schweiss, G. Heger, W. Reichardt, Z. Fisk, K. Gamayunov, I. Tanaka, and H. Kojima, Physica (Amsterdam) **223C**, 396 (1994).

[15] J. Burgy, M. Mayr, V. Martin-Mayor, A. Moreo, and E. Dagotto, Phys. Rev. Lett. **87**, 277202 (2001).

[16] A. Campana, R. Cantelli, F. Cordero, M. Corti, and A. Rigamonti, Euro. Phys. J. B **18**, 49 (2000).

[17] A.H Castro Neto, Phys. Rev. B **51**, 3254 (1995).

[18] J.H. Cho, F.C. Chou, and D.C. Johnston, Phys. Rev. Lett. **70**, 222 (1993).

[19] M.K. Crawford, R.J. Harlow, E.M. McCarron, W.E. Farneth, J.D. Axe, H. Chou, and Q. Huang, Phys. Rev. B **44**, 7749 (1991).

[20] N.J. Curro, P.C. Hammel, B.J. Suh, M. Hücker, B. Büchner, U. Ammerahl, and A. Revcolevschi, Phys. Rev. Lett. **85**, 642 (2000).

[21] A. Fujimori, E. Takayama-Muromachi, Y. Uchida, and B. Okai, Phys. Rev. B **35**, 8814 (1987).

[22] S. Fujiyama, Y. Itoh, H. Yasuoka, and Y. Ueda, J. Phys. Soc. Jpn. **66**, 2864 (1997).

[23] E. Fukushima and S.B.W. Roeder, *Experimental Pulse NMR, A nuts and Bolts Approach*, Persius Books Publishing, 1981.

[24] D.M. Ginsberg, *Physical Properties of High Temperature Superconductors II*, World Scientific Publishing Co. 1990.

[25] J. Haase, C.P. Slichter, R. Stern, C.T. Milling, and D.G. Hinks, Physica (Amsterdam) **341C**, 1727 (2000).

[26] P.C. Hammel, A.P. Reyes, S.W. Choeng, Z. Fisk, and J.E. Schirber, Phys. Rev. Lett. **71**, 440 (1993).

[27] D. Haskel, E.A. Stern, D.G. Hinks, A.W. Mitchell, and J.D. Jorgensen, Phys. Rev. B **56**, 521 (1997).

[28] D. Haskel, E.A. Stern, D.G. Hinks, A.W. Mitchell, F.D. Jorgensen, and J.I. Budnick, Phys. Rev. Lett. **76**, 439 (1996).

[29] S.M. Hayden, G. Aeppli, R. Osborn, A.D.Taylor, T.G. Perring, S.-W. Cheong, and Z. Fisk, Phys. Rev. Lett. **67**, 3622 (1991).

[30] M. Horvatić, C. Berthier, Y. Berthier, P. Ségransan, P. Butaud, W.G. Clark, J.A. Gillet, and J.Y. Henry, Phys. Rev. B **48**,

[31] A.W. Hunt, P.M. Singer, K.R. Thurber, and T. Imai, Phys. Rev. Lett. **82**, 4300 (1999).

[32] A.W. Hunt, P.M. Singer, A.F. Cederstöm, and T. Imai, Phys. Rev. B **64**, 134525 (2001).

[33] P. Hüsser, H. U. Suter, E. P. Stoll, and P. F. Meier, Phys. Rev. B **61**, 1567 (2000).

[34] H.Y. Hwang, B. Batlogg, H. Takagi, H.L. Kao, J. Kwo, R.J. Cava, J.J. Krajewski, and W.F. Peck, Phys. Rev. Lett. **72**, 2636 (1994).

[35] N. Ichikawa, S. Uchida, J.M. Tranquada, T. Niemoeller, P.M. Gehring, S.-H. Lee, and J.R. Schneider, Phys. Rev. Lett. **85**, 1738 (2000).

[36] T. Imai, C.P. Slichter, K. Yoshimura, and K. Kosuge, Phys. Rev. Lett. **70**, 1002 (1993).

[37] T. Imai, C.P. Slichter, A.P. Paulikas, and B. Veal, Phys. Rev. B **47**, 9158 (1993).

[38] T. Imai, K. Yoshimura, T. Uemura, H. Yasuoka, and K. Kosuge, J. Phys. Soc. Jpn. **59**, 3846 (1990).

[39] T. Imai, T. Shimizu, T. Tsuda, H. Yasuoka, T. Takabatake, Y. Nakazawa, and M. Ishikawa, J. Phys. Soc. Jpn. **57**, 1771 (1988).

[40] Y. Itoh, M. Matsumura, H. Yamagata, and H. Miyamoto, J. Phys. Soc. Jpn. **65**, 695 (1996).

[41] Y. Itoh, M. Matsumura, and H. Yamagata, J. Phys. Soc. Jpn. **65**, 3747 (1996).

[42] V. Jaccarino, in *Theory of Magnetism and Transition Metals*, Proceedings of the international School of Physics "Enrico Fermi" Course No. XXXVII (Academic Press, New York, 1967).

[43] R.E. Walstedt *et al.*, Phys. Rev. Lett. **72**, 3610 (1994).

[44] J.D. Jorgensen, Jpn. J. Appl. Phys. **26**, 2017 (1987).

[45] M.-H. Julien, A. Campana, A. Rigamonti, P. Carretta, F. Borsa, P. Kuhns, A.P. Reyes, W.G. Moulton, M. Horvatić, C. Berthier, A. Vietkin, and A. Revcolevschi, Phys. Rev. B **63**, 144508 (2001).

[46] B. Keimer, N. Belk, R.J. Birgeneau, A. Cassanho, C.Y. Chen, M. Greven, M.A. Kastner, A. Aharony, Y. Endoh, R.W. Erwin, and G. Shirane, Phys. Rev. B **46**, 14034 (1992).

[47] H. Kimura, K. Hirota, C.-H. Lee, K. Yamada, and G. Shirane, J. Phys. Soc. Jpn. **69**, 851 (2000).

[48] H. Kimura, H. Hirota, H. Matsushita, K. Yamada, Y. Endoh, S.-H. Lee, C.F. Majkrzak, R. Erwin, G. Shirane, M. Greven, Y.S. Lee, M.A. Kastner, and R.J. Birgeneau, Phys. Rev. B **59**, 6517 (1999).

[49] K.-I Kumagi, K. Kawano, I. Watanabe, K. Nishiyama, and K.Nagamine, Hyperfine Int. **86**, 473 (1994).

[50] Y.S. Lee, R.J. Birgeneau, M.A. Kastner, Y. Endoh, S. Wakimoto, K. Yamada, R.W. Erwin, S.-H, Lee, G. Shirane, Phys. Rev. B **60**, 3643 (1999).

[51] D.E. MacLaughling and H. Alloul, Phys. Rev. Lett. **36**, 1158 (1976).

[52] R.L. Martin, Phys. Rev. Lett. **75**, 744 (1995).

[53] I. Martin and A.V. Balatsky, Physica (Amsterdam) **357C**, 46 (2001).

[54] T.E. Mason, G. Aeppli, and H.A. Mook, Phys. Rev. Lett. **68**, 1414 (1992).

[55] M. Matsuda, M. Fujita, K. Yamada, R.J. Birgeneau, M.A. Kastner, Y. Endoh, S. Wakimoto, and G. Shirane, Phys. Rev. B **62**, 9148 (2000).

[56] H. Matsushita, H. Kimura, M. Fujita, K. Yamada, K. Hirota, and Y. Endoh, J. Phys. Chem. Solid **60**, 1071 (1999).

[57] F. Mila and T.M. Rice, Physica C **157**, 561 (1989).

[58] A.J. Millis, H. Monien, and D. Pines, Phys. Rev. B **42**, 167 (1990).

[59] H. Monien, P. Monthoux, and D. Pines, Phys. Rev. B **43**, 275 (1991).

[60] A.R. Moodenbaugh, Y. Xu, M. Suenaga, T.J. Folkerts, and R.N Shelton, Phys. Rev. B **38**, 4596 (1988).

[61] T. Moriya, J. Phys. Soc. Jpn. **18**, 516 (1963).

[62] B. Nachumi, Y. Fudamoto, A. Keren, K.M. Kojima, M. Larkin, G.M. Luke, J. Merrin, O. Tchernyshyov, Y.J. Uemura, N. Ichikawa, M. Goto, H. Takagi, S. Uchida, M.K. Crawford, E.M. McCarron, D.E. MacLaughlin, and R.H. Heffner, Phys. Rev. B **58**, 8760 (1998).

[63] H. Nagasawa and W.A. Steyert, J. Phys. Soc. Jpn. **28**, 1171 (1970).

[64] A. Narath, Phys. Rev. **162**, 320 (1967).

[65] Ch. Niedermayer, C. Bernhard, T. Blasius, A. Golnik, A Moodenbaugh, and J.I. Budnick, Phys. Rev. Lett. **80**, 3843 (1998).

[66] T. Niemöller, H. Hünnefeld, J.R. Schneider, N. Ichikawa, S. Uchida, T. Frello, N.H. Andersen, and J.M. Tranquada, Euro. Phys. J. B **12**, 509 (1999).

[67] S.H. Pan, J.P. O'Neal, R.L. Badzey, C. Chamon, H. Ding, J.R Engelbrecht, Z. Wang, H. Eisaki, S. Uchida, A.K. Guptak, K.W Ng, E.W. Hudson, K.M. Lang, and J.C. Davis, Nature **413**, 292 (2001).

[68] C.H. Pennington, PhD Thesis (1989), Univeristy of Illinois.

[69] C.H. Pennington, D.J. Durand, C.P. Slichter, J.P. Rice, E.D. Bukowski, and D.M. Ginsberg , Phys. Rev. B **39**, 2902 (1989).

[70] C.H. Pennington and C.P. Slichter, Phys. Rev. Lett. **66**, 381 (1991).

[71] S. Pliberšek and P.F. Meier, Europhys. Lett. **50**, 789 (2000).

[72] P.G. Radaelli, D.G. Hinks, A.W. Mitchell, B.A. Hunter, J.L. Wagner, B. Dabrowski, K.G. Vandervoort, H.K. Viswanathan, and J.D. Jorgensen, Phys. Rev. B **49**, 4163 (1994).

[73] A.W. Sandvik, Phys. Rev. B **52**, R9831 (1995).

[74] A.T. Savici, Y. Fudamoto, I.M. Gat, M.I. Larkin, Y.J. Uemura, G.M. Luke, K.M. Kojima, Y.S. Lee, M.A. Kastner, and R.J. Birgeneau, Physica B **289-290**, 338 (2000).

[75] B. Shastry, Phys. Rev. Lett. **63**, 1288 (1989).

[76] T. Shimizu, J. Phys. Soc. Jpn. **62**, 772 (1993), and J. Phys. Soc. Jpn. **62**, 779 (1993).

[77] P.M. Singer, A.W. Hunt, A.F. Cederstöm, and T. Imai, Phys. Rev. B **60**, 15345 (1999).

[78] P.M. Singer, A.W. Hunt, A.F. Cederstöm, and T. Imai, proceedings to LT23, T. Imai inviter paper, accepted for publication.

[79] P.M. Singer, A.W. Hunt, and T. Imai, Phys. Rev. Lett. **88**, 47602 (2002).

[80] P.M. Singer, A.W. Hunt, T. Imai, F.C. Chou, K. Hirota, M. Takaba, T. Kakeshita, H. Eisaki, and S. Uchida, *to be published.*

[81] C.P. Slichter, *Principles of Magnetic Resonance*, (Springer-Verlag, New York 1989), 3rd ed. 1996.

[82] Y.-Q. Song, M.A. Kennard, M. Lee, K.R. Poppelmeier, and W.P. Halperin, Phys. Rev. B. **44**, 7159 (1991).

[83] B.W. Statt, P.C. Hammel, Z. Fisk, S.W. Cheong, F.C. Chou, D.C. Johnston, and J.E. Schirber, Phys. Rev. B **52**, 15575 (1995).

[84] R.M. Sternheimer, Phys. Rev. **164**, 10 (1967).

[85] M. Suzuki and M. Hikita, Phys. Rev. B **44**, 249 (1991).

[86] T. Suzuki and T. Fujita, J. Phys. Soc. Jpn. **6**, 1883 (1989).

[87] T. Suzuki, T. Goto, K. Chiba, T. Shinoda, T. Fukase, H. Kimura, K. Yamada, M. Ohashi, and Y. Yamaguchi, Phys. Rev. B **57**, R3229 (1998).

[88] H. Takagi, R.J. Cava, M. Marezio, B. Batlogg, J.J. Krajewski, W.F. Peck, P. Bordet, and D.E. Cox, Phys. Rev. Lett. **68**, 3777 (1992).

[89] H. Takagi, T. Ido, S. Ishibashi, M. Uota, S. Uchida, and Y. Tokura, Phys. Rev. B **40**, 2254 (1989).

[90] M. Takigawa, P.C. Hammel, R.H. Heffner, Z. Fisk, K.C. Ott, and J.D. Thompson, Phys. Rev. Lett. **63**, 1865 (1989).

[91] M. Takigawa, A.P. Reyes, P.C. Hammel, J.D. Thompson, R.H Heffner, Z. Fisk, and K.C. Ott, Phys. Rev. B **43**, 247 (1991).

[92] H. Tou. M. Matsumura, and H. Yamagta, J. Phys. Soc. Jpn. **61**, 1477 (1992).

[93] J.M. Tranquada, B.J. Sternlieb, J.D. Axe, Y. Nakamura, and S. Uchida, Nature **375**, 561 (1995).

[94] J.M. Tranquada, J. D. Axe, N. Ichikawa, Y. Nakamura, S. Uchida, and B. Nachumi, Phys. Rev. B **54**, 7489 (1996).

[95] J.M. Tranquada, J.D. Axe, N. Ichikawa, A.R. Moodenbaugh, Y. Nakamura, and S. Uchida, Phys. Rev. Lett. **78**, 338 (1997).

[96] J.M. Tranquada, N. Ichikawa, and S. Uchida, Phys. Rev. B **59**, 14712 (1999).

[97] S. Wakimoto, G. Shirane, Y. Endoh, K. Hirota, S. Ueka, K. Yamada, R.J. Birgeneau, M.A. Kastner, Y.S. Lee, P.M. Gehring, and S.-H. Lee, Phys. Rev. B **60**, 769 (1999).

[98] R.E. Walstedt and S.W. Cheong, Phys. Rev. B **64**, 14404 (2001).

[99] R.M. White, *Quantum Theory of Magnetism*, (McGraw-Hill, New York 1970), 2nd Ed. 1983.

[100] K. Yamada, C.H. Lee, K. Kurahashi, J. Wada, S. Wakimoto, S. Ueki, H. Kimura, T. Endoh, S. Hosoya, G. Shirane, R.J. Birgeneau, M. Greven, M.A. Kastner, and Y.J. Kim, Phys. Rev. B **57**, 6165 (1998).

[101] K. Yoshimura, T. Imai, T. Shimizu, Y. Ueda, K. Kosuge, and H. Yasuoka, J. Phys. Soc. Jpn. **58**, 3057 (1989).

[102] M.v. Zimmermann, A. Vigliante, T. Niemöller, N. Ichikawa, T. Frello, J. Madsen, P. Wochner, S. Uchida, N.H. Andersen, J.M. Tranquada, D. Gibbs, and J.R. Schneider, Europhys. Lett. **41**, 629 (1998).

[103] Due to an unfortunate accident, we were only able to acquire data for $x = 0.07$ at 295 K.

[104] Stricktly speaking, NMR probes up to the penetration depth δ which for current experimental conditions is $\delta \gtrsim 10^6$ a.